



Growth Anisotropy and Cortical Microtubules in Explosive Pod Shatter

Inaugural-Dissertation

zur

Erlangung des Doktorgrades
der Mathematisch-Naturwissenschaftlichen Fakultät
der Universität zu Köln
vorgelegt von

Gaby Weber

aus Köln

Köln, 2018



Berichterstatter:	Prof. Dr. Miltos Tsiantis Prof. Dr. Martin Hülskamp
Prüfungsvorsitz:	Prof. Dr. Achim Tresch
Tag der letzten mündlichen Prüfung:	19.11.2018

Die vorliegende Arbeit wurde am Max-Planck-Institut für Pflanzenzüchtungsforschung in Köln in der Abteilung für vergleichende Entwicklungsgenetik (Direktor Prof. Dr. Miltos Tsiantis) angefertigt.

Acknowledgement

First of all I would like to thank Miltos Tsiantis for being my dissertation adviser.

Further, I thank my colleagues Sören Strauß, Brendan Lane and Adam Runions for their help with the MorphoGraphX software. I thank the Hay team's technician Wolfram Faigl, Marie Monniaux and Anahit Galstyan for all the supportive help in the lab. Without your help and hints, I would not have been able to finish my work within three years.

I also want to thank Kristin Krause for her private support. Thank you for helping me through the tough time of my thesis by diverting me. I thank you for your friendship and especially for always being there for me.

Very special thanks to Angela Hay, my direct supervisor. Thank you very much for your support and care during all this time. I have always felt comfortable with you and in your group. Thank you for always having an open ear for me and thank you for your patience (particularly at the beginning of the PhD thesis when I came to you from another scientific field). Most of all, I thank you for your trust in every way.

Thank you.

Abstract

The goal of my project is to investigate how the fruit pod of *Cardamine hirsuta* explodes to disperse its seeds. Recently, it was shown that the fruit pods coil due to the rapid release of tension generated by differential shortening of fruit valve tissues. It was further shown that shortening of the exocarp tissue is an active process and does not arise from passive shrinkage. Finite-element modelling (FEM) predicted that this process is dependent on the 3D geometry and anisotropy of exocarp cells. Cell growth anisotropy is determined by the net alignment of cortical microtubules (CMT), which guide the direction of cellulose synthesis in the cell wall. However, the specific function of CMT alignment in explosive pod shatter is not clear. Thus, the aim of my project is to characterize the alignment of CMT arrays during fruit development and their function in explosive pod shatter. I used confocal laser scanning microscopy to visualise a fluorescently labelled tubulin $\alpha 6$ protein in order to analyse CMT alignment. To perturb CMT alignment, I used the herbicide oryzalin to depolymerize CMT. In a genetic approach, I silenced gene expression of the microtubule severing protein Katanin (KTN1) using an inducible artificial microRNA (amiRKTN1). My results showed that daily oryzalin treatment of maturing fruit pods abolished CMT organisation in the exocarp cells of *C. hirsuta*, which abolished explosive pod shatter. However, *KTN1* gene silencing was not sufficient to impact exocarp CMT alignment or affect explosive pod shatter. In summary, my perturbations with oryzalin showed that aligned CMT arrays are required for turgor-driven contraction of the exocarp cell layer and explosive pod shatter in *C. hirsuta*.

Zusammenfassung

Ziel meines Projektes ist zu untersuchen wie die Frucht der *Cardamine hirsuta* zerspringt um die Samen zu verteilen. Kürzlich wurde gezeigt, dass sich die Schoten durch das plötzliche Freiwerden von Spannung, welche durch Verkürzung von Fruchuventilgeweben erzeugt wird, aufwickeln. Die Verkürzung des Exokarpusgewebes ist ein aktiver Prozess und entsteht nicht durch passives Schrumpfen. Mittels eines Finite-Element-Modells (FEM) wurde vorhergesagt, dass dieser Prozess von der 3D Geometrie und der Anisotropie der Exocarpzellen abhängt. Die Zellwachstumsanisotropie ist durch die Ausrichtung der kortikalen Mikrotubuli (CMT) bestimmt, welche die Richtung der Zellulosesynthese in der Zellwand leiten. Die spezifische Funktion der Mikrotubulieusrichtung in dem Zerplatzen der *C. hirsuta* Schoten ist jedoch unklar. Ziel meines Projektes ist es daher, die Ausrichtung der CMT während der Fruchtentwicklung und deren Funktion in den zerspringenden Schoten zu charakterisieren. Ich nutze konfokale Laserscanmikroskopie genutzt um mittels der Visualisierung von einem fluoreszenzmarkierten Tubulin- $\alpha 6$ -Protein die CMT-Ausrichtung zu analysieren. Um die CMT-Ausrichtung zu stören, verwendete ich das CMT depolymerisierende Herbizid Oryzalin. In einem genetischen Ansatz deaktivierte ich das Mikrotubuli-schneidende Protein Katanin (KTN1) während der Fruchtentwicklung in *C. hirsuta* mit einer induzierbaren künstlichen MikroRNA (amiRKTN1). Meine Ergebnisse zeigen, dass eine tägliche Behandlung von reifenden Schoten mit Oryzalin die CMT-Organisation in den Exokarpzellen der *C. hirsuta* aufhebt. Dies wiederum hat zur Folge, dass die Schoten die Fähigkeit zu zerspringen verlieren. Die Herabregulation von *KTN1* ist jedoch nicht ausreichend, um die Ausrichtung der CMT oder das Zerspringen der Schoten zu beeinflussen. Zusammengefasst zeigten meine Perturbationen mit Oryzalin, dass ausgerichtete

CMT-Anordnungen für die Turgor-gesteuerte Kontraktion der Exocarp-Zellschicht und für die zerpringende Schoten in *C. hirsuta* benötigt werden.

List of Abbreviations

%	Percentage
°C	Degree Celsius
µg	Microgramm
µm	Micrometer
µM	Micromolar
<i>A. thaliana</i>	<i>Arabidopsis thaliana</i>
<i>A. tumefaciens</i>	<i>Agrobacterium tumefaciens</i>
amiR	Artificial micro RNA
<i>C. hirsuta</i>	<i>Cardamine hirsuta</i> Oxford
CaM35S	Cauliflower Mosaic Virus 35S Promoter
CLSM	Confocal Laser Scanning Microscopy
CMT	Cortical Microtubules
Col-0	Columbia-0
Dex	Dexamethasone
DMSO	Dimethylsulfoxide
DNA	Deoxyribonucleic acid
dNTP	Nucleoside triphosphate
DZ	Dehiscence zone
EDTA	Ethylenediaminetetraacetic acid
GFP	Green Fluorescent Protein
GUS	β-glucuronidase
h	Hours
KTN1	Katanin

l	Liters
LB medium	Luria Broth Medium
MAPs	Magnesium chloride
MgCl ₂	Minute
min	Milliliters
ml	Millimeters
mm	Millimolar
mM	Murashige and Skoog Medium
MS Medium	Microtubules
MT	Sodium chloride
NaCl	Magnesium chloride
ng	Nanogram
nm	Nanometer
Norf	Norflurazon
OD	Optical Density
Oligo (dt) primers	Primer with poly Thymine tail
Ox	Oxford
PCR	Polymerase Chain reaction
RNA	Ribonucleic acid
RT-qPCR	Real Time Quantitative PCR
s	Second
SDS	Sodium dodecyl sulfate
T1	First generation of transformed seeds
T2	Second generation of transformed seeds

T-DNA	Transfer DNA
TE Buffer	Buffer containing TRIS and EDTA
TRIS Buffer	Tris(hydroxymethyl-aminomethane
TUA6	Tubulin alpha 6
WT	Wildtype
X-Gluc	5 bromo 4 chloro 3 indolyl- β -D-glucuronic acid

Content

Acknowledgement

Abstract

Zusammenfassung

List of Abbreviations

Content

1. Introduction.....	1
1.1. Fruits and Seed Dispersal in the Brassicaceae.....	1
1.2. <i>Arabidopsis thaliana</i> Fruit Development.....	2
1.3. Rapid Plant Movements	5
1.4. <i>Cardamine hirsuta</i> as a Model Organism	5
1.4.1. Explosive Pod Shatter	6
1.5. Structure and Function of the Plant Cell Wall	9
1.6. Role of Cortical Microtubules (CMT) in Plant Growth.....	9
1.6.1. Chemical Perturbation of CMT Alignment	12
1.6.2. MT Severing Protein Katanin	12
1.7. Aim of the Thesis	14
2. Materials and Methods	15
2.1. Chemicals.....	15
2.2. Buffers, Media and Solutions	15
2.3. Plant Materials and Growth Conditions	15

2.3.1.	Plant Material	15
2.3.2.	Plant Growth Conditions	15
2.4.	Bacteria Strains.....	15
2.5.	Oligonucleotides.....	16
2.6.	Genetic Methods	17
2.6.1.	Transgenic Constructions	17
2.6.2.	Plant Transformation.....	17
2.6.3.	Selection of Transgenic Plants.....	18
2.6.4.	Sterilisation of Transgenic Seeds	18
2.6.5.	Dexamethasone (Dex) Induction	18
2.7.	Molecular biology methods.....	19
2.7.1.	Genomic DNA Extraction	19
2.7.2.	RNA Isolation	19
2.7.3.	Gel Electrophoresis.....	19
2.7.4.	Oryzalin Treatment.....	19
2.7.5.	Osmotic treatment	20
2.7.6.	β -glucuronidase Staining with X-Gluc substrate (GUS staining).....	20
2.8.	Analytical Methods.....	21
2.8.1.	PCR.....	21
2.8.2.	Quantitative Reverse Transcriptase PCR (RT-qPCR)	21
2.8.3.	Valve coiling analysis	22
2.9.	Microscopy Techniques.....	22
2.9.1.	Light Microscopy and Imaging.....	22

2.9.2. Confocal Laser Scanning Microscopy (CLSM)	22
2.10. Bioinformatics.....	22
2.10.1 Primer Design	22
2.10.2 MorphoGraphX.....	23
3 Results	25
3.1. Staging Fruit Development in <i>C. hirsuta</i> and <i>A. thaliana</i>	25
3.2. Defining the Time Point of CMT Reorientation	36
3.3. CMT Disruption with Oryzalin	39
3.4. KATANIN1 (<i>KTN1</i>) Silencing During Fruit Development	54
4. Discussion	75
4.1. Summary.....	75
4.2. Staging Fruit Development in <i>C. hirsuta</i> and <i>A. thaliana</i>	76
4.3. CMT Disruption with Oryzalin	78
4.4. <i>KTN1</i> Silencing During Fruit Development	83
5. Future Perspective.....	85
Figures	86
Tables.....	89
Sources	90
Erklärung	
Curriculum Vitae	

1. Introduction

1.1. Fruits and Seed Dispersal in the Brassicaceae

Since evolving more than 250 million years ago, Angiosperms evolved great diversity in species and a wide range of seed dispersal strategies making them highly efficient in colonising territories (Langowski *et al.*, 2016; Bowman *et al.*, 2007). This success is primarily based on the ability of flowering plants to form fruit, which help to protect and disperse the seeds (Langowski *et al.*, 2016; Chaffey, 2008). Fruits develop from the ovary walls and can be classified based on morphology and the mode of seed dispersal (Esau, 1977). Thus, on the basis of fruit wall histology, fruits are distinguished into fleshy fruits and dry fruits (Esau, 1977).

Fleshy fruits can be subdivided into fruits with a rind (e.g. citrus fruits, bananas etc.) and fruits without a rind (e.g. cherries, tomatoes) (Esau, 1977). In general, these fruit have a pericarp that develops into a fleshy tissue attracting animals and/or humans to assist in seed dispersal (Esau, 1977; Langowski *et al.*, 2016). Dry fruits are subdivided into indehiscent and dehiscent fruits (Esau, 1977). Indehiscent fruits often originate from ovaries, which develop one single seed (Esau, 1977). In contrast, dehiscent fruits carry several seeds that are disclosed at maturity. Thus, abiotic factors like water and wind can be used to ensure seed dispersal (Langowski *et al.*, 2016; Chaffey, 2008). The dehiscence process occurs late in fruit development when a dehiscence zone (DZ) is formed, allowing cell separation between fruit tissues (Esau, 1977).

Many species in the Brassicaceae family have dehiscent fruit and disperse their seeds by pod shatter. This dispersal strategy refers to how the fruit shatters or disintegrates upon light mechanical pressures after dehiscence has occurred (Dinneny and Yanofsky 2005). So far, genetic analysis of dry, dehiscent fruit development is

mostly limited to the Brassicaceae species and model plant *Arabidopsis thaliana* (Dinney and Yanofsky 2005).

1.2. *Arabidopsis thaliana* Fruit Development

A. thaliana is a small, annual, self-fertilizing weed of the Brassicaceae family, which is native in Europe, Asia and Africa but naturalized worldwide (Price *et al.*, 1995; Somerville and Koornneef, 2002). By having a relatively short life cycle (approx. eight weeks), requiring simple growth conditions and producing up to 10000 seeds from a single individual, *A. thaliana* is an ideal organism for laboratory propagation. Further, it is a suitable model for genetic research because it is diploid, with a small genome (135Mb), and efficient, stable transformation protocols, that enable genetic and genomic methods to investigate a variety of biological problems (Page and Grossniklaus, 2002; Somerville and Koornneef, 2002).

The fruit of *A. thaliana* develops from the fertilized gynoecium forming a silique, which dehisces and dries at maturity (Roeder and Yanofsky, 2006). It comprises two valves, attached to the replum, that cover and protect the developing seeds. Connecting each valve to the replum is the valve margin tissue, which differentiates into a separation layer and a lignified cell layer to create the dehiscence zone (DZ) (Figure 1, Dinney and Yanofsky, 2005). Discrete stages of *A. thaliana* flower and fruit development are described in detail in *The Arabidopsis Book* (Roeder and Yanofsky, 2006). Stages one to 13 describe flower developmental stages. Fertilization occurs in stage 14, and stage 15 and is characterised by an elongating gynoecium extending beyond the stamens denoting the start of fruit development in *A. thaliana*. During stage 16, sepals, petals and stamens wither and fall from the fruit. In the beginning of stage 17 (stage 17a), the fruit elongates further to almost final length. Additionally, the lignification of the endocarp *b* layer (*enb*) and valve margin occurs,

and the endocarp a (*ena*) cell layer disintegrates. At the end of stage 17 (stage 17b), the fruit reaches its final length and width. Then, the fruit yellows (stage 18) before it dries and turns brown (stage 19). Dehiscence occurs during stage 19 when the valves separate from the fruit (Roeder and Yanofsky, 2006). Finally, in stage 20, the seeds abscise from the fruit, leaving a dried replum and septum behind (Roeder and Yanofsky, 2006).

The process of dehiscence depends on the precise patterning of fruit tissues. This patterning requires the orchestrated activity of transcription factors that regulate cell fate differentiation and mechanical processes at the valve margin (Ferrándiz, 2002; Dinneny and Yanofsky, 2005). The gene *FRUITFULL* (*FUL*) encodes a MADS-box transcription factor that limits the expression of valve margin identity genes to the valve margin (Gu *et al.*, 1998; Liljegren *et al.*, 2004). *FUL* is expressed in valves during fruit development and loss of function mutants exhibit severely reduced fruit sizes and thus, highly compacted seeds (Gu *et al.*, 1998). Complementary to *FUL*, the MADS-box genes *SHATTERPROOF1* and *2* (*SHP1*, *SHP2*) promote valve margin development (Langowski *et al.*, 2016; Ferrandiz *et al.*, 2000). Both genes are redundantly expressed in all medial tissues (replum, valve margins, septum and ovules) and specify the valve margin lignification and separation layer formation, resulting in the differentiation of the valve margin into the DZ prior to seed dispersal (Liljegren, 2000). By repressing *SHP1/2* expression and thus preventing valve margin cell fate, the *REPLUMLESS* (*RPL*) homeobox gene regulates replum development (Roeder *et al.*, 2003). Another gene controlling dehiscence is the basic-helix-loop-helix transcription factor *ALCATRAZ* (*ALC*) (Rajani and Sundaresan, 2001). *ALC* expression is restricted to the valve margin during fruit development and is required for separation layer formation (Rajani and Sundaresan, 2001). However, the atypical basic-helix-loop-helix transcription factor *INDEHISCENT* (*IND*) exhibits the strongest

effect on valve margin development, since loss of function mutants develop fruits without a dehiscence zone. *IND* expression is limited to the valve margin and ectopically expressed in *ful* where it causes many of the phenotypes found in *ful* mutant fruit (reduced fruit size, ectopic lignification, loss of valve cell identity) (Liljegren *et al.*, 2004). Therefore, patterning of the different fruit tissues is achieved by different transcription factors limiting *IND* expression to the dehiscence zone.

Taken together, *A. thaliana* has dehiscent siliques, patterned by a network of transcription factor interactions, and uses pod shatter for seed dispersal.

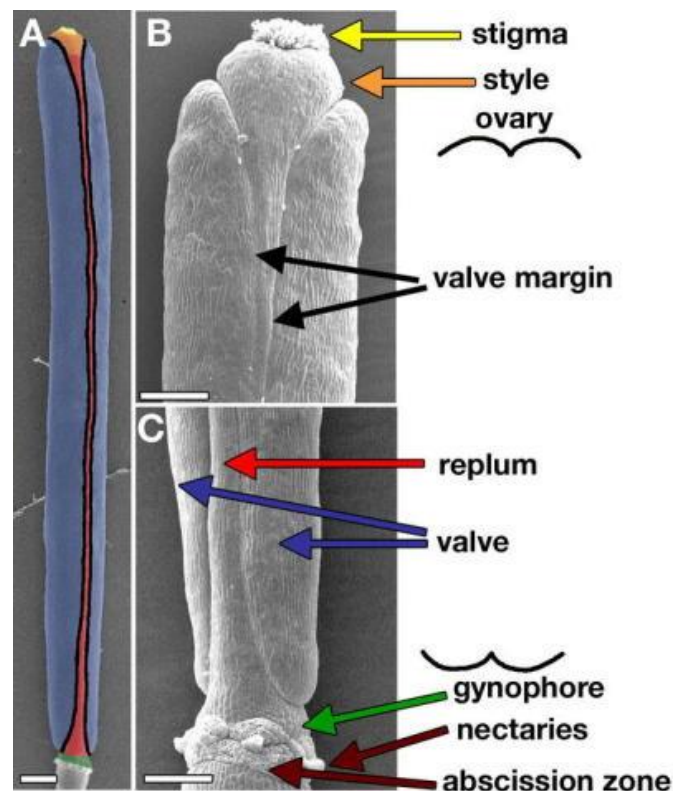


Figure 1: Scanning electron micrograph of an *A. thaliana* WT fruit at stage 17 (Roeder and Yanofsky 2006).

1.3. Rapid Plant Movements

Although plants are stationary, they show a variety of movements with different speeds (Skotheim and Mahadevan, 2005). Tropisms, such as the coiling of tendrils and the orientation of organs to optimize photosynthesis, are examples of slow plant movements (Darwin, 1881; Geitmann, 2016). Such slow movements are based on cells growing, swelling or shrinking, which are processes driven by turgor pressure, and hence the speed of these movements is limited by the speed of water transport through cells and tissues (Skotheim and Mahadevan, 2005). To speed up their movements, plants require a mechanism to store energy gradually and release it rapidly. Such a mechanism enables plant movements at a millisecond scale. Examples of rapid plant movements include the fast closure of the Venus flytrap (*Dionaea muscipula*), the high-speed pollen release of the *white mulberry* or the seed dispersal by explosive pod shatter of *Cardamine hirsuta* (Forterre *et al.*, 2005; Taylor *et al.*, 2006; Hofhuis *et al.*, 2016). Generally, most rapid movements are associated with the dispersal of spores, pollen grains or seeds since fast plant motion enables small particles to surmount adhesion and drag to become airborne (Martone *et al.*, 2010). However, there is still little known about the biological processes that enable rapid plant movements.

1.4. *Cardamine hirsuta* as a Model Organism

C. hirsuta belongs to the Brassicaceae family and is considered native in Europe and from there spread worldwide (Hay *et al.*, 2014). As a close relative of the model plant *A. thaliana*, *C. hirsuta* shares many similar traits (Hay and Tsiantis, 2016). Both plants are diploid, form a small rosette that allows large-scale cultivation, need eight weeks for seed generation (seed-to-seed) and show an abundant seed set

(Hay *et al.*, 2014). The genome of *C. hirsuta* is 198 MBp (Gan *et al.*, 2016) and *C. hirsuta* has a comparable transformation efficiency to *A. thaliana* (Hay *et al.*, 2014). These characteristics make *C. hirsuta* a good model system for comparative studies with *A. thaliana* (Hay *et al.*, 2014).

Although the two species are closely related, they differ in many traits (Hay *et al.*, 2014). Perhaps the most characteristic difference between the two species is their seed dispersal. *C. hirsuta* disperses its seeds ballistically via explosive pod shatter whereas *A. thaliana* uses non-explosive pod shatter. Both species have dehiscent fruit, but only the valves of *C. hirsuta* coil explosively. In this way, *C. hirsuta* is able to launch its seeds over a 5 m diameter (Hofhuis *et al.*, 2016). Hence, explosive seed dispersal fits the life history strategy of *C. hirsuta* as a ruderal weed that is a pioneer coloniser of disturbed ground.

1.4.1. Explosive Pod Shatter

Explosive pod shatter in *C. hirsuta* is a rapid process that spreads seeds several meters away from the parent plant within a few milliseconds (Hofhuis *et al.*, 2016). The explosion starts when the valves detach from the fruit and rapidly coil back, usually from the base to the apex of the fruit. By transient adhesion to the inner valve surface, seeds are ballistically launched at approximately 10 m/s during the valve coiling (Hofhuis *et al.*, 2016). Finally, the valve comes to rest in a curled configuration of three to four coils (Figure 2, Hofhuis *et al.*, 2016). Such a rapid process requires mechanisms that enable the storage of elastic energy and its sudden, fast release. The cellular basis of these mechanisms have been recently identified in *C. hirsuta* (Hofhuis *et al.*, 2016).

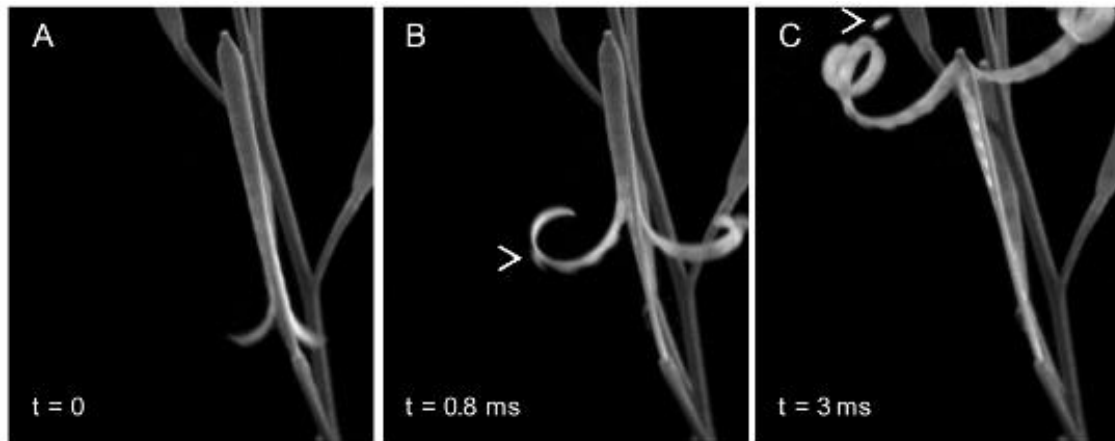


Figure 2: Process of ballistical seed dispersal of *C. hirsuta*. A) Explosive pod shatter starts when valves detach from the replum. B) Valves coil rapidly due to released tension. C) The seeds are launched away.

To understand the mechanism of explosive seed dispersal in *C. hirsuta*, each fruit valve was modelled as three mechanical layers: an inner layer (endocarp *b*) that is lignified and thus stiff and inextensible, a middle layer (mesocarp) that is a passive buffering layer, and an active outer layer (exocarp) (Figure 2, Hofhuis *et al.*, 2016). During *C. hirsuta*'s fruit maturation, the exocarp layer shortens in length due to the anisotropic growth of its cells, but this contraction is resisted since the exocarp is attached to the inextensible endocarp *b* layer. The differential contraction of these valve tissues generates tension along the length of the valve. An elastic instability in the valve allows this tension to be released by explosive coiling once the dehiscence zones weaken along the length of each valve (Hofhuis *et al.*, 2016).

Surprisingly, tension develops before the fruit dries. This means that exocarp cells do not contract passively through loss of turgor pressure as reported previously (Vaughn *et al.*, 2011), but rather, they contract actively while alive and turgid (Hofhuis *et al.*, 2016). This result could be demonstrated using osmotic treatments where valves coiled more tightly in water and loosely in salt solution, suggesting that turgor pressure drives exocarp cell contraction (Hofhuis *et al.*, 2016). Indeed, at the

cellular level, exocarp cells lengthened considerably when plasmolysed in salt solution and contracted in water (Hofhuis *et al.*, 2016). To explore this cellular contraction and identify properties of the exocarp cells in *C. hirsuta* that allow them to contract in length, a finite element model of pressurized cells was constructed (Hofhuis *et al.*, 2016). This model could mimic the results of osmotic treatments when the actual geometry of mature, *C. hirsuta* exocarp cells was used, and the cell walls were anisotropic - stiffer in the longitudinal fruit direction (Figure 3) (Hofhuis *et al.*, 2016).

In summary, the tension that drives explosive pod shatter in *C. hirsuta* is caused by differential contraction of valve tissues through an active mechanism involving turgor-driven cellular contraction (Hofhuis *et al.*, 2016).

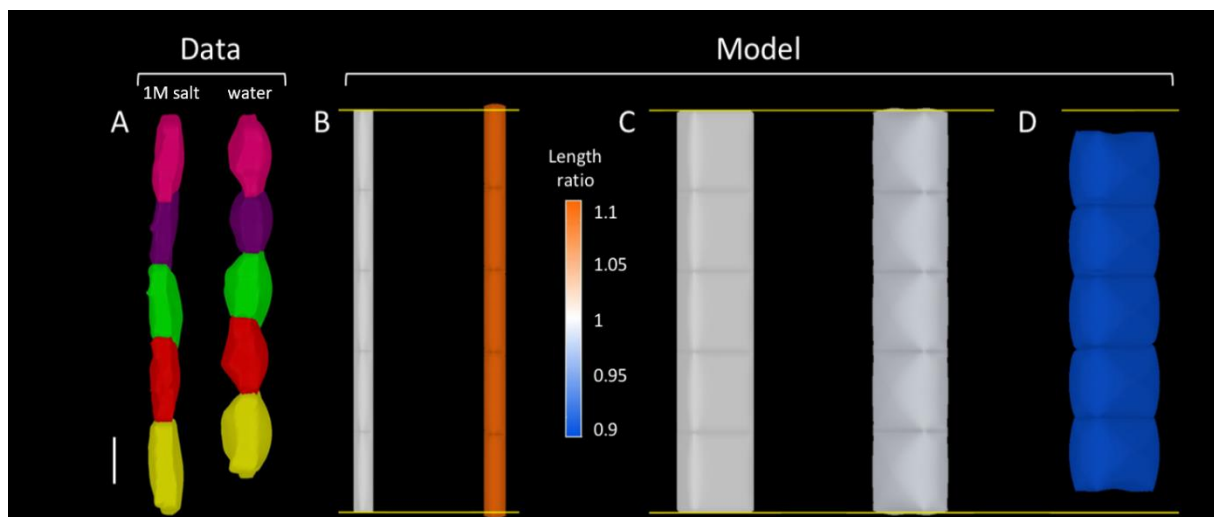


Figure 3: Turgor-driven contraction of exocarp cells. A) Treating *C. hirsuta* valve exocarp cells with a 1M salt solution caused cells to lengthen whereas a subsequent water treatment caused cells to contract. B) FEM simulations of cells pressurized from 0 Mpa (left) to 0.7 Mpa (right). Heatmap shows relative increase (orange) or decrease (blue) in cell length; horizontal yellow line shows initial length. Cell dimensions: 100 x 20 x 20 μm for *A. thaliana* (B) and 50 x 50 x 20 μm for *C. hirsuta* exocarp cells (C, D). Cell wall material: isotropic (B, C), anisotropic (D). Pressure: 0 Mpa (left, B, C), 0.7 Mpa (right, B – D). The figure is adapted from Hofhuis *et al.*, 2016. Scale bar: 20 μm .

1.5. Structure and Function of the Plant Cell Wall

Plant cells differ to animal cells because they are surrounded by a cell wall. Initially, plant cells develop a thin and flexible primary cell wall, which consists of a pectin matrix containing a mesh of cellulose-microfibrils. To strengthen the cell wall, plants either secrete hardening substances into the primary cell wall or add a secondary cell wall between the plasma membrane and the primary cell wall. The primary cell wall is composed of cellulose microfibrils embedded in a complex polysaccharide matrix, whereas the secondary cell wall often contains the cross-linked phenolic polymer lignin, providing the cell wall with stiffness and hydrophobicity (Cosgrove, 2005).

Cellulose-microfibrils are composed of several β -(1-4) linked D-glucose units, built by a cellulose synthase complex. This enzyme is located in the plasma membrane and extrudes cellulose microfibrils out in to the cell wall. The orientation of cellulose synthesis is directly dependent on the orientation of cortical microtubules (CMT), which are located adjacent to the plasma membrane (Paredez *et al.*, 2006). Hence, the direction of maximal cell expansion is indirectly determined by its CMT alignment (Baskin, 2005; Cosgrove, 2016).

1.6. Role of Cortical Microtubules (CMT) in Plant Growth

The growth of plant organs is a complex process, which can be defined as the irreversible deformation of cell walls by turgor pressure (Lloyd, 1991). During wall extension, cells take up water and thus increase in volume. The increase in volume is facilitated by cell wall yielding, which is the result of cell-wall loosening and severing of cellulose (Peaucelle *et al.*, 2015). Growth occurs by cell wall loosening combined with anisotropic reinforcement of the cell wall by cellulose (Boudon *et al.*, 2015;

Lockhart *et al.*, 1967; Cosgrove, 2016; Lloyd, 1991). However, the mechanisms controlling growth are still not well understood.

Growth can be measured by four regional parameters: 1) growth rate, which describes changes in size. 2) Anisotropy, which describes the amount of growth in a principal direction. 3) Growth direction, which describes the angle of the principal growth direction. 4) Rotation rate, which is thought to be an emergent mechanical effect describing a relative change in orientation over time (Figure 4, Coen *et al.*, 2004).

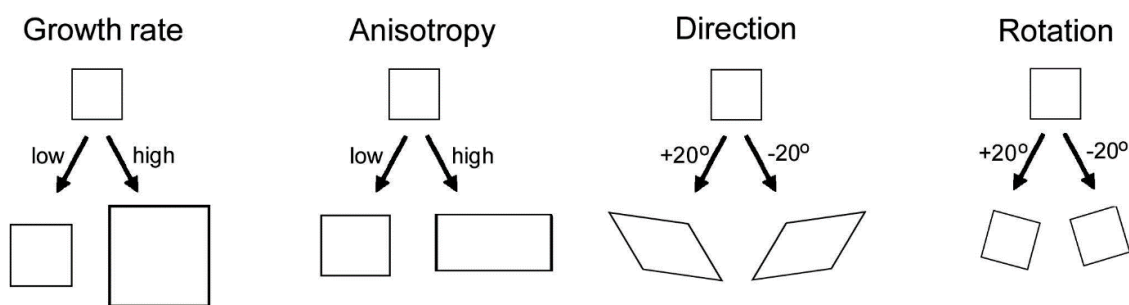


Figure 4: Schematic description of the four parameters for describing growth properties (Coen *et al.*, 2004).

Although turgor pressure drives cell expansion, growth is influenced by the orientation of cellulose microfibrils in the cell wall, which is guided by CMT alignment (Paredes *et al.*, 2006). Thus, CMT alignment indirectly determines the growth anisotropy of a cell. MT are hollow filaments of 13 cylindrically arranged, polar protofilaments, which are built of highly conserved α - and β -tubulin heterodimers (Alberts *et al.*, 2003; Fosket and Morejohn, 1992). Traversing the cytoplasm, they belong to the cytoskeleton and play an important role in intracellular organelle transport, polarity establishment, cell division and cell morphogenesis (Desai and Mitchison, 1997; Lin *et al.*, 2013). Due to continuous assembling and disassembling of tubulin dimers on the plus ends, MT are highly dynamic and able to quickly reorganise and reorient (Alberts *et al.*, 2003; Shaw *et al.*, 2003). CMTs are located adjacent to the

plasma membrane, in contrast to MTs that traverse the cytoplasm, and the dynamics of CMTs can be influenced by mechanical stress (Baskin *et al.*, 1994; Creff *et al.*, 2015; Uyttewaal *et al.*, 2012). For example, CMTs orient perpendicular to the maximal mechanical stress (Sampathkumar *et al.*, 2014).

In *C. hirsuta* and *A. thaliana*, CMT in the fruit exocarp cells reorient during fruit maturation (Hofhuis *et al.*, 2016). The CMT are transversely oriented early in development as the fruit elongates. When final fruit length is reached, exocarp CMT reorient to the longitudinal direction, associated with a change in growth direction as the fruit increases in width (Hofhuis *et al.*, 2016). The mechanism(s) regulating CMT orientation in the fruit are unknown. However, the ability to regulate CMT orientation is associated with all principle plant hormones (Lloyd, 1991). For example, auxin modulates CMT dynamics and, reciprocally, an intact CMT alignment is required for the polar transport of auxin to the cell wall where it is active (Sasidharan *et al.*, 2014; Sassi *et al.*, 2014). Auxin also regulates CMT dynamics via the plant's CMT severing protein Katanin (KTN1) since the hormone activates the KTN1 signaling pathway (Lin *et al.*, 2013; Sharma *et al.*, 2007; Hamant *et al.*, 2008). Thus, auxin indirectly promotes the organization of ordered CMT alignments (Lin *et al.*, 2013). CMT orientation is also regulated by microtubule associated proteins (MAPs) that stabilize tubulin dimers and thus control CMT assembly (Amos and Schlieper, 2005). Further, cell shape influences CMT alignment anisotropy since it depends on the local curvature of the cell surface strongly adjusting to the longest cell axis (Mirabet *et al.* 2017).

Overall, CMT play an important role in plant growth and development by influencing the mechanical anisotropy of the cell wall (Peaucelle *et al.*, 2015; Mirabet *et al.*, 2017).

1.6.1. Chemical Perturbation of CMT Alignment

CMT properties can be influenced by several naturally and synthetically produced chemicals (Baskin *et al.*, 1994; Dostál and Libusová, 2014; Dumontet and Jordan, 2010). Well studied MT-active chemicals like Colchicine, Paclitaxel and Vinblastine are used in medicine for anticancer treatment (Dostál and Libusová, 2014; Ganguly and Cabral, 2011; Jordan and Wilson, 2004) whereas other MT drugs show herbicidal effects and are therefore used in agriculture (Dostál and Libusová, 2014; Vaughn and Lehen, 1991). The most common MT-active herbicides are dinitroanilines like Oryzalin, Trifluralin, Benefin, Ethylfluralin, Pendimethalin and Prodamine, and pyridine-based compounds such as Dithiopyr and Thiazopyr (Dostál and Libusová, 2014). However, all MT-active chemicals act on MT by increasing (e.g. Paclitaxel) or decreasing (e.g. Vinblastine, Oryzalin) tubulin polymerization (Dostál and Libusová, 2014; Dumontet and Jordan, 2010).

CMT alignment in *A. thaliana* is commonly investigated by treating leaves, roots or seedlings with oryzalin (Baskin *et al.*, 1994; Corson *et al.*, 2009; Hugdahl and Morejohn, 1993). Oryzalin is a MT inhibitor since it causes MT depolymerisation by rapidly binding to tubulin dimers, thus preventing their incorporation into the MT polymer (Hugdahl and Morejohn, 1993). Although, the binding is reversible it causes a significant perturbation by intensely reducing CMT alignment (Hoffman and Vaughn, 1994; Hugdahl and Morejohn, 1993). Further, depolymerisation affects CMT reorientation since polar tubulin subunits are required for the assembly at the polymer's plus-end and disassembly at the minus-end (Cai, 2010).

1.6.2. MT Severing Protein Katanin

The ordered alignment and reorientation of MT requires the MT severing protein Katanin (KTN1) (McNally and Vale, 1993; Zhang *et al.*, 2013). This conserved protein

is a downstream component of the ROP6-RIC1 signalling pathway (Lin *et al.*, 2013) and is built of two subunits named according to their molecular weight: the bigger subunit p80, which is the regulatory unit, and p60, which is the catalytic subunit (Alberts *et al.*, 2003; McNally and Vale, 1993; Oda, 2015). Since p60 contains the region for protein interactions at its N-terminus, it is solely responsible for the ATP-dependent MT severing (Lindeboom *et al.*, 2013; McNally and Vale, 1993; Nakamura *et al.*, 2010; Wightman *et al.*, 2013; Wightman and Turner, 2007; Zhang *et al.*, 2013). KTN1 works via internal cleavage in the MT lattice at the minus ends and crossover sites of branching MTs (Lin *et al.*, 2013; McNally and Vale, 1993; Wightman and Turner, 2007) followed by continuous depolymerisation of tubulin dimers from the nucleation site, which further contributes to CMT organisation (Alberts *et al.*, 2003; Shaw *et al.*, 2003).

The importance of KTN1 for MT organization is revealed by KTN1 mutants and is well described in the literature (Burk *et al.*, 2001; Stoppin-Mellet *et al.*, 2006; Zhang *et al.*, 2013). A *KTN1* loss of function mutant in *A. thaliana* exhibits dwarf growth and shorter internode and fruit length (Burk *et al.*, 2001). Further, leaf pavement cells and hypocotyls of *A. thaliana* exhibit severe microtubule phenotypes in a loss of function KTN1 mutant since the CMT severing at crossover sites was completely abolished and mutants failed to recover CMT alignment following cold exposure (Zhang *et al.*, 2013). Similarly, KTN1 overexpression severely disturbs CMT alignment and produces small CMT fragments due to increased MT severing (Stoppin-Mellet *et al.*, 2006).

1.7. Aim of the Thesis

The focus of my project is to characterise CMT orientation during *C. hirsuta* fruit development and CMT function in explosive pod shatter. CMT orientation at the plasma membrane guides the orientation of cellulose microfibril synthesis. Thus, the net alignment of CMT arrays influence the direction of cell growth (anisotropy). We hypothesise that intact CMT arrays in the fruit exocarp are a key requirement for explosive pod shatter in *C. hirsuta*. To support this hypothesis, I propose to quantify CMT orientation and cell growth anisotropy in the exocarp during different stages of fruit development. To test this hypothesis, I propose to perturb CMT arrays using the MT-depolymerising drug oryzalin. In addition, I propose to silence *KTN1* gene expression, since the severing protein is required for CMT reorientation, using an artificial microRNA (amiRKTN1) that is Dexamethasone-inducible.

2. Materials and Methods

2.1. Chemicals

All chemicals were sourced from Sigma-Aldrich unless specifically mentioned.

2.2. Buffers, Media and Solutions

Buffer, media and solutions used for my experiments, were prepared based on the protocols from (Sambrook and Russell, 2001).

2.3. Plant Materials and Growth Conditions

2.3.1. Plant Material

A. thaliana plants of the ecotype Columbia (Col-0) and *C. hirsuta* reference accession Oxford (Ox) (specimen voucher Hay *et al.*, 2014) were used as wild-types in this study. The plants were grown on soil or 0.5 x Murashige and Skoog medium (MS) (Murashige and Skoog, 1962).

A. thaliana and *C. hirsuta* 35S::*GFP:TUA6* transgenic lines are described previously (Ueda *et al.*, 1999; Hofhuis *et al.*, 2016).

2.3.2. Plant Growth Conditions

After stratifying in 2 ml 0.1 % Agar for seven days in the dark at 4 °C, the seeds were sown on moist soil and transferred to long day conditions (18 h at 20 °C, 6 h at 16 °C) in climatic chambers. Propagator lids were removed post germination.

2.4. Bacteria Strains

The *E. Coli* strains DH5α and DH10b were used for plasmid amplification. For plant transformation, *A. tumefaciens* GV3101 (Koncz and Shell, 1986) was used.

2.5. Oligonucleotides

The following list shows oligonucleotides used in this project for sequencing or amplification via PCR or RT-qPCR. All oligonucleotides were ordered from Invitrogen by Thermo Fischer Scientific.

Table 1: Table of oligonucleotides used in this project.

Primer	Sequence
GW0001_KTN1_F	CAAACACACGCTCGGACGCA
GW0002_KTN1_R	CCCCATGGCGATGCCTTAAATA
GW0003_qPCR_KTN1_At-Ch_F	CGCCATTGCTCAGATCAACAAGC
GW0004_qPCR_KTN1_At_R	TGCTTCACAACCTCCGTCTCTTCC
GW0005_qPCR_KTN1_Ch_R	GGAAGAGACGGAAGTTGTAAAGCA
GW0006_KTN1-interfer-Chr5_At-1_F	ACGAGGCTAGCGTTGGATTGTG
GW0007_KTN1-interfer-Chr5_At-1_R	GTGAATAGGCCGAGATGGGAAGA
GW0008_KTN1-interfer-Chr5_At-2_F	CGGCGAATATGAAACGGCCAAC
GW0009_KTN1-interfer-Chr5_At-2_R	CTTCGCTCCCAGATGAGGGAATC
GW0010_KTN1-interfer-Chr5_Ch-1_F	ACGCGGCTGGCGTTGGATTGTG
GW0011_KTN1-interfer-Chr5_Ch-1_R	GTGAATCGGCCGAGATGGGGAGA
GW0012_KTN1-interfer-Chr5_Ch-2_F	CGGCGAATATGAAACGGCCAAC
GW0013_KTN1-interfer-Chr5_Ch-2_R	CCTTCTCTCCCAGATGAGGGAATC
GW0014_KTN1-interfer-Chr6_At-1_F	AAACAGGCATTCGACGCTGGTG
GW0015_KTN1-interfer-Chr6_At-1_R	GAGTGTTTCCCACCGAGACAACT
GW0016_KTN1-interfer-Chr6_At-2_F	CGCAGCGAGTTTATCTTTGATCCG
GW0017_KTN1-interfer-Chr6_At-2_R	GCCTTGAATTCAGTTGTGCGTGT
GW0018_KTN1-interfer-Chr6_Ch-1_F	AAACAGCATTTGATGCAGGTG
GW0019_KTN1-interfer-Chr6_Ch-1_R	GAGTGTTTCCCACCGAGACAACT
GW0020_KTN1-interfer-Chr6_Ch-2_F	CGAATGAGTTTATATTTGATCCG
GW0021_KTN1-interfer-Chr6_Ch-2_R	GCTATGAACTCTGTTGTGCGTGT
GW0022_qPCR_KTN1_altern_D_AT_R	GAAGAGACGGAAGTTGTGAAGCAA
GW0023_qPCR_KTN1_altern_D_Ch_R	GAAGAGACGGAAGTTGTAAAGCAA
GW0024_qPCR_KTN1_altern_G_AT_R	GTTGTGAAGCAATTGGATGCAGAG
GW0025_qPCR_KTN1_altern_G_Ch_R	GTTGTAAAGCAATTGGATGCAGAG
GW0026_genotyping_PI5_F	AAGCAGGCTCCGAATTCGCCC
GW0027_genotyping_PI5_R	GAAAGCTGGGTCTGAATTCGCCCTT
GW0028_qPCR_KTN1_altern_D_AT_R	TTGCTTCACAACCTCCGTCTCTTC
GW0029_qPCR_KTN1_altern_At_R	GGTATTGATAGGTGGAGAAGCAGCG
GW0030_qPCR_KTN1_altern_At_R	GACGCCCAGTGGGAGCTTCT
GW0031_qPCR_KTN1_altern_D_Ch_R	TTGCTTTACAACCTCCGTCTCTTC
GW0032_qPCR_KTN1_altern_Ch_R	GATGATTTAGTGTTGTTGATGGGCGG
GW0033_qPCR_KTN1_altern_Ch_R	GCACGACGGCCAGTGGGA
GW0034_KTN1-interfer-Chr5_Ch-a_F	GAGAGCGGAGATGGCGATAGAG
GW0035_KTN1-interfer-Chr5_Ch-1_R	TCTCCCCATCTCCGGCCGATTACAC
GW0036_KTN1-interfer-Chr5_Ch-b_F	GAGCGGACTTCGTAATTGAAACG
GW0037_KTN1-interfer-Chr5_At-1_R	TCTTCCCATCTCCGGCCTATTACAC
GW0038_KTN1-interfer-Chr5_At-a_F	GGAGATGGTGATAGAGATGGAAGACTGA

Primer	Sequence
GW0039_KTN1-interfer-Chr5_At-b_F	CGGTGATTGAAACGGCGAGAG
GW0040_KTN1-interfer-Chr6_Ch-a_R	GCCATCTATGCAACATTTTCGACAAG
GW0041_KTN1-interfer-Chr6_Ch-b_R	CGTGAGGCATTTTTCTCGAGGTC
GW0042_KTN1-interfer-Chr6_At-a_R	TTCCCGTCCTGCCATTATGCAAC
GW0043_KTN1-interfer-Chr6_At-b_R	TCTCTAGGTCCTCGGATTTCTGGAC

2.6. Genetic Methods

2.6.1. Transgenic Constructions

Using a pCR8/GW/TOPO-TA-Cloning Kit, an artificial microRNA designed to silence KTN1 (amiRKTN1, kindly provided by A. Maizel) was inserted in a Dexamethasone inducible two-component system consistent of a constitutive promotor AtRPS5 α expressing chemically responsive transcription factor (LhGR) and target promotor (pOp6) driving amirKTN1 expression (Moore *et al.*, 2006). The construct was then transformed in *C. hirsuta* and *A. thaliana* WT and 35S::*GFP:TUA6* lines of both species.

2.6.2. Plant Transformation

Plasmids containing T-DNA were introduced into *A. tumefaciens* strain GV3101 by electroporation. A single colony was grown in 5 ml of Luria Broth (LB) medium together with the respective antibiotics overnight at 28 °C, which was then used to inoculate a 1 l culture. These cultures were grown to an optical density of OD_{600 nm} = 0.7 – 1. Cells were re-suspended in transformation buffer (5 % sucrose, 10 mM MgCl₂, 1x Gamborg's Vitamins (Sigma Laboratories), 100 ng/ml 6-benzylaminopurine, 0.03 % Silwet-77). Plasmids were transformed via floral dip into 30 plants of *C. hirsuta* Ox, *C. hirsuta* 35S::*GFP:TUA6*, *A. thaliana* Col-0 and *A. thaliana* 35S::*GFP:TUA6* each. Inflorescent plants were submerged in the solution for 5 min, after which the plants were laid on their side in the dark and overnight at

room temperature. The next day the plants were transferred to the greenhouse and placed upright.

2.6.3. Selection of Transgenic Plants

Transgenic plants carrying the BASTA resistance gene were selected by spraying 400 μ M BASTA herbicide (Basta, 200 g/l glufosinat ammonium, Bayer) on seedlings. To select the second generation of transformed plants (T2), approx. 100 seeds of 9-12 independent lines of each transformed species were sowed and selected on BASTA resistance. The selection of the T3 revealed 5 *C. hirsuta* 35S::*GFP:TUA6*, *amiRKTN1* lines with single copy transgene loci, and 16 *A. thaliana* 35S::*GFP:TUA6*, *amiRKTN1* lines, respectively.

2.6.4. Sterilisation of Transgenic Seeds

Seeds were sterilised using 70 % ethanol and 0.5 % Triton X-100 for 2 min, followed by a wash with 99 % ethanol for 2 min and left to dry under a fume hood overnight.

2.6.5. Dexamethasone (Dex) Induction

I induced expression of *amiRKTN1* by dipping branches carrying a marked pod of 7 mm (stage 16) in a Dex solution (100 μ M Dex and 0.03 % Silwet) and control solution (water and 0.03 % Silwet) for 10 min, respectively. 24 h after dipping, the plants were analysed via confocal laser scanning microscopy (CLSM) in 24 for four days in a row and on the last day after sixteen treatments in total (16 days).

2.7. Molecular biology methods

2.7.1. Genomic DNA Extraction

To extract plant genomic DNA for PCR analysis, one to three fruit pods were mechanically homogenised in 2 ml Eppendorf tubes by adding 400 µl extraction buffer (250 mM TRIS buffer pH 7.5, 250 mM NaCl, 25 mM EDTA, 0.5 % SDS). The tubes were then vortexed for 2 min. Samples were spun afterwards at full speed in an Eppendorf micro centrifuge for 5 min and 300 µl of the supernatants were removed to fresh tubes containing 300 µl isopropanol at room temperature. The tubes were inverted and incubated at room temperature for approximately 5 min to precipitate DNA. Afterwards, the tubes were spun at full speed for 10 min, supernatant was discarded and DNA was air-dried. DNA was then re-dissolved by pipetting up and down carefully in 100 µl TE-Buffer (10 mM TRIS Buffer pH 8.0, 1 mM EDTA), kept at 4 °C overnight.

2.7.2. RNA Isolation

Total RNA was extracted using the Spectrum Plant Total RNA Kit (Sigma, STRN50), treated on-column with DNaseI (Sigma, DNASE70).

2.7.3. Gel Electrophoresis

Depending on fragment length, digested, amplified PCR products were visualised on a 1.5-3 % agarose (Invitrogen, Thermo Fischer Scientific) 1x TAE gel containing 1:20000 gel red and run at 120 V for 40-90 min.

2.7.4. Oryzalin Treatment

C. hirsuta and *A. thaliana* fruit pods of 7 mm (stage 16) were dipped in an Oryzalin solution (125 µM Oryzalin, 0.03 % Silwet) and control solution (125 µM

Dimethylsulfoxid (DMSO), 0.03 % Silwet) for 10 min, respectively. 24 h after dipping, the plants were analysed via confocal laser scanning microscopy every 24 for four days in a row and on the last day after sixteen treatments in total (16 days).

2.7.5. Osmotic treatment

Valves of mature *C. hirsuta* fruit, previously treated with Dex or Oryzalin, were cut to fragments of 3-4 mm length and fixed in a petri dish using adhesive tag. After staining with 1 % propidium iodide (PI) in deionized water for 5 min, the fruit's exocarp cells were imaged via CLSM. Subsequently, the water was removed with a tissue and the valve segments were submerged in a 1 M NaCl solution containing PI for 45 min. The salt solution was removed with a tissue and replaced by deionized water before the fruit segment was analysed via CLSM again. To facilitate orientation and recover the same cells of the previously performed CLSM analysis, the sample was kept on the microscope.

2.7.6. β -glucuronidase Staining with X-Gluc substrate (GUS staining)

Plant tissue was fixed in 90 % cold acetone for 20 min, washed twice with water and stained via vacuum infiltration for 15 min and overnight storage at 37°C in the dark with freshly prepared staining solution (50 mM sodium phosphate buffer, 0.2 % Tritonx-100, 2 mM X-Gluc, 5 mM ferrocyanide and ferricyanide salts). After a wash with 20 %, 35 % and 50 % ethanol for 30 min each, the tissue was exposed to the post fixing solution (50 % ethanol, 3.7 % formaldehyde, 5 % acetic acid) for 30 min. Then, the tissue was washed with 70 %, 80 % and 90 % ethanol for 30 min each. Samples were visualised using light microscopy.

2.8. Analytical Methods

2.8.1. PCR

A 25 µl reaction mix was used containing 5 µM forward and reverse primer, 10 mM dNTP, 10x PCR buffer, polymerase (Taq Amplicon® or Phusion®) and DNA template in water.

Reactions took place in a SensoQuest LabCycler using the following programme: 95 °C for 3 min, 30 cycles of 95 °C for 10 s, 53 °C for 30 s and 72 °C for 30 s, then 72 °C for 3 min followed by the infinite storage temperature of 4 °C.

2.8.2. Quantitative Reverse Transcriptase PCR (RT-qPCR)

Gene expression levels were quantified in tissue samples from intact *C. hirsuta* and *A. thaliana* fruits at developmental stages 15, 16 and 17. All samples were immediately frozen in liquid nitrogen and stored at -80°C before processing. 1 µg of eluted RNA was used for complementary DNA (cDNA) synthesis using the SuperScriptIII kit (Invitrogen). cDNA templates were used in qPCR reactions to amplify amiRKTN1 using Power SYBR Green Supermix (Applied Biosystems) on a ViiA7 machine (Applied Biosystems). Each reaction was made in technical triplicates and three biological samples were used per genotype. The efficiency of each set of primers and calculation of the gene expression level was determined according to the manufacturer's protocol (Applied Biosystems, Thermo Fischer Scientific).

Transcript levels for each gene were calculated using the formula $(E_{\text{target}})^{-\Delta C_P \text{target}(\text{control-sample})} / (E_{\text{ref}})^{-\Delta C_P \text{ref}(\text{control-sample})}$ (Pfaffl 2001) and expression of *KTN1* was normalized to the reference gene *Clathrin/AP2M* (CARHR174880). The error bar represents the standard error of mean calculated on biological experiment repetitions. Primer sequences are listed in Table 1.

2.8.3. Valve coiling analysis

To quantify the coils, a lateral view of the coiled valve was used and only complete concluded coils were counted. To quantify the tension of the coiled valves, a top view was used. By using Image J, a circle was fit inside of the coil. The area of the circle was used to calculate the diameter via the following formula:

$$diameter = 2 * \sqrt{\frac{area}{\pi}}$$

2.9. Microscopy Techniques

2.9.1. Light Microscopy and Imaging

A Zeiss Axiophot compound microscope equipped with a Leica DFC490 camera and 20x and 40x objectives was used to image fresh tissues.

Pictures of coiled valves were captured from the aerial perspective with a Nikon DS800 digital camera and processed with Image J.

2.9.2. Confocal Laser Scanning Microscopy (CLSM)

A Leica DM6000 TCS SP8 microscope equipped with a HyD detector was used with a long distance 63x/0.9 water immersion objective to visualize GFP::TUA6 marked CMT (excitation: 488 nm, emission: 495-545 nm). Samples were carefully fixed with adhesive tags to the bottom of small petri dishes and mounted in water. Z--stacks were acquired with 0.2 μ m interval.

2.10. Bioinformatics

2.10.1 Primer Design

Primers were designed using Invitrogen Vector NTI Advance™ 11.0, NCBI Primer-BLAST and Primer3 (Rozen and Skaletsky, 2000). DNA sequencing data was analysed using ContigExpress (Invitrogen Vector NTI Advance™ 11.0) Sequence

comparisons were conducted using ContigExpress and AlignX (Invitrogen Vector NTI Advance™ 11.0) (Larkin *et al.*, 2007; Goujon *et al.*, 2010), analysis of multiple sequence alignments using <http://multalin.toulouse.inra.fr/multalin/> (Corpet, 1988). The primers used throughout this thesis are listed in Table 1. All primers were synthesised by Invitrogen, Thermo Fischer Scientific.

DNA sequences and genome annotations for *A. thaliana* were retrieved from The *Arabidopsis* Information Resource at www.arabidopsis.org (Lamesch *et al.*, 2012). The sequences from *C. hirsuta* were translated *in silico* from database and sequencing DNA data using Invitrogen Vector NTI Advance™ 11.0.

2.10.2 MorphoGraphX

To quantify the degree and direction of cortical microtubule alignment, CLSM image stacks of 35S::GFP:TUA6 expression in exocarp cells were loaded into MorphoGraphX software and their surfaces extracted with the marching-cube algorithm (Barbier de Reuille *et al.*, 2015). The surface mesh was subdivided into a fine mesh and the surface-associated signal was projected on to this mesh to allow for cell segmentation with the watershed 2D tool. The GFP signal was re-projected within the extracted surface, depending on the signal depth in the sample. The principal orientation of the GFP signal (magnitude) within each cell was computed using the Fibril orientations algorithm (Barbier de Reuille *et al.*, 2015). The angles of CMT alignments in relation to the longitudinal fruit axis were calculated using the compute fibril angles process. Images were acquired by CLSM and light microscopy.

The aspect ratio was analysed via the shape analysis process run after a custom Bezier was created. The data of the x and y coordinates were saved via heatmap and the aspect ratio was calculated by dividing the values of the long axis (y axis) by the short axis (x axis).

To determine the growth tensor, 3D segmented cells of two different time points were directly compared. Therefore, the cells of the early time point were marked as parents so that the labelling of the segmented cells can be adopted to the subsequent time point. The length of the segmented cells was calculated by fitting ellipsoids in the segmented cells and adding together the lengths of the longitudinal axis. The cell volume was determined via heat map process.

Stomata are not taken into consideration for further calculations

3 Results

3.1. Staging Fruit Development in *C. hirsuta* and *A. thaliana*

A. thaliana and *C. hirsuta* have very similar fruits but very different seed dispersal strategies (Hay *et al.*, 2014). *A. thaliana* pods shatter passively, whereas *C. hirsuta* disperses its seeds ballistically by explosive coiling (Hay *et al.*, 2014; Hofhuis *et al.*, 2016). I characterized fruit pod development in *A. thaliana* and *C. hirsuta* to ensure a reliable definition of developmental stages that allows me to make meaningful comparisons between species. I analysed *A. thaliana* ecotype Col-0 and *C. hirsuta* ecotype Ox, which are the ecotypes used throughout my thesis, and grew all plants together under standard conditions. I used the main inflorescence stem of each plant for analysis, which consists of a developmental series of fruit, and conducted each analysis when the oldest pod on the main stem reached stage 18. I then categorised all fruit pods on the main stem according to their developmental stage, based on the staging described in The Arabidopsis Book (Roeder and Yanofsky, 2006).

Comparing the fruits of both species emphasises their morphological similarities (Figure 5). The last stages of flower development in both species are stage 12, when the petals elongate to reach the length of the medial stamens and the gynoecium becomes ready for fertilisation; and stage 13, when the flower opens and anthesis occurs (Figure 5; Roeder and Yanofsky, 2006; McKim *et al.*, 2017). Fruit development begins after pollination occurs at stage 14, and by stage 15 the gynoecium has elongated above the stamens (Figure 5). By stage 16 the fruit pod has doubled in length and other floral organs abscise (Figure 5). The fruit elongates considerably during stage 17 to reach its final length (stage 17a) and begins to grow in width (stage 17b) (Figure 5). It is at this stage that differences between the fruits of *A. thaliana* and *C. hirsuta* become more obvious. The valves of *A. thaliana* fruit are

very curved in cross-section and attach to a narrow replum, whereas the valves of *C. hirsuta* fruit are quite flat and attach to a wider replum (Figure 5). The very curved valves of *A. thaliana* fruit do not touch the seeds, whereas the flatter valves of *C. hirsuta* fruit press against the seeds, which are considerably larger in *C. hirsuta* than in *A. thaliana* (Hay *et al.*, 2014). Thus, the *C. hirsuta* valves become slightly corrugated, indicating the positions where the seeds are pressed against the valve (Figure 5). Stage 18, when the fruits yellow (Figure 5), is the final stage of *C. hirsuta* fruit development as fruits are competent to explode and disperse seeds from stage 17b onwards. In comparison, *A. thaliana* fruits continue to develop through stages 19 and 20 where dehiscence occurs, the fruits dry, and seed dispersal occurs passively when the pod shatters upon touch (Roeder and Yanofsky, 2006).



Figure 5: Phenotypic comparison of different fruit developmental stages of *A. thaliana* and *C. hirsuta*, respectively. Developmental stages were determined according to the stages described in *The Arabidopsis Book* (Roeder and Yanofsky, 2006). Since fruit development is so similar between *A. thaliana* and *C. hirsuta*, the developmental stages described in *The Arabidopsis Book* (Roeder and Yanofsky, 2006) can be applied to both species. Scale bar: 20 μ m

The focus of my work is to characterize the dynamics of CMT in valve exocarp cells. CMT alignment in these cells is known to reorient during fruit pod development and this is predicted to play an important role in contraction of the exocarp cell layer in *C. hirsuta* (Hofhuis *et al.*, 2016). To monitor CMT dynamics I used stably transformed *C. hirsuta* and *A. thaliana* 35S::*GFP:TUA6* marker lines in Ox and Col-0 ecotypes, respectively (Hofhuis *et al.*, 2016). To assess whether the experimental set-up that I used for imaging was affecting fruit development or not, I first characterized fruit development in these transgenic lines. I used adhesive tags to fix single developing fruit (stage 12 - stage 13) of *A. thaliana* and *C. hirsuta* on a microscope slide. The slide was fully supported by attachment to a wooden stake, which allowed the plant to grow normally (Figure 6). To monitor growth and development of these fruit, I measured the length and width of the fruit pods daily throughout development. I compared two individual plants of *A. thaliana* and *C. hirsuta* wild-type and 35S::*GFP:TUA6* marker lines of both species, respectively. I analysed the data by pooling replicate plants of each species (n=2), since I found little difference in fruit growth and development between individuals of wild-type and 35S::*GFP:TUA6* genotypes (Figure 7 and Table 2). In comparison to a previous report that 35S::*GFP:TUA6* caused right-handed helical growth of juvenile *A. thaliana* leaves (Abe *et al.*, 2003), I found no obvious phenotypic differences between wild-type and 35S::*GFP:TUA6* plants in *A. thaliana* or *C. hirsuta*. I plotted average values for fruit length and width (n=4 for each species) against defined developmental stages (Figure 8) and determined the range of fruit lengths that describes each different fruit developmental stage (Table 3). I subsequently used fruit length to assign developmental stage, according to this analysis (Table 3), throughout my work. Based on my comparison of fruit development in plants grown in standard conditions (Figure 5) versus plants grown in the conditions used for imaging (Figure 8), I conclude that *A. thaliana* and *C. hirsuta* 35S::*GFP:TUA6*

marker lines can be used to image CMT dynamics, without affecting wild-type fruit development.

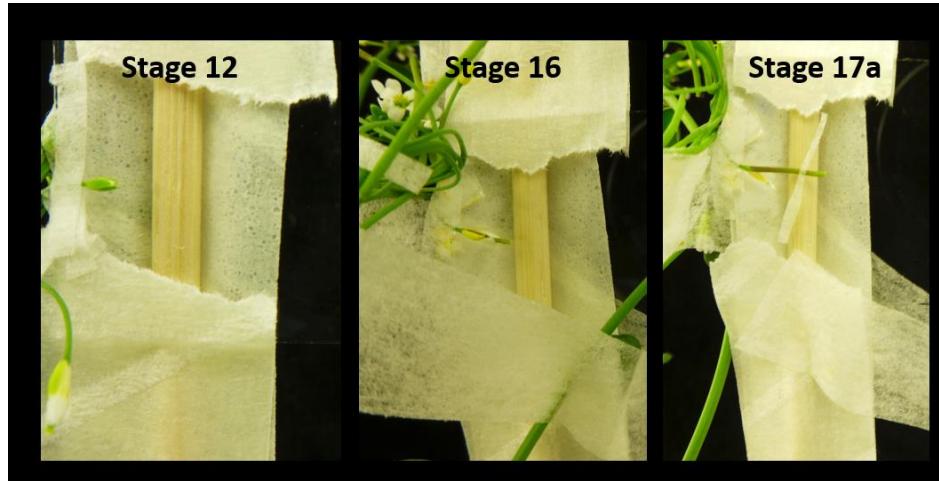


Figure 6: Single *A. thaliana* fruit pod fixed to microscopic slide with an adhesive tag to monitor its growth. The slide is fixed to a wooden stick to adjust the height and avoid rupture or developmental perturbations.

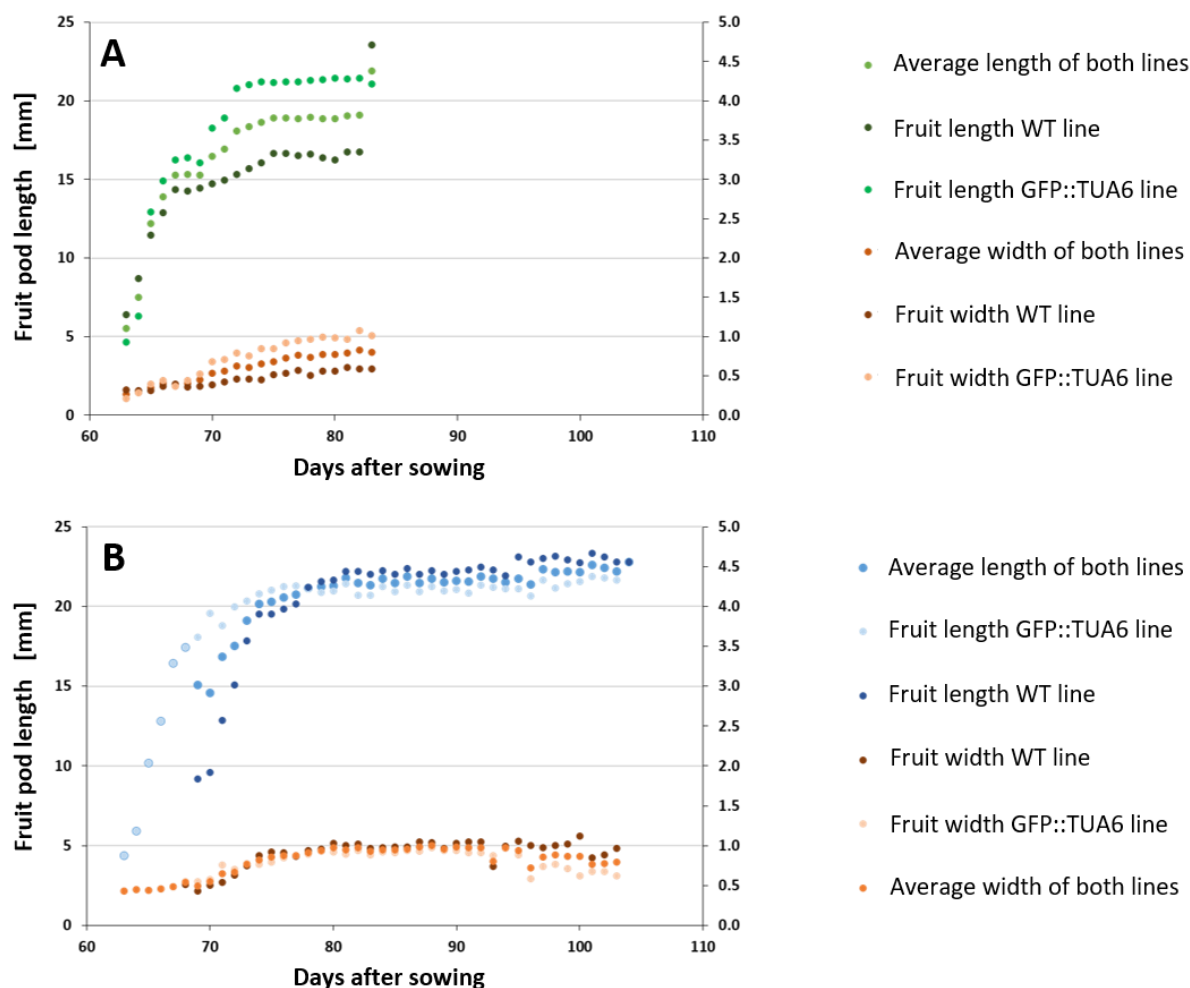


Figure 7: Growth of *C. hirsuta* (A) and *A. thaliana* (B) wild type (WT) and 35S::GFP:TUA6 marker lines. Fruit were monitored from stage 12 through 18.

Table 2: Overview of *C. hirsuta* and *A. thaliana* fruit growth. Average growth rate is calculated by dividing mean pod length (final length – initial length) by number of days of growth. The t-test shows that the means of WT and 35S::GFP:TUA6 lines of both species do not differ significantly.

Species	Line	Average final fruit pod length [mm]	T-Test on average final pod length	Average fruit pod growth rate [mm/day]	T-Test on average fruit pod growth rate	
<i>C. hirsuta</i>	Oxford	20.07 ± 0.27	0.30	0.69 ± 0.14	0.45	n=2
	35S::GFP:TUA6	20.52 ± 0.22		0.86 ± 0.24		n=2
<i>A. thaliana</i>	Col-0	22.27 ± 0.26	0.56	0.71 ± 0.09	0.23	n=2
	35S::GFP:TUA6	21.64 ± 0.21		0.52 ± 0.11		n=2

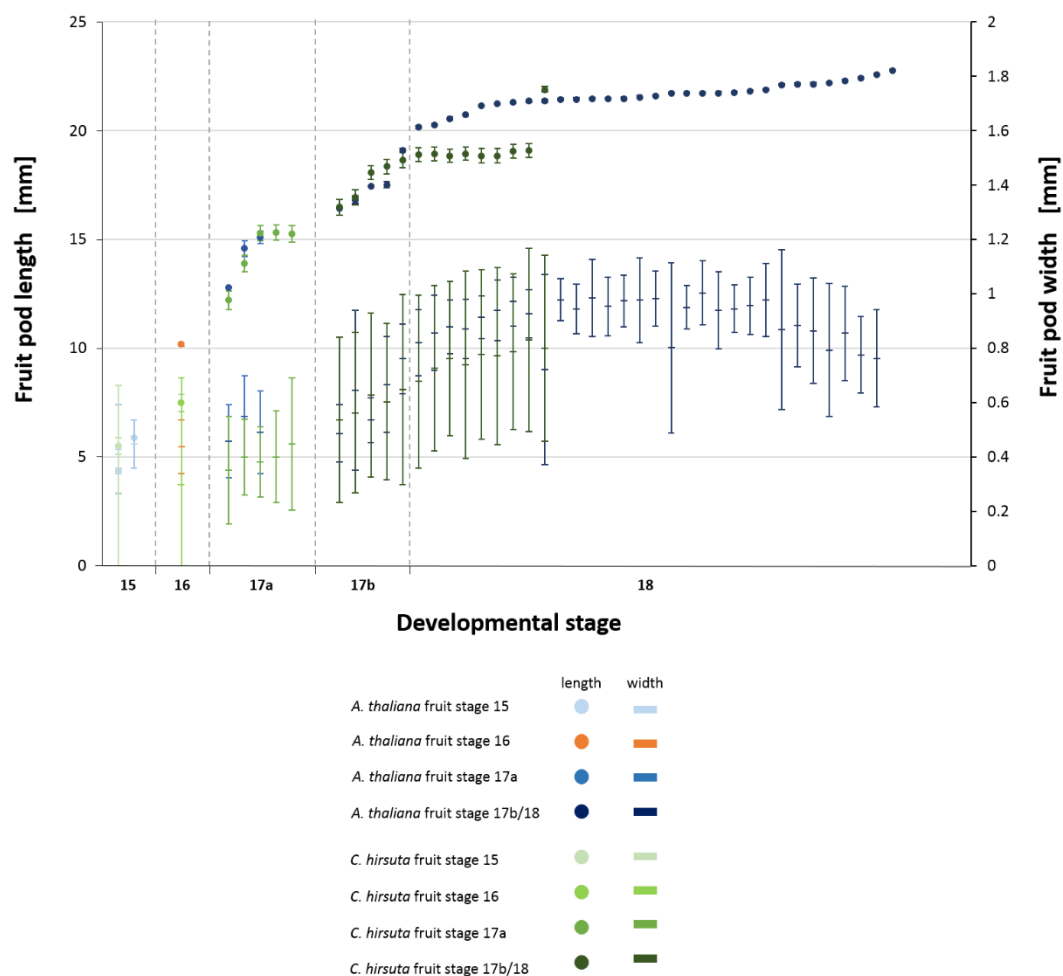


Figure 8: Comparison of fruit growth between *C. hirsuta* and *A. thaliana* WT and 35S::GFP:TUA6 marker lines, respectively, according to the different fruit pod stages. The dots indicate fruit length and the transverse bars indicate fruit width. Both species show similar growth patterns in each stage and are therefore comparable.

Table 3: Fruit development stages described by fruit length according to data shown in Figure 8.

Stage 15	Stage 16	Stage 17a	Stage 17b - 18
2 – 6 mm	7 – 11 mm	12 – 16 mm	16 – 25 mm

To characterise CMT alignment, I first imaged *35S::GFP:TUA6* signal in the valve exocarp using CLSM to generate image stacks. I then used these image stacks to quantify CMT angles relative to the longitudinal fruit axis by using MorphoGraphX software. The distribution of CMT angles were plotted by frequency under each image where the orientation and magnitude of CMT alignment is shown by a red line in each cell (Figure 9). Both species show a reorientation of CMT alignment, from transverse to longitudinal, during stage 16 (Figure 9).

The magnitude of CMT alignment is higher in *C. hirsuta* than *A. thaliana* exocarp cells throughout fruit development, as indicated by the longer red lines (Figure 9). In *C. hirsuta* fruit, CMT angles are restricted between 60 – 100° from stages 13 through 15, indicating a strongly transverse orientation (Figure 9). Then, in stage 16 and 17a, CMT angles are distributed from 0 – 90°, indicating no preferential alignment (Figure 9). Finally, in stage 17b and 18, CMT angles are mostly distributed between 0 – 20°, indicating a strongly longitudinal orientation (Figure 9).

The same trend in CMT dynamics was also observed in *A. thaliana* exocarp cells through fruit development. CMT alignment was mostly transverse in stage 13 and shifted to a longitudinal alignment in stage 17a (Figure 9). However, the magnitude of CMT alignment was considerably lower than in *C. hirsuta* cells, as seen by the shorter red lines (Figure 9). Also, CMT angles were distributed from 0 – 90° in stages 14, 15 and 16, indicating no preferential alignment over a longer period of development than *C. hirsuta* cells (Figure 9).

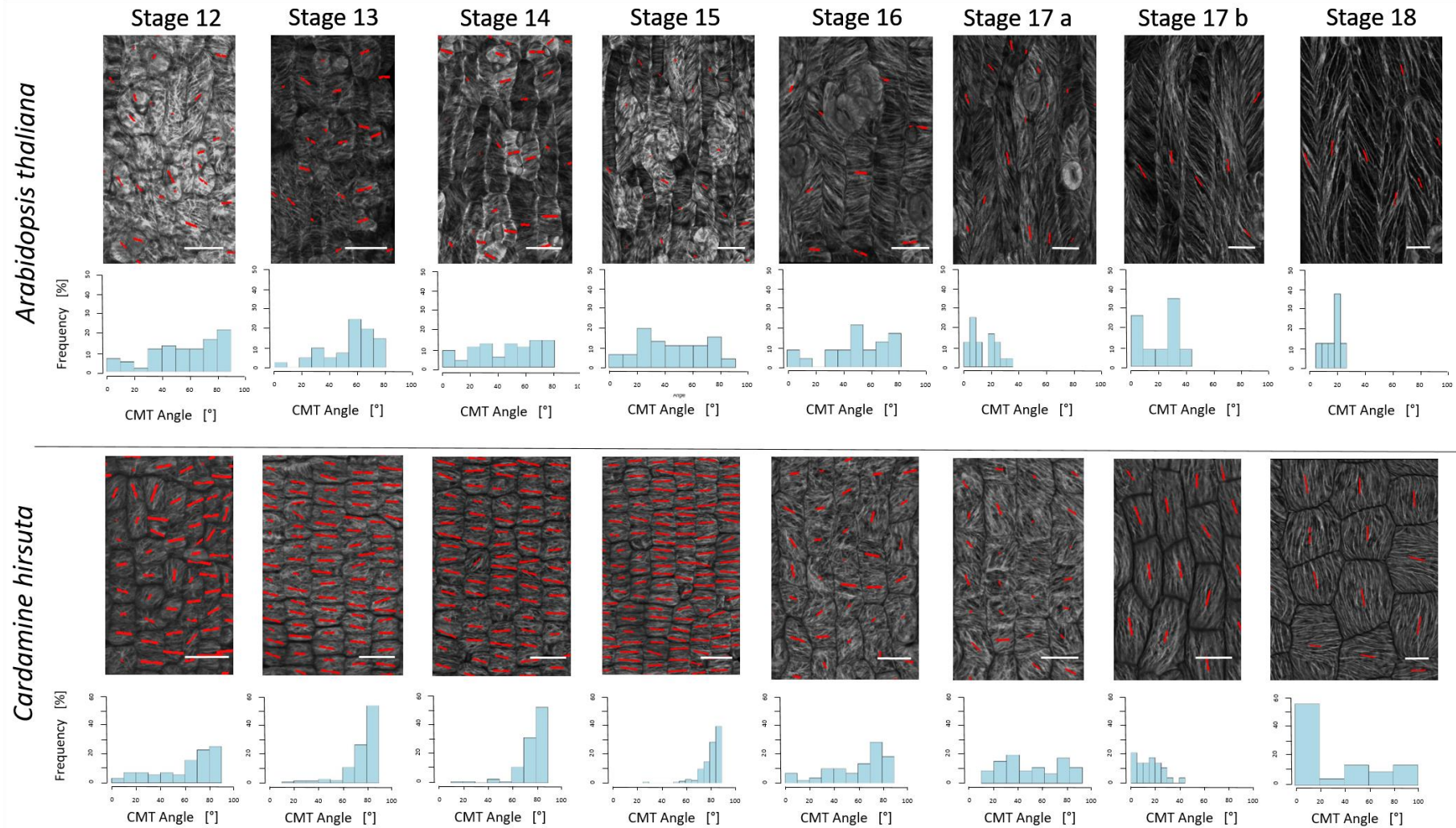


Figure 9: CMT alignment in exocarp cells at different fruit developmental stages in *A. thaliana* and *C. hirsuta*. The length of the red line represents the extent of CMT organisation and its orientation represents the average CMT alignment of the cell. Frequency histograms plot the frequency of cells with average CMT angles in bins of 10° from 0 – 90°. Scale bar: 25µm

Another obvious difference between *C. hirsuta* and *A. thaliana* exocarp cells is the density of cells with well-aligned CMT arrays in *C. hirsuta* versus *A. thaliana* i.e. many more red lines within the same area of exocarp tissue in *C. hirsuta* than *A. thaliana*, especially in stages 12 through to 16 (Figure 9). This is not only due to a difference in the degree of CMT alignment, but also to a difference in exocarp cell shape and size. *A. thaliana* exocarp cells are rectangular, and elongate in length throughout fruit development, becoming so elongate by stages 17b and 18 that single cells extend beyond the field of view in Figure 9. In contrast to this, *C. hirsuta* exocarp cells are shorter in length and square in shape during the early stages of fruit development (stages 12 – 15, Figure 9). These cells elongate to become rectangular in stage 16, before expanding in width to become square by stage 18 (Figure 9).

To quantify this change in exocarp cell shape during fruit development, I calculated the aspect ratio of all cells in a 2-dimensional plane. To do this, I divided the length of a cell, aligned to the longitudinal axis of the fruit, by its width. This way, a perfect square-shaped cell has an aspect ratio of 1, whereas the aspect ratio of an elongate, rectangular-shaped cell is > 1 , and a wide, rectangular-shaped cell is < 1 (Figure 11).

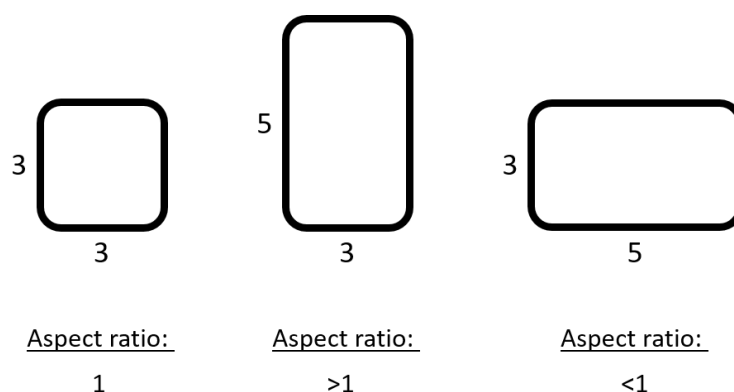


Figure 10: Schematic explanation of the aspect ratio.

By visualising the aspect ratio of exocarp cells in *A. thaliana* and *C. hirsuta* fruit, dynamic changes in cell shape are visible through development (Figure 12). *A. thaliana* cells show an average aspect ratio of 2.16 ± 0.45 at stage 12, which describes an elongate, rectangular cell shape (Figure 11). The aspect ratio of *A. thaliana* cells continues to increase throughout fruit development to reach an average aspect ratio of 7.13 ± 0.47 at stage 18 (Figure 11). Therefore, *A. thaliana* exocarp cells maintain an elongate, rectangular shape throughout all stages of fruit development. In contrast to this, *C. hirsuta* exocarp cells are close to square-shaped at stage 12, exhibiting an average aspect ratio of 1.08 ± 0.45 (Figure 11). Then in stages 13 to 15, the average aspect ratios change to values below 1 (0.57 ± 0.28 , 0.58 ± 0.33 and 0.65 ± 0.27), indicating that the cells have a wide, rectangular shape (Figure 11). In stages 16 and 17a, the average aspect ratios change again to values greater than 1 (1.28 ± 0.35 and 1.28 ± 0.58), indicating an elongate, rectangular cell shape (Figure 11). In stage 17b, the average aspect ratio further increases to 1.86 ± 0.51 , indicating a more elongate, rectangular cell shape (Figure 11). By stage 18, the average aspect ratio of exocarp cells changes to 1.18 ± 0.56 , indicating an abrupt change to square-shaped cells (Figure 11). Therefore, in contrast to *A. thaliana*, the shape of *C. hirsuta* exocarp cells changes dynamically through development. Two important differences are: (1) At stage 15, just prior to when the fruit starts to elongate considerably through stages 16 and 17 (Figure 5), *A. thaliana* exocarp cells are very elongated whereas *C. hirsuta* exocarp cells are very short (Figure 11). (2) At stages 17b and 18, when the fruit starts to increase in width (Figure 5), *C. hirsuta* exocarp cells increase in width to change shape from elongate to square, while *A. thaliana* cells continue to elongate (Figure 11).

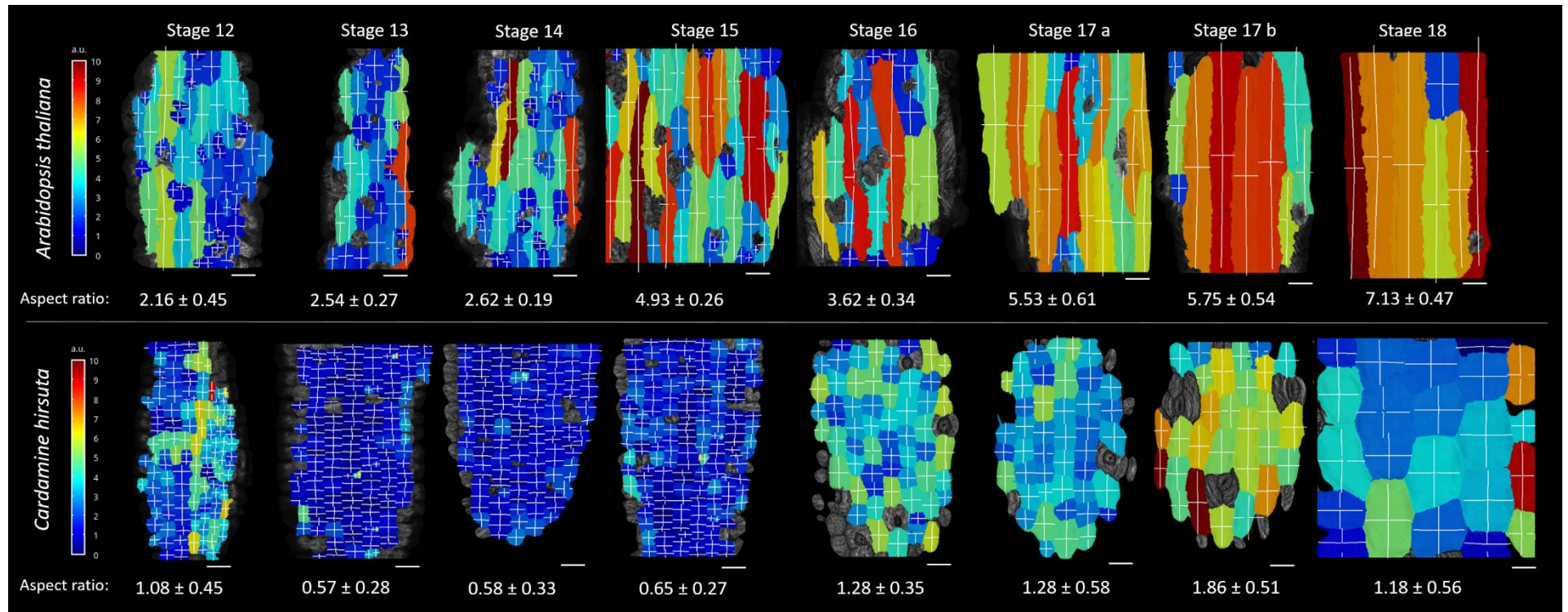


Figure 11: Aspect ratio (shown as heat map) for exocarp cells of *A. thaliana* and *C. hirsuta* during fruit development. Average aspect ratios for all cells are shown below the image for each stage. The crosshairs indicate the sizes of the cells in transverse and longitudinal direction. Scale bars: 20 μm .

3.2. Defining the Time Point of CMT Reorientation

The alignment of CMTs indirectly controls the direction of cell growth by guiding the orientation of cellulose microfibril deposition in the cell wall (Paredes et al 2006; Mirabet et al. 2017). The change in direction of exocarp cell growth from longitudinal to transverse, between stages 17b and 18 of *C. hirsuta* fruit development (Figure 11), is associated with a change in CMT alignment (Figure 9). Therefore, by stage 18, *C. hirsuta* exocarp cells have acquired a square shape and longitudinally aligned CMT that are predicted to align cellulose microfibrils in this same direction. These two features, cell shape and cell wall anisotropy, are key parameters for exocarp cell contraction to occur in a finite element model of this process (Figure 3, Hofhuis et al., 2016). To investigate this process further, I analysed the reorientation of CMT alignment in more detail. In the exocarp cells of both *C. hirsuta* and *A. thaliana*, CMT reorient between stages 16 and 17b (Figure 9). To investigate the precision and reproducibility of this timing, I performed live imaging of *C. hirsuta* and *A. thaliana* 35S::*GFP:TUA6* marker lines.

I imaged one specific fruit pod in five individual plants of each species, performing CLSM at time point 0 h and then every 24 h until CMT reorientation had occurred. From these image stacks, I quantified CMT alignment in relation to the longitudinal fruit axis. I started each time series when fruit length reached 7-8 mm, which correlated to fruit stage 16, where I first observed a change in the distribution of CMT angles (Figure 9 and Table 3). To summarize the data on CMT organisation in all five replicates, I pooled the data from the five individual plants and plotted the CMT angles against their frequency (Figure 12). In addition, I selected one representative image from the replicates at each time point to show in Figure 12.

At the first time point (0 h), the highest frequency of CMT angle bins were between 70 – 90° in *C. hirsuta* and *A. thaliana* exocarp cells, indicating a transverse CMT alignment in relation to the longitudinal fruit axis (Figure 12). After 24 h, the distribution of CMT angles in both species was flatter, and the magnitude of CMT alignment was lower (shorter red lines), indicating loss of this transverse CMT alignment (Figure 12). After 48 h, the distribution of CMT angles was skewed towards lower values, with the highest frequency of CMT angles between 0 – 40° in *C. hirsuta* and *A. thaliana* exocarp cells, indicating a longitudinal CMT alignment (Figure 12). After 72 h, the distribution of CMT angles was even more skewed towards lower values in *C. hirsuta*, with the highest frequency of CMT angles lying between 0 – 10° in both species (Figure 12). Thus, CMT reorientation occurred in exocarp cells of both *C. hirsuta* and *A. thaliana* within 24 h of the pods entering fruit development stage 16 (7 – 11 mm fruit length).

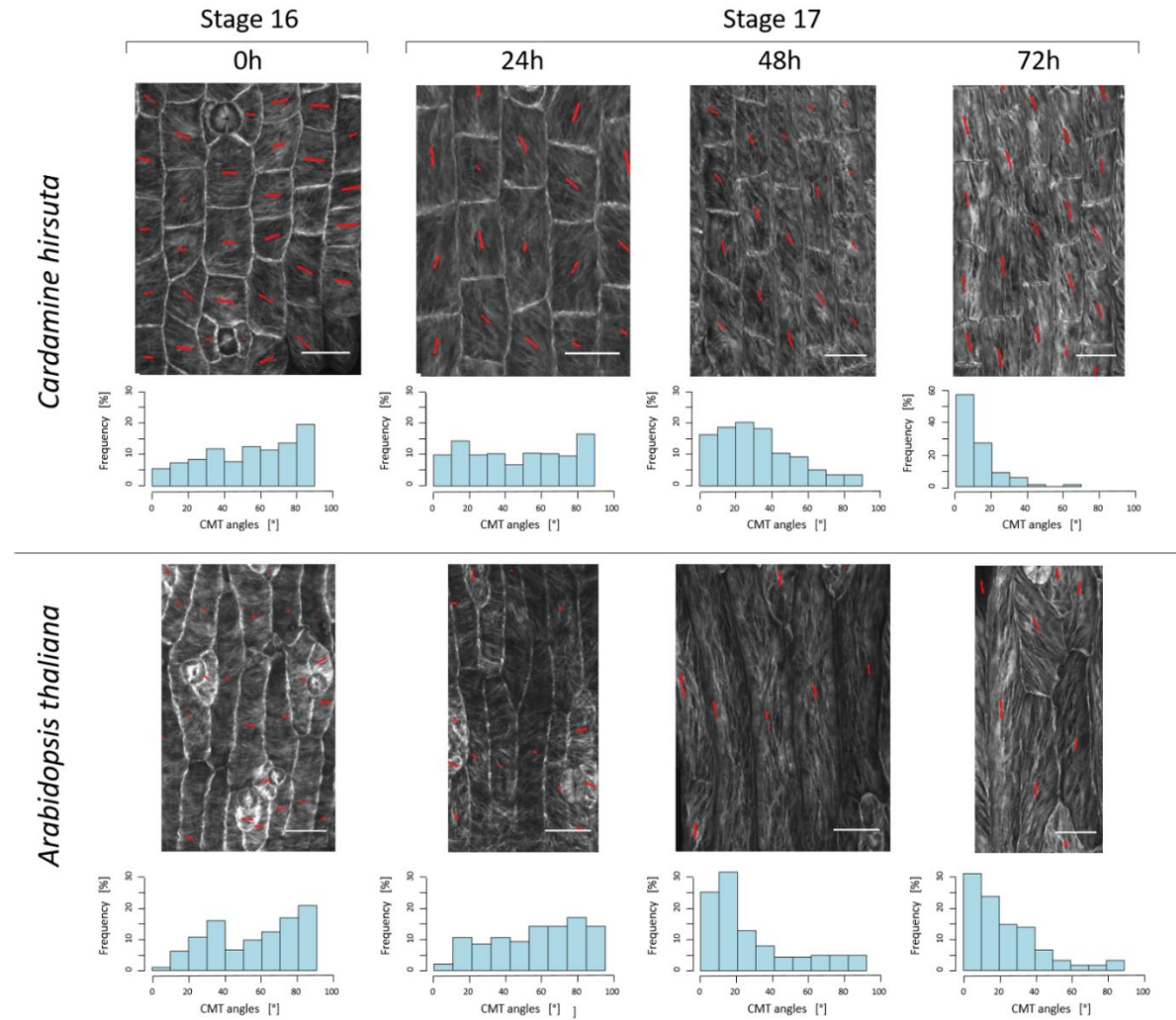


Figure 12: Time series of CMT orientation in individual fruit pods of *C. hirsuta* and *A. thaliana* 35S::GFP:TUA6 plants. The length of the red line represents the extent of CMT organisation and its orientation represents the average CMT alignment of the cell. Frequency histograms plot the frequency of cells with average CMT angles in bins of 10° from 0 – 90°. Scale bars: 25μm.

3.3. CMT Disruption with Oryzalin

CMT alignment guides the net orientation of cellulose microfibrils in a cell and therefore influences cell anisotropy (Paredes *et al.*, 2006). Exocarp cell shape and anisotropy are predicted by our modelling to be important for the cellular contraction that drives explosive pod shatter (Hofhuis *et al.*, 2016). Our observations suggest that a change in CMT alignment is associated with a change in anisotropic growth of exocarp cells in *C. hirsuta* (Figure 9, Figure 11, Figure 12 and Hofhuis *et al.*, 2016). Therefore, to test whether CMT alignment is required for explosive pod shatter, I used the herbicide oryzalin to disrupt CMTs. Oryzalin depolymerises tubulin dimers, thus inhibiting their incorporation into the MT polymer (Dostál and Libusová, 2014; Dumontet and Jordan, 2010). Since I wanted to apply oryzalin to mature fruit pods, which have a thick cuticle, I first ascertained a suitable concentration to perturb CMT in the exocarp. I added 0.03 % Silwet to all my solutions to improve the cuticular penetration (Hu *et al.*, 2010). I treated individual branches of *C. hirsuta* 35S::*GFP:TUA6* plants with different concentrations of oryzalin (50 μ M, 125 μ M, 250 μ M and 500 μ M) as well as control solutions containing DMSO for 5 min. After 24 h, I performed CLSM on random pods from each concentration of oryzalin to check whether CMT alignment was disrupted, indicated by CMT bundling (Figure 13). The control did not exhibit any effect and 50 μ M had a slight effect by decreasing the CMT density (Figure 13). However, treatment with 125 μ M oryzalin resulted in CMT bundling, which is caused by depolymerisation of tubulin dimers (Figure 13, Dostál and Libusová, 2014; Dumontet and Jordan, 2010)). This bundling is increased in the 250 μ M oryzalin treatment (Figure 13). Treatment with 500 μ M oryzalin had less effect in the pod that I analyzed for unknown reasons (Figure 13). Since I aimed to perturb CMT orientation in the fruit exocarp with minimal overall effect to the plant, I selected

125 μ M oryzalin for further experiments as this was the minimal concentration that caused CMT bundling.

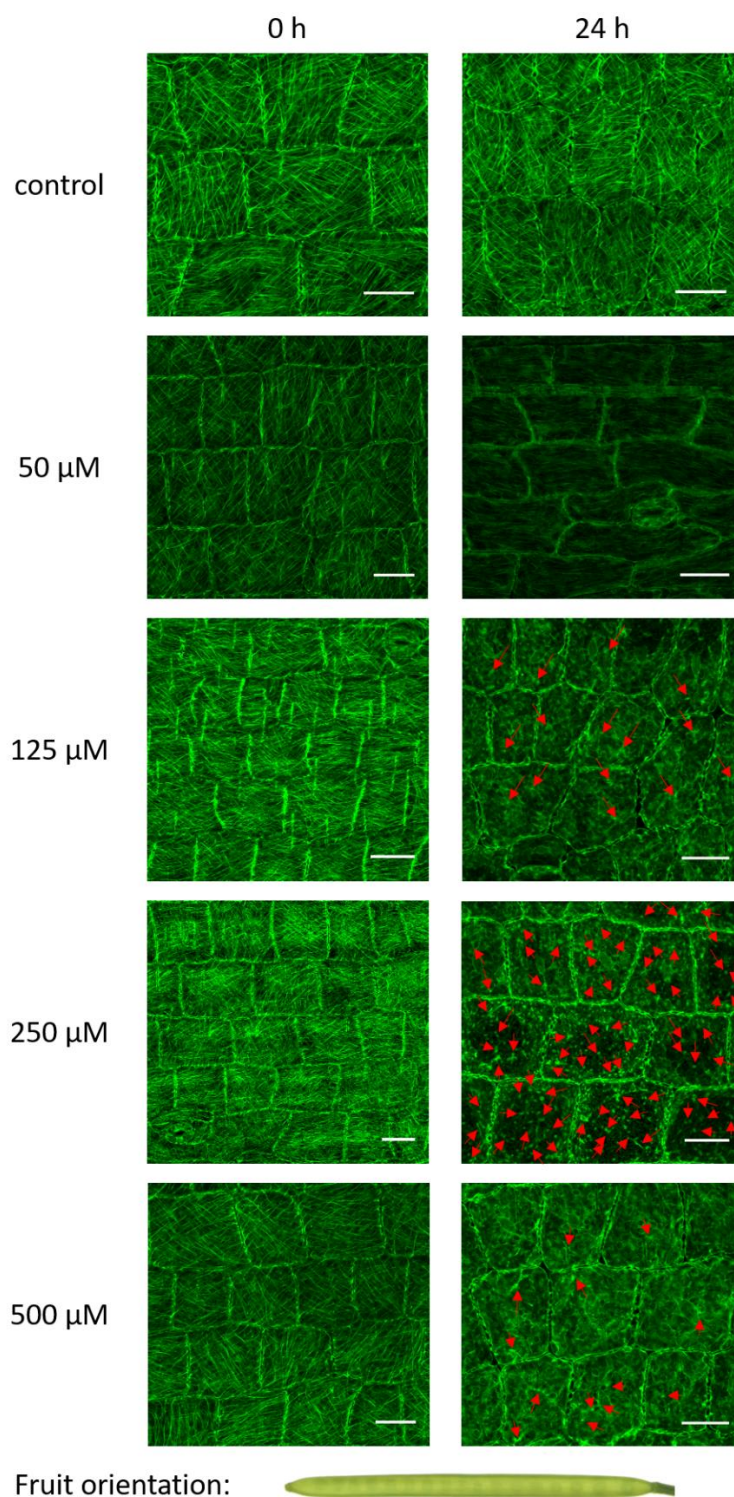


Figure 13: Ascertaining a suitable oryzalin concentration for CMT disruption in adult fruit pods. Branches of individual *C. hirsuta* 35S::GFP:TUA6 plants were dipped in solutions of 50 μ M, 125 μ M, 250 μ M and 500 μ M oryzalin for 5 min, respectively. Afterwards, the CMT alignment of random pods of the treated branches were analysed via CLSM. The arrows indicate bundled CMT. Scale bars: 25 μ m.

In the next step, I analysed the effect of a single oryzalin treatment on CMT alignment in the exocarp during fruit development. I used *C. hirsuta* 35S::GFP:TUA6 plants and pods of stage 16. I performed CLSM on untreated, oryzalin treated (125 μ M), and DMSO treated fruit pots (n=1 for each treatment) at 0 h. Then, I performed CLSM again to analyse CMT alignment 24 h, 48 h, 72 h and 144 h post treatment. Finally, I calculated CMT angles in relation to the longitudinal fruit axis to quantify CMT alignment (Figure 14). The results show that fruits treated with control solution exhibit CMT alignments and dynamics comparable to untreated wild-type fruit pods (Figure 9, Figure 12 and Figure 14). At 0h and 24 h, CMT angles are skewed to high values, indicating a transverse alignment, and after 48 h, CMT angles are skewed to low values, indicating a longitudinal alignment, which is maintained through to 144 h (Figure 14). Additionally, exocarp cell shape changed from almost square, to rectangular, to square again, as I observed previously (Figure 9). Analysis of two individual fruit pods treated with 125 μ M Oryzalin for 5 min, did not show the CMT bundling that I had observed previously (compare Figure 14 with Figure 13). However, the oryzalin treatment affected CMT alignment in oryzalin replicate 1, reducing the magnitude of aligned CMTs in all cells after 24 h (see red lines reduced to dots in Figure 14). This was sustained for 48 h and then cells recovered CMT alignment after 72 h (see red lines in Figure 14). Interestingly, the distribution of CMT angles at 72 h and 144 h was skewed towards low values in oryzalin-treated fruit, indicating a longitudinal alignment, which was very similar to control samples (Figure 14). These results suggest that when CMTs recovered after oryzalin treatment they did not recover their pre-treatment transverse alignment, but rather the longitudinal alignment that their developmental age dictates.

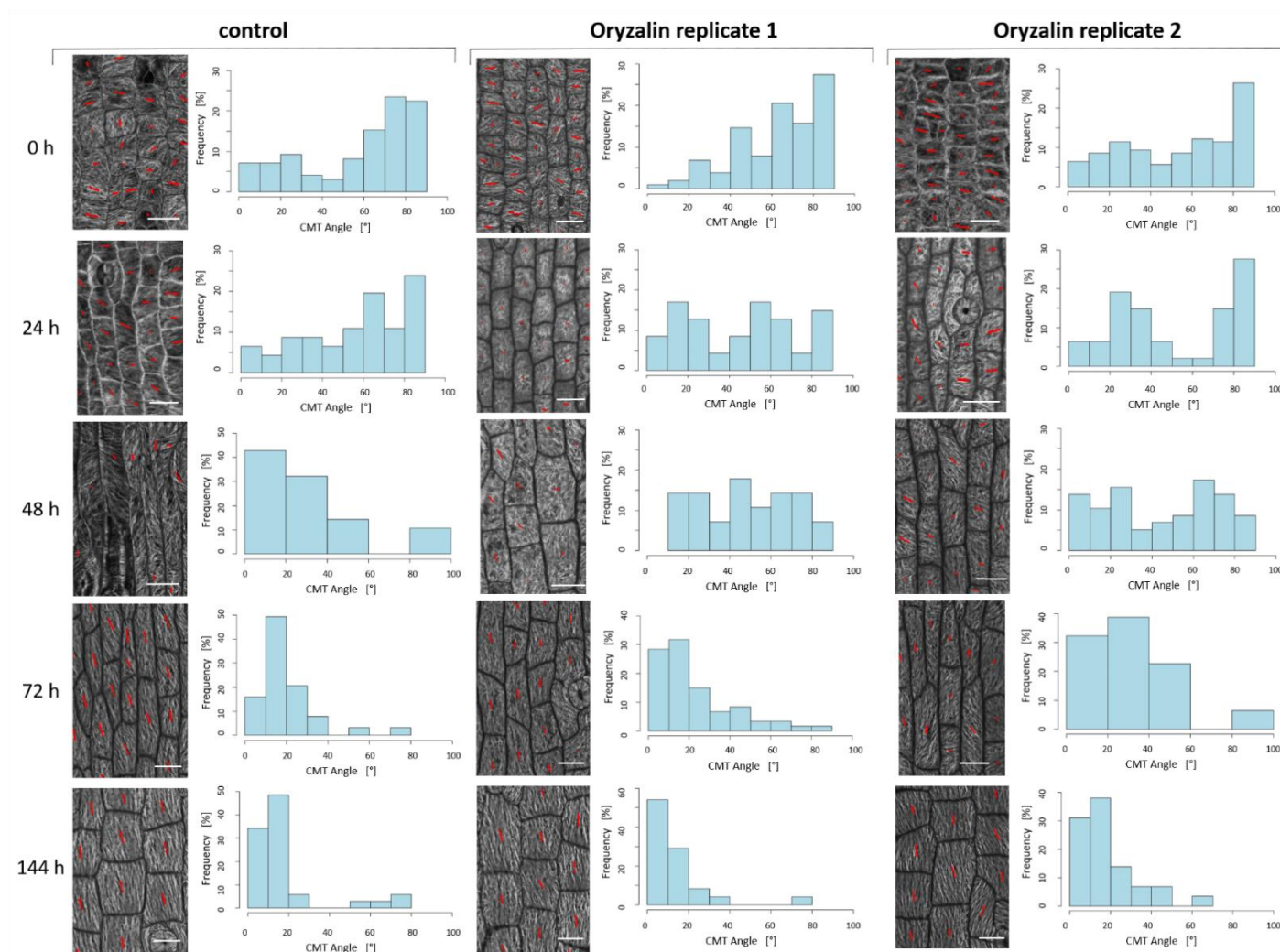


Figure 14: Single oryzalin treatment of *C. hirsuta* 35S::*GFP:TUA6* fruit pods (stage 16). Individual pods were dipped in 125 μ M oryzalin (rep1, rep2) and 125 μ M DMSO (control) for 5 min. The length of the red line represents the extent of CMT organisation and its orientation represents the average CMT alignment of the cell. Frequency histograms plot the frequency of cells with average CMT angles in bins of 10° from 0 – 90°. Scale bars: 25 μ m.

Based on these results I decided to modify my experimental design from a single, short oryzalin treatment to a sustained treatment. Two factors that I wanted to address were: (1) the lack of CMT bundling, suggesting that CMTs were not fully depolymerized, and (2) the recovery of longitudinal CMT alignment. By treating *C. hirsuta* 35S::*GFP:TUA6* fruit pods daily with 125 μ M oryzalin, I aimed to achieve a sustained depolymerization of CMTs in the exocarp. Further, I strictly focused on fruits of 7 mm length since this length indicated the very start of stage 16 when CMT alignment is transverse (Table 3). I began by marking single fruit pods of 7 mm length in a sample of 40 plants. Then I performed CLSM on 7 mm fruit pods from 6 plants to analyse CMT alignment before oryzalin treatment (0 h) (Figure 15). CLSM was strictly performed on living fruits that were still attached to the plant. I divided the remaining 34 plants, carrying a marked 7 mm long fruit pod, equally into samples and controls. I treated sample fruit pods with 125 μ M oryzalin for 10 min and treated control fruit pods similarly with DMSO. Sample plants were fully separated from control plants to prevent contamination. 24 h after oryzalin treatment, I analyzed CMT alignment in the exocarp of 6 fruit pods by CLSM, and dipped the plants again in freshly prepared oryzalin and control solutions for 10 min, respectively. I repeated the treatments every 24 h until the fruit pods were competent to explode. The sample pods were judged to be competent when the pod that initiated two pods before the sample exploded. At this time point I stopped the treatments and performed a final CLSM analysis. In this experiment, I stopped after 16 days (384 h).

To investigate the effect of continuous oryzalin treatments, I quantified CMT angles in relation to longitudinal fruit axis and plotted them against their frequency (Figure 15). To summarize my results I pooled the data of the three control fruits to plot as a histogram at each time point and showed the magnitude of CMT alignment per cell in a representative fruit. The control fruits followed a similar developmental

trajectory to what I have previously described (Figures 9, 12, 14). At 0 h, the distribution of CMT angles is skewed towards high angles and the magnitude of alignment is high, indicating a well-organized, transverse CMT alignment (Figure 15). This transverse alignment is sustained after 24 h and reorients towards a longitudinal alignment after 48 h (Figure 15). At 72 h, the distribution of CMT angles is skewed towards low angles and the magnitude of alignment is high, indicating a well-organized, longitudinal CMT alignment (Figure 15). Then at 384 h, when the control fruits are competent to explode, CMT angles remained low with a distribution centered around 20° (Figure 15). At this time point, exocarp cell shape in the control fruit had changed from rectangular to square (Figure 15).

In comparison to these control fruit, CMT alignment in the exocarp was severely disrupted by sustained oryzalin treatment (Figure 15). At 0 h, sample fruit had a very similar transverse alignment of exocarp CMTs to control fruit (Figure 15). However, CMT alignment is completely abolished 24 h after oryzalin treatment although the CMT bundling that I saw in previous oryzalin treatments was not visible (Figure 15 and Figure 13). This disruption is even stronger after 48 h, 72 h and 384 h, such that the red lines that show the magnitude of CMT alignment per cell are reduced to dots, indicating no ordered CMT alignment (Figure 15). Therefore, it made no sense to calculate CMT angles in any of these oryzalin-treated samples. 384 h after oryzalin treatment I saw CMT bundling comparable to Figure 13. However, the strong depolymerizing effect was visible in all oryzalin replicates.

Oryzalin treatment affected not only CMT alignment but also the dynamic cell shape changes that *C. hirsuta* exocarp cells pass through (Figure 9, Figure 11 and Figure 15). In control samples, exocarp cell shape changes from square to rectangular and elongate at 48 h – 72 h, before changing again by expanding in width to become square at 384 h (Figure 15). At 48 h – 72 h after oryzalin treatment, exocarp cells appear

slightly rounded and less elongated than the exocarp cells of control fruit (Figure 15). By 384 h after oryzalin treatment, exocarp cell shape is abnormal with aberrant bulges and not comparable to the cell shape of control fruit at this time point (Figure 15). Therefore, oryzalin treatment disrupted the changes in exocarp cell shape that are part of normal fruit development in *C. hirsuta* and are predicted to play a key role in the contraction mechanism that generates the tension required for explosive pod shatter (Hofhuis *et al.*, 2016).

To further analyse the effect of oryzalin treatment on exocarp cell shape, I calculated the aspect ratio of treated and untreated cells throughout the time course experiment (Figure 16). At 0 h, exocarp cells in the control fruit exhibited a square shape with a mean aspect ratio of approximately one (Figure 16). Over the following 72 h, the mean aspect ratio mean increases over one indicating an elongate, rectangular shape (Figure 16). By 384 h, exocarp cells acquire a square shape represented by a mean aspect ratio of approximately one (Figure 16). This is consistent with previous findings (Figure 11). Exocarp cell shape in oryzalin-treated fruit differed significantly from control fruit at 48 h (Figure 16). The mean aspect ratio of oryzalin-treated cells at 48 h was lower than untreated cells, indicating a more square shape, similar to the shape of cells at 0 h before treatment (Figure 16). Therefore, oryzalin treatment blocked the dynamic changes in exocarp cell shape that are specific to the development of explosive *C. hirsuta* fruit and not found in the non-explosive fruit of *A. thaliana* (Figure 11).

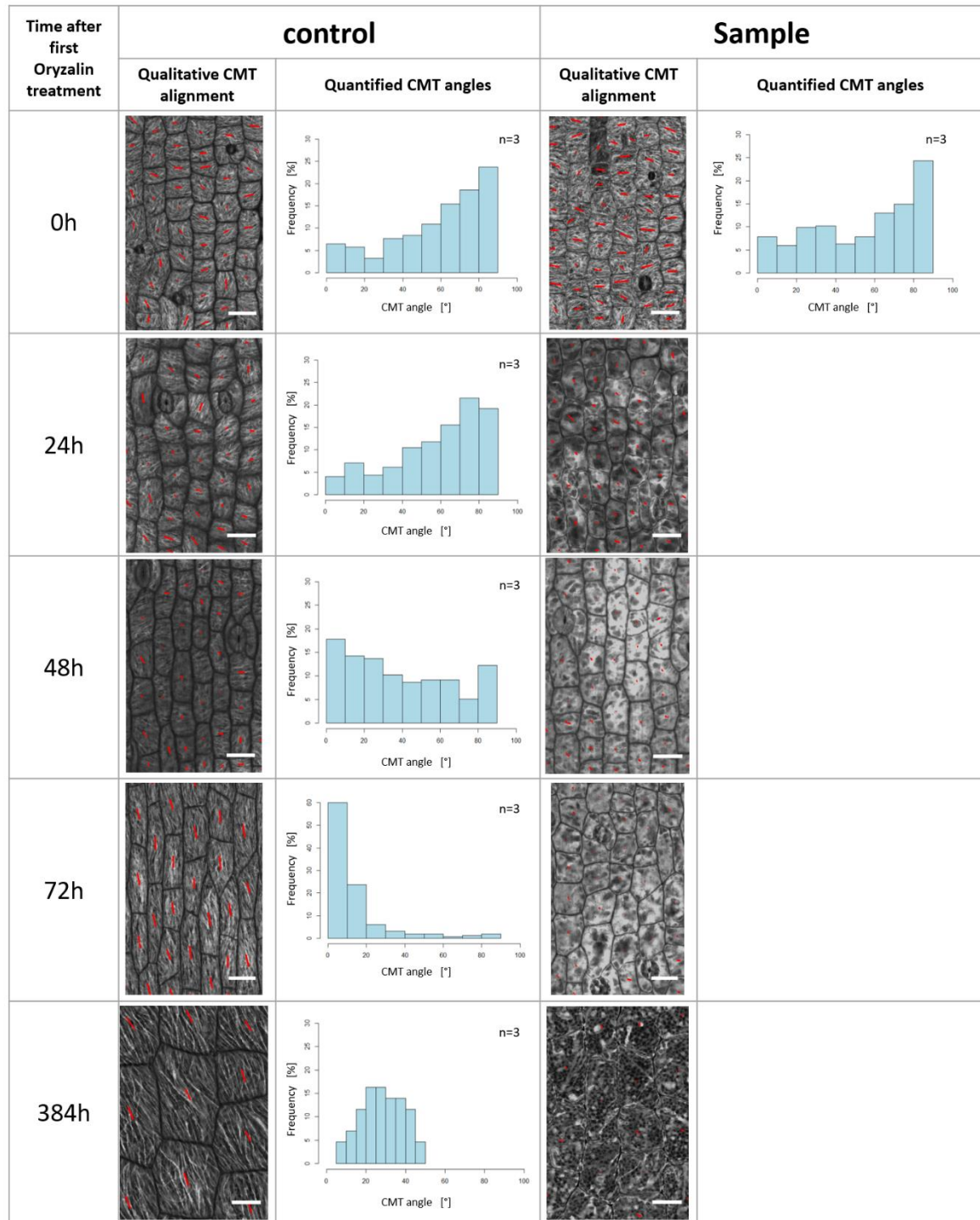


Figure 15: Sustained oryzalin treatment of *C. hirsuta* 35S::*GFP:TUA6* fruit pods. Every 24 h until the pod were close to explosive pod shatter, the fruits were treated with 125 μ M oryzalin and 125 μ M DMSO, respectively. The data of three treated plants were pooled, each. Due to the depolymerized CMT, the oryzalin treated fruits lost the CMT alignment. The magnitude (red line) represents the average CMT orientation of the cells and its length indicates the degree of CMT organisation. Scale bars: 20 μ m.

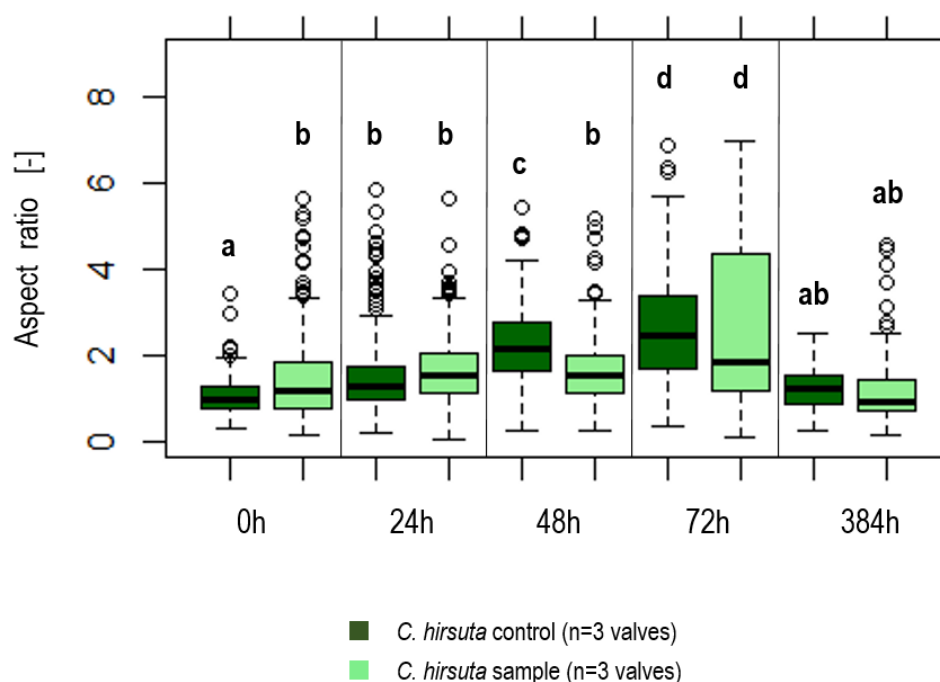


Figure 16: Aspect ratio analysis of *C. hirsuta* 35S::GFP:TUA6 valve exocarp cells treated with 125 μ M oryzalin (sample) and 125 μ M DMSO (control), respectively. Box and whisker plots: box delimits the 2nd and 3rd quartiles, whiskers show the 1st and 4th quartiles, white circles show outliers, black lines show mean. Statistical significance was determined at 0.05 by an ANOVA Tukey test.

Table 4: Effect of sustained oryzalin treatment on explosive pod shatter. The numbers are mean values of the analysed segmented cells.

		Change in length		Change in width		Change in depth		Change in volume
		μ m	%	μ m	%	μ m	%	%
Control	H ₂ O	18.52	- 0.79	26.68	+ 5.04	12.32	+ 34.51	+ 75.80
	NaCl	18.67		25.33		8.07		
Sample	H ₂ O	17.75	+ 0.63	22.81	+ 4.17	11.74	+ 6.70	+ 15.68
	NaCl	17.64		21.86		10.95		

To test whether sustained oryzalin treatment during fruit maturation was sufficient to affect explosive pod shatter, I performed another time-course experiment. Fruit pods of *C. hirsuta* 35S::*GFP:TUA6* plants were treated every 24 h with freshly prepared oryzalin and control solutions for 10 min, as previously described. I started the experiment when fruit pods were 7 mm in length, representing the start of stage 16 when CMT alignment is transverse, and continued 24 h treatments until the fruit pods were competent to explode (408 h after first Oryzalin treatment). 24 h after the last treatment, I carefully cut the marked fruit from the plant for analysis (Figure 17). First, I took a picture of the fruit before explosion. Then, I triggered explosion by pressing the base of the fruit with forceps and photographed the freshly exploded fruit valves in air. Sustained oryzalin treatment dramatically abolished explosive pod shatter (Figure 17). The oryzalin-treated fruits appeared very similar in size and morphology to untreated fruits, yet the valves failed to coil explosively (Figure 17). In fact, valves either failed to curve or curved slightly but failed to produce a single coil (Figure 17). Therefore, I was unable to quantify coil diameter in these samples (Figure 18).

To further investigate the effect of oryzalin treatment on valve coiling, which is a process that requires turgor pressure (Hofhuis *et al.*, 2016), I placed the fruit valves in water for 45 min, photographed them, then placed the valves in a 4 M NaCl solution for 45 min before photographing them again. This osmotic treatment affected valve coiling of control fruit as previously reported (Hofhuis *et al.*, 2016): the valves curled into 3-4 coils in air, coiled more tightly in water, and more loosely in 4 M NaCl (Figure 17). To quantify these effects, I calculated the diameter of the valve coils in each treatment by fitting a circle inside the coil from top view images (Figure 17, Figure 18). I found no significant difference between the coil diameters of untreated wild-type and control fruits (Figure 18). In contrast to this, the valves of oryzalin-treated fruits were insensitive to osmotic treatment (Figure 17), suggesting that the mechanism of turgor-

driven contraction, which is required for valve coiling, had been abolished in the exocarp cell layer (Hofhuis *et al.*, 2016).

To further investigate the dramatic effect of sustained oryzalin treatment on explosive pod shatter, I used CLSM to compare the exocarp cellular response to osmotic treatments in oryzalin-treated versus untreated fruit. At the organ level, I had shown that valves of oryzalin-treated fruits were insensitive to osmotic treatment (Figure 17). Now, I aimed to test whether I could observe this effect at the cellular level. Previous work had shown that exocarp cells in wild-type fruit contracted in length by 12% when transferred from low turgor (1 M NaCl) to high turgor (pure water) solutions, despite expanding in volume by 53% (Hofhuis *et al.*, 2016). This anisotropic response of exocarp cells to turgor pressure was proposed to play a key role in the tissue contraction that drives explosive pod shatter (Hofhuis *et al.*, 2016). Therefore, I aimed to repeat these experiments using fruit that had been treated with either 125 μ M oryzalin or control solution every 24 h for a total of 384 h, as described previously (Figure 15).

The method I followed was to cut 2-4 mm long fruit segments and perform CLSM in both high turgor and low turgor solutions after cell wall staining with propidium iodide (PI). Specifically, I placed the fruit segments in deionized water with PI for 10 min and then imaged exocarp cells under this high turgor treatment. Next, I placed the fruit segments in 1 M NaCl with PI for 45 min. I exchanged the solution with water before imaging the same exocarp cells under this low turgor treatment. I loaded the CLSM stacks into MorphoGraphX software to generate a 3D mesh of the exocarp cells in high and low turgor treatments. I used these 3D meshes to measure the changes in cell volume and directional expansion and shrinkage in these cells in response to osmotic treatments. I summarize the results of four adjacent exocarp cells in oryzalin-treated and untreated *C. hirsuta* fruit at time point 384 h (Figure 19 and Figure 20). I used

crosshairs in a top view of the cells in high turgor, to display the principal directions of shrinkage (red) and expansion (white) when compared to low turgor. The exocarp cells of control fruits shrink slightly in length and expand in width under high turgor (Figure 19 A, Table 4). These cells also expand considerably in depth under high turgor, as seen in side view (Figure 19 B, C Table 4). The increase in cell volume under high turgor is also obvious from this side view (Figure 19 B, C Table 4). Exocarp cell volume increased by 75.80 % under high turgor and this change between high and low turgor is displayed as a heatmap in a top view of the cells in high turgor (Figure 19 D). This overall trend of increasing cell volume, depth and width and decreasing cell length in response to increasing turgor, is similar to previous results (Hofhuis *et al.*, 2016), but the magnitude of change in cell length is much reduced because I used whole fruit rather than valve segments in my experiment (discussed further in discussion section).

In contrast to control fruit, the exocarp cells in oryzalin-treated fruit showed very little change in response to osmotic treatments (Figure 20, Table 4). In particular, cells showed no appreciable expansion in volume under high turgor, and no expansion in width or depth (Figure 20, Table 4). The lack of response to osmotic treatments in exocarp cells of oryzalin-treated fruits may indicate a technical problem. For example, the cells may have been damaged during the experiment such that they failed to inflate and deflate in response to osmotic treatments. Therefore, it is difficult to draw conclusions from this experiment (discussed further in discussion section).

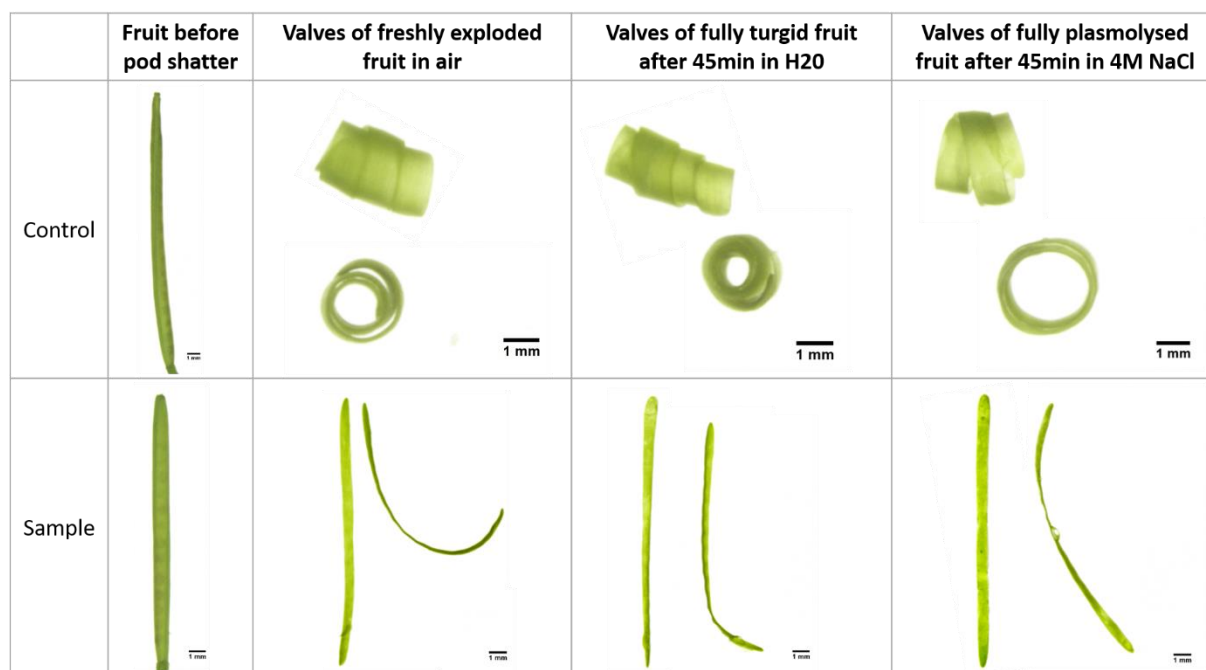


Figure 17: Sustained oryzalin treatment of *C. hirsuta* 35S::GFP:TUA6 fruits abolishes explosive valve coiling. Fruit pods were manually triggered to explode at time point 408 h and valves were photographed in air and after high turgor (pure water) and low turgor (4 M NaCl) treatments.

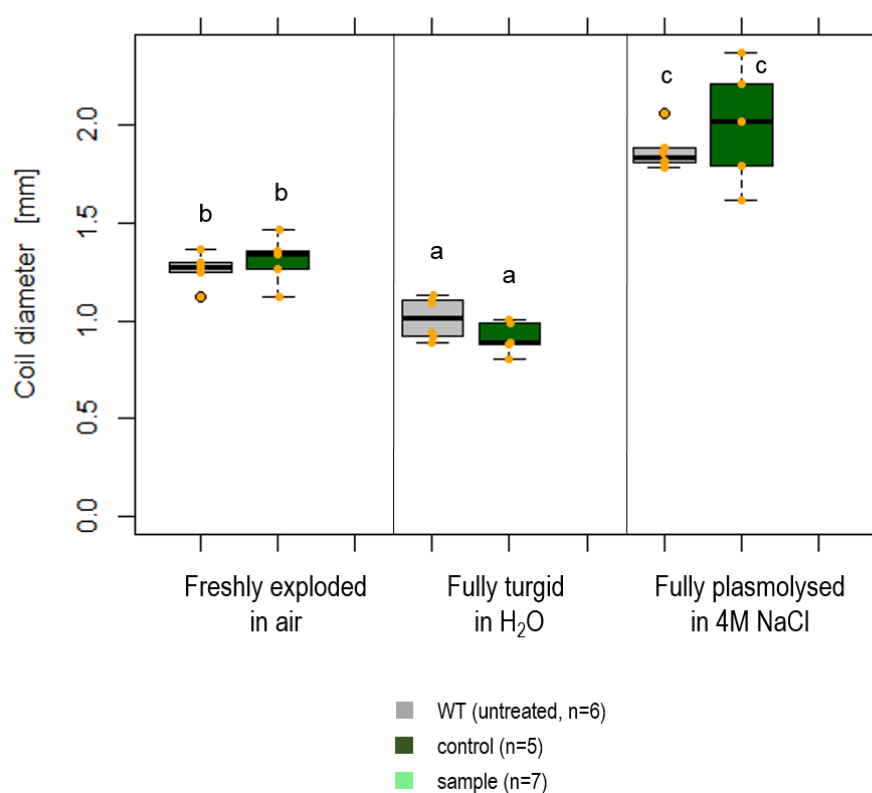


Figure 18: Quantification of coil diameters of osmotic treated *C. hirsuta* 35S::GFP:TUA6 fruits after a continuous chemical treatment (125 μ M DMSO and 125 μ M oryzalin, respectively) in a 24 h rhythm.

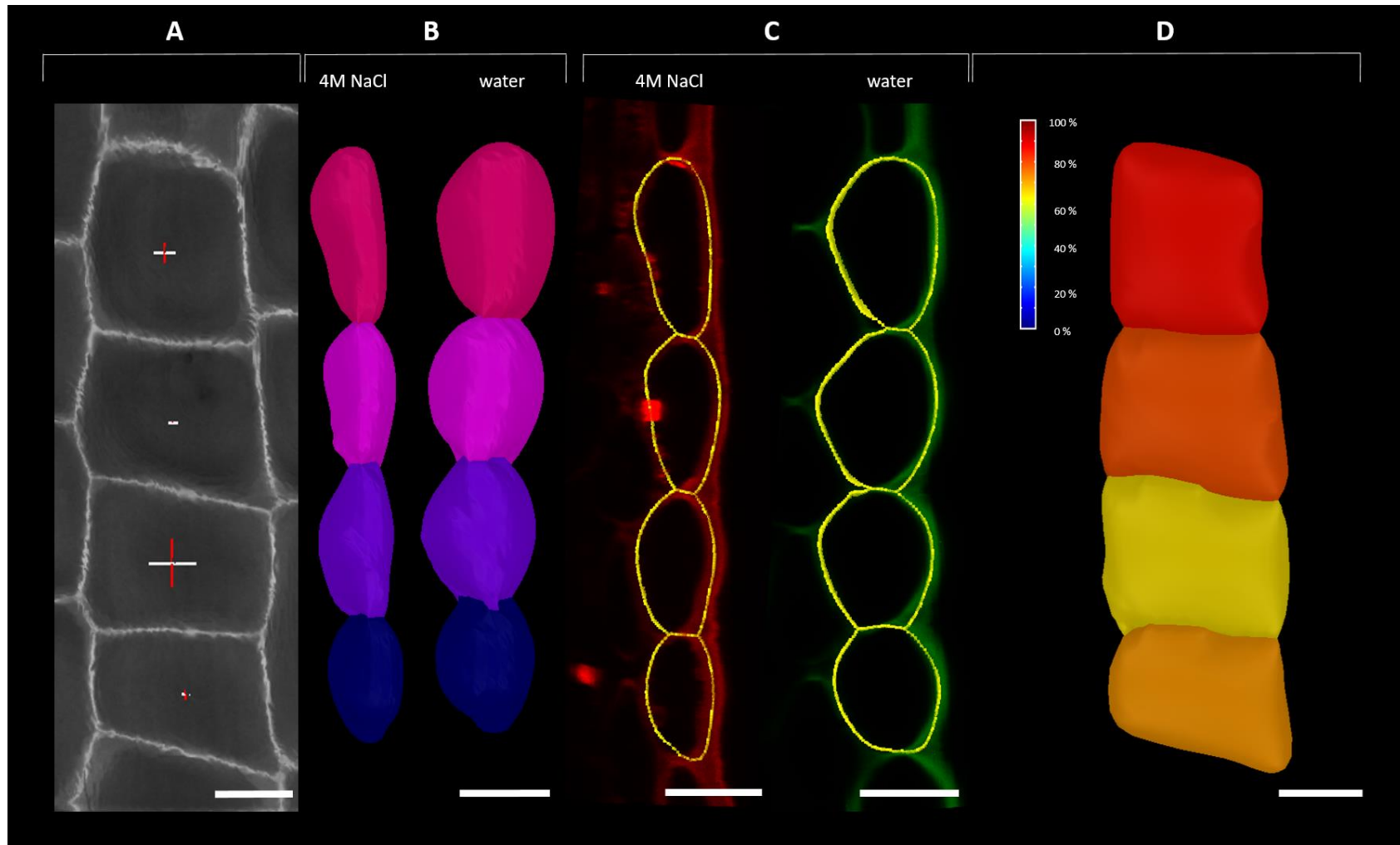


Figure 19: Osmotic treatment of *C. hirsuta* 35S::GFP:TUA6 fruits before explosive pod shatter. The fruit analysed fruit pods were repeatedly dipped in 125 μ M DMSO. A) Top view of PI-stained cells before osmotic treatment. The crosshairs show the principal directions of shrinkage (red) and expansion (white) in comparison to salt treated cells. B) The segmented exocarp cells post and prior salt treatment. C) Side view of PI-stained cells post and prior salt treatment. D) Segmented exocarp cells post and prior salt treatment. The heat map shows cell volume. Scale bars: 20 μ m.

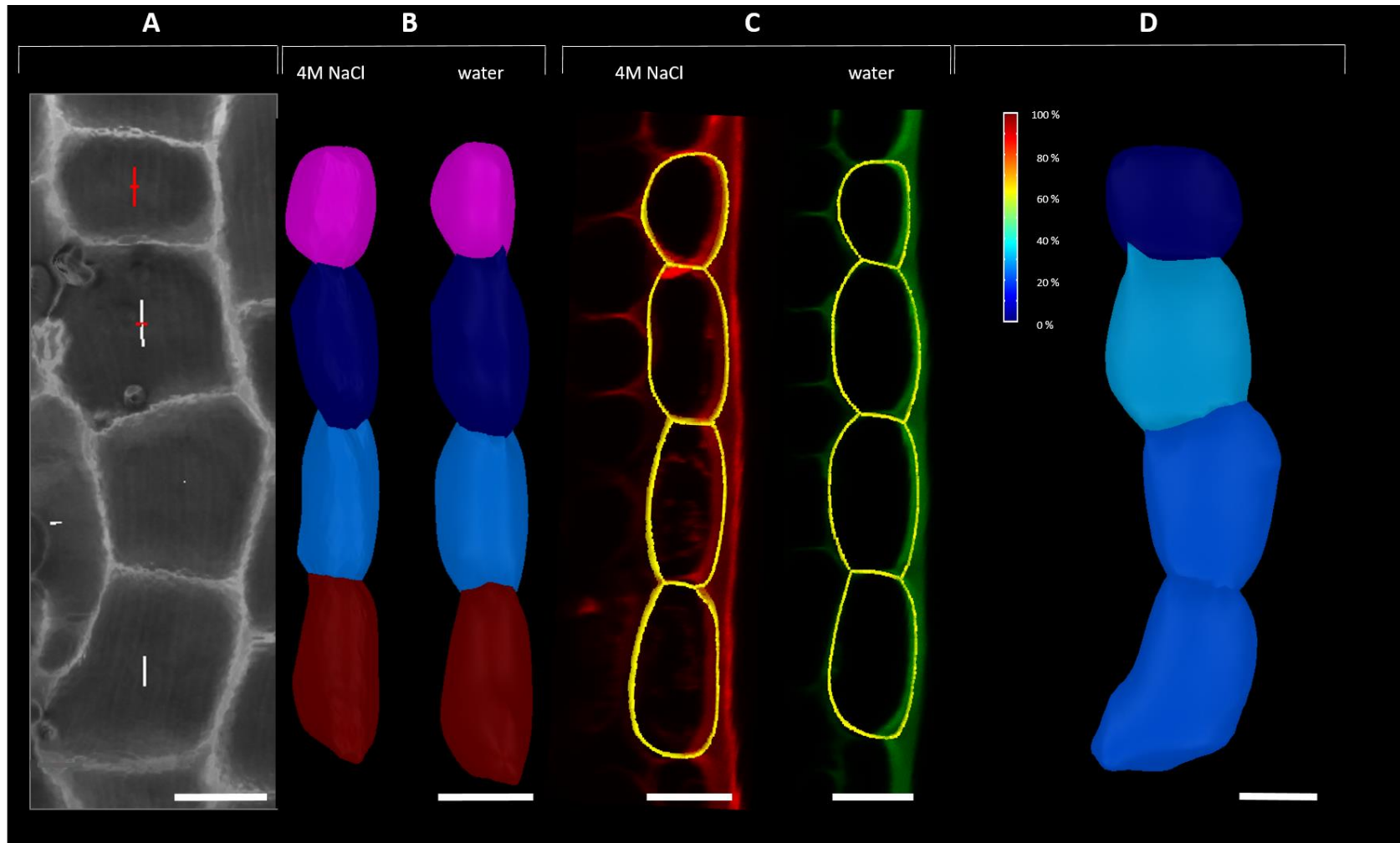


Figure 20: Osmotic treatment of *C. hirsuta* 35S::GFP:TUA6 fruits before explosive pod shatter. The fruit analysed fruit pods were repeatedly dipped in 125 μM oryzalin. A) Top view of PI-stained cells before osmotic treatment. The crosshairs show the principal directions of shrinkage (red) and expansion (white) in comparison to salt treated cells. B) The segmented exocarp cells post and prior salt treatment. C) Side view of PI-stained cells post and prior salt treatment. D) Segmented exocarp cells post and prior salt treatment. The heat map shows cell volume. Scale bars: 20 μm .

3.4. KATANIN1 (*KTN1*) Silencing During Fruit Development

In the previous section I showed that sustained oryzalin treatment abolished explosive pod shatter in *C. hirsuta*. The depolymerization of CMTs during fruit maturation (treating fruit from stage 16 until competent to explode) affected valve coiling without affecting overall fruit size and morphology (Figure 17). To extend these findings, I aimed to create a genetic tool in *C. hirsuta* to perturb CMT alignment and dynamics. Since *KTN1* is required for CMT organisation and reorientation in *A. thaliana* (McNally and Vale, 1993; Vaughn and Lehen, 1991; Zhang *et al.*, 2013), I investigated whether loss of *KTN1* gene function in *C. hirsuta* affected exocarp cell CMT. To silence *KTN1* gene expression, I used an artificial mircoRNA designed to a region of *A. thaliana KTN1* (amiRKTN1, kindly provided by A. Maizel) with 62% identity to *C. hirsuta KTN1* (CARHR074160.1) (Figure 21). I inserted the amiRKTN1 into a dexamethasone-inducible two-component system and transformed this construct into *C. hirsuta* and *A. thaliana* wild-type and *35S::GFP:TUA6* plants (Figure 22). The design of this construct should allow me to broadly induce *KTN1* silencing, under control of the *AtRPS5a* promoter, at specific stages of fruit development, by exposing the fruit to dexamethasone (Dex).

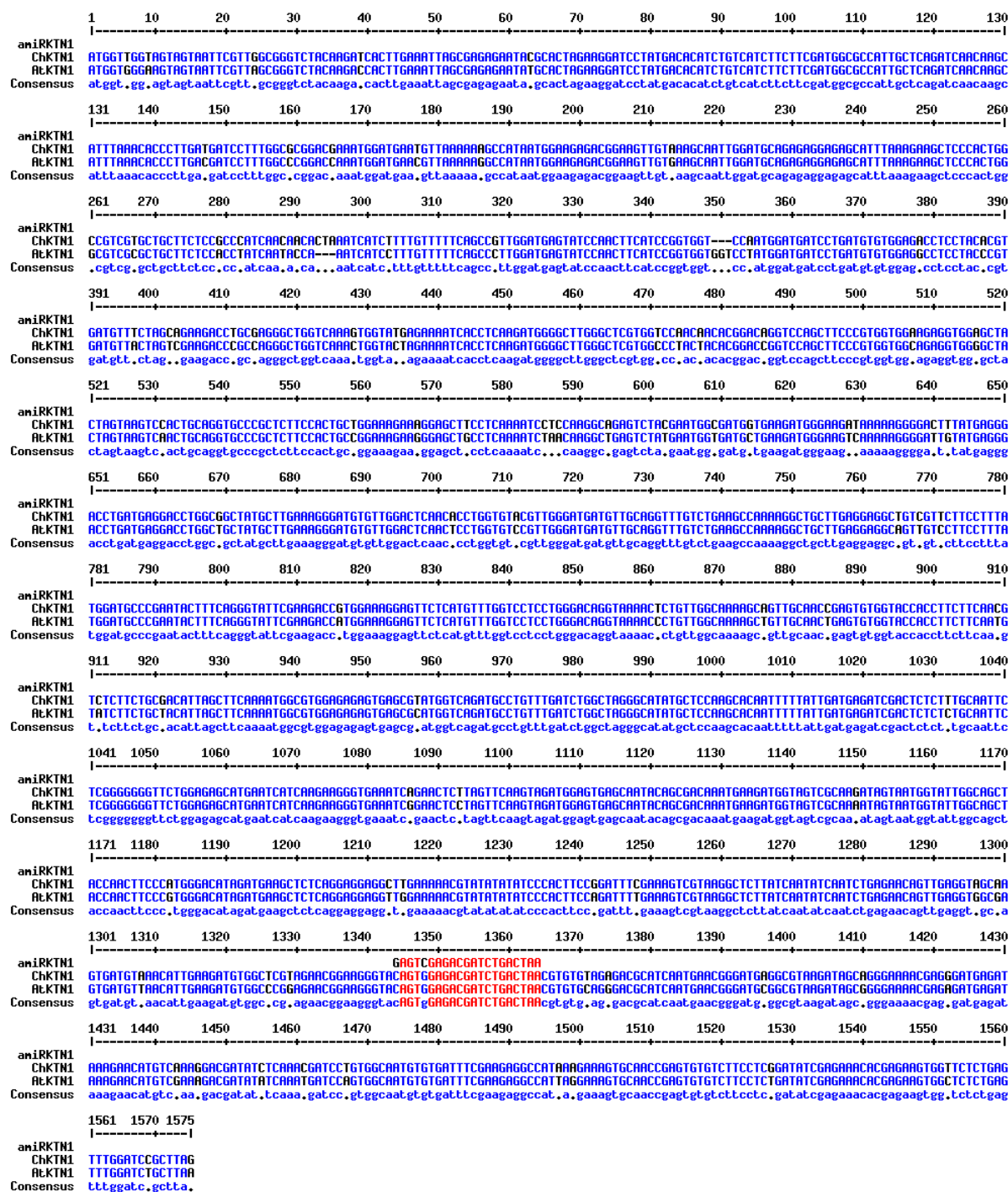


Figure 21: Alignment of amiRKTN1 with *C. hirsuta* KTN1 (CARHR074160.1) and *A. thaliana* KTN1 (AT1G80350.1). The *KTN1* sequence targeted by amiRKTN1 is identical between *A. thaliana* and *C. hirsuta*. There are two mismatches between the amiRKTN1 and *KTN1* sequence.

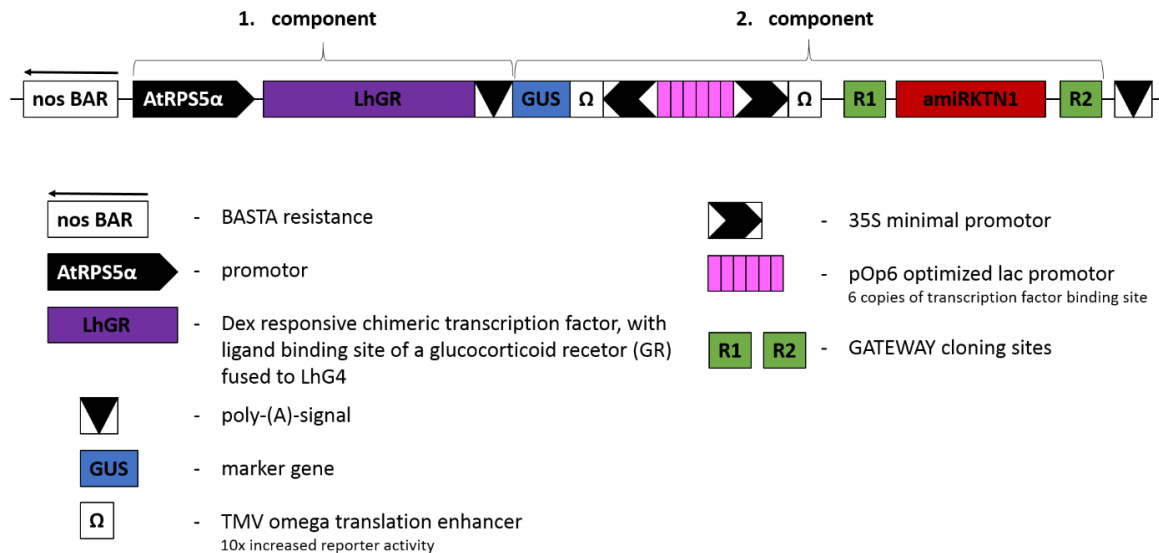


Figure 22: Dexamethasone inducible two-component system carrying amiRKTN1 for posttranslational KTN1 silencing.

I selected *C. hirsuta* and *A. thaliana* 35S::GFP:TUA6; amiRKTN1 lines with a single transgene insertion locus (by scoring segregation of the resistance gene in the T2 generation) and with a wild-type phenotype (indicating that the LhGR system was not leaky). To test whether the Dex induction worked, I analyzed 10 day-old seedlings grown for 48 h on 100 μ M Dex-containing agar and Dex-free agar, respectively. I assayed expression of the GUS marker gene (Figure 22) and found GUS staining was specific to those seedlings grown on Dex-containing agar (Figure 23).

To test whether 100 μ M Dex was sufficient to reduce *KTN1* gene expression levels, I performed RT-qPCR on seedlings grown 48 h on 100 μ M Dex-containing agar and Dex-free agar, respectively. By comparing *KTN1* expression levels of Dex-treated seedlings to untreated seedlings, I found a significant reduction in *KTN1* expression in seedlings grown on Dex-containing agar (Figure 24). In *C. hirsuta*, I found six 35S::GFP:TUA6; amiRKTN1 lines in the T2 generation with *KTN1* gene expression in seedlings reduced to approximately 90 % of wild-type levels (T2-1, T2-3, T2-4, T2-5 and T2-8) (Figure 24). Although, *KTN1* expression levels were also reduced in

C. hirsuta lines T2-2, T2-6 and T2-11, the reduction was not significant (Figure 24). The analysis of *A. thaliana* T2 seedlings grown 48 h on 100 μ M Dex containing agar revealed an even stronger *KTN1* reduction (Figure 24). In *A. thaliana*, I found eight *35S::GFP:TUA6; amiRKTN1* lines in the T2 generation with *KTN1* gene expression in seedlings reduced to 95 % or more of wild-type levels (T2-2, T2-3, T2-5, T2-8, T2-9, T2-11, T2-12 and T2-13) (Figure 24). Line T2-10 showed approx. 80 % reduction in *KTN1* expression associated with a large error and line T2-6 showed wild-type levels of *KTN1* expression (Figure 24). I decided to continue my investigations with *C. hirsuta* *35S::GFP:TUA6; amiRKTN1* line T2-8 and *A. thaliana* *35S::GFP:TUA6; amiRKTN1* line T2-5 since these lines showed a significant reduction of *KTN1* expression in seedlings and were homozygous lines (Figure 24).

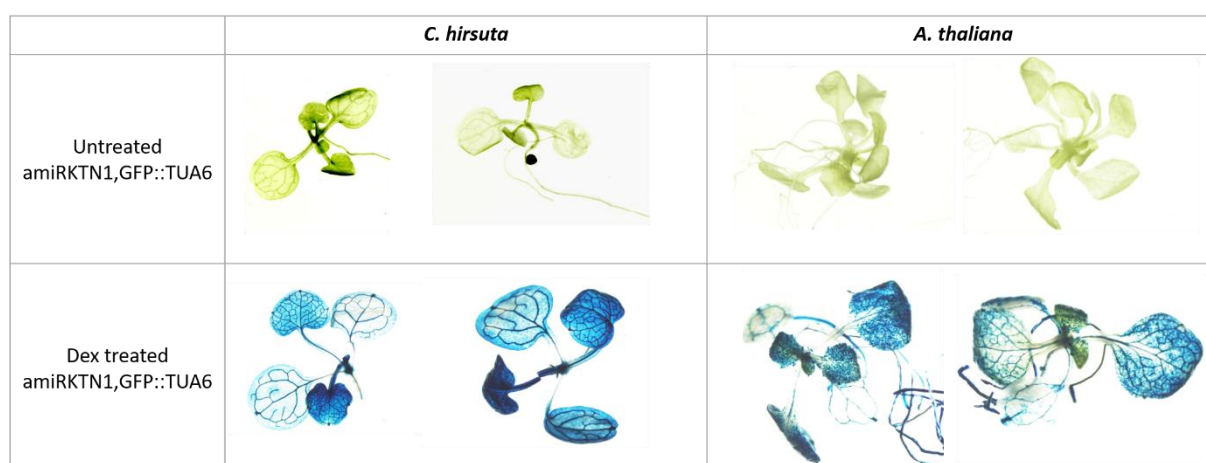


Figure 23: Dex-induction of the GUS marker gene in the *amiRKTN1* two-component construct. *C. hirsuta* and *A. thaliana* *35S::GFP:TUA6; amiRKTN1* lines were grown for 48 h on 100 μ M Dex-containing and Dex-free agar, respectively. The clear blue staining indicates an expression of the GUS marker gene.

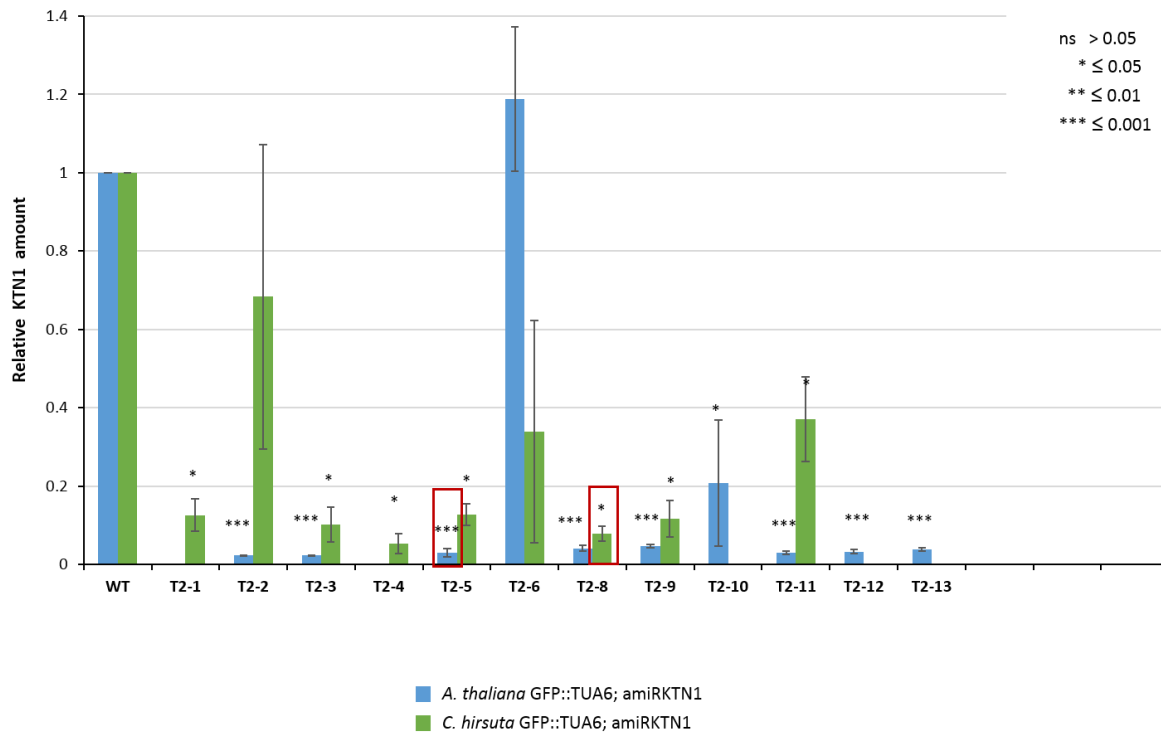


Figure 24: Quantification of *KTN1* gene expression levels by RT-qPCR in seedlings of *C. hirsuta* and *A. thaliana* 35S::GFP:TUA6; *amiRKTN1* lines grown 48 h on 100 μ M Dex-containing agar. The significant reduction in *KTN1* amount in the Dex treated samples indicate a successful expression of the *amiRKTN1* in the two-component construct. The red boxes indicate the homozygous lines I used for further experiments. The diagram shows the means of 3 biological and 3 technical replicates for each analysis. The error bars indicate the error between technical replicates.

To analyze the Dex-induction of *amiRKTN1* in fruit, I treated fruit pods of the homozygous *C. hirsuta* 35S::GFP:TUA6; *amiRKTN1* line T2-8 with 100 μ M Dex. I marked one fruit pod of 7 mm length in 40 individual plants to represent stage 16 of fruit development when CMT reorientation occurs (Figure 12). After performing CLSM to examine CMT alignment in the fruit exocarp before Dex treatment, I separated the remaining plants into controls (n=3) and samples (two replicates with n=3 each). Then, I dipped the branches of the remaining plants carrying the marked fruits into solutions of 100 μ M Dex with 0.03 % Silwet (sample) and water with 0.03 % Silwet (control) for 10 min. I analysed CMT alignment 24 h after treatment by performing CLSM while the fruit was still attached to the plant. Afterwards, I harvested these same fruits for

RT-qPCR analysis to measure *KTN1* gene expression levels. I harvested an additional Dex-treated fruit for GUS staining to qualitatively analyse the effect of the Dex treatment on the construct expression. I repeated these treatments and subsequent analysis every 24 h, such that fruits were treated 0, 1, 2 or 3 times and analyzed 0 h, 24 h, 48 h or 72 h after the first treatment.

To analyze CMT alignment in the valve exocarp cells of sample and control fruit, I quantified the distribution of CMT angles in relation to the longitudinal fruit axis using MorphoGrahpx software (Figure 25). The control fruits showed a reorientation of CMT alignment after stage 16, from transverse to longitudinal, which is comparable to wild type (Figure 9, Figure 12 and Figure 25). At 0 h, the distribution of CMT angles is skewed towards high angles and the magnitude of alignment is high, indicating a well-organized, transverse CMT alignment (Figure 25). At 24 h, the distribution of CMT angles is skewed towards low angles and the magnitude of alignment is high, indicating a switch to a well-organized, longitudinal CMT alignment (Figure 25). This longitudinal CMT alignment is maintained at 48 h and 72 h (Figure 25).

Two samples of Dex-treated fruit showed a delayed acquisition of longitudinal CMT alignment (Figure 25). At 0 h, the distributions of CMT angles are skewed towards high angles and the magnitude of alignments is high, indicating well-organized, transverse CMT alignments (Figure 25). In sample B, this transverse CMT alignment is maintained at 24 h and 48 h time points (Figure 25). Finally at 72 h, the distribution of CMT angles is skewed towards low angles and the magnitude of alignment is high, indicating a switch to a well-organized, longitudinal CMT alignment (Figure 25). Therefore, repeated Dex treatment kept CMT in a transverse alignment for 48 h after reorientation occurred in control fruit. Sample A showed a broad distribution of CMT angles from 0 – 80 ° at 24 h after Dex treatment (Figure 25). At 48 h, the distribution of CMT angles is skewed towards low angles and the magnitude of alignment is high,

indicating a switch to a well-organized, longitudinal CMT alignment, which is maintained at 72 h (Figure 25). Therefore, repeated Dex treatment delayed the rapid reorientation of CMT alignment that occurred in control fruit, such that it occurred after 48 h rather than 24 h (Figure 25).

To verify that these Dex treatments induced expression of the amiRKTN1 two-component construct, I analyzed GUS expression at each time point. Fruit stained distinctly blue 24 h after Dex treatment, indicating strong induction of gene expression (Figure 25). However, after repeated Dex treatments at 48 h and 72 h, the GUS staining becomes faint and accumulates at the tip and base of the fruit, indicating weak induction of gene expression (Figure 25).

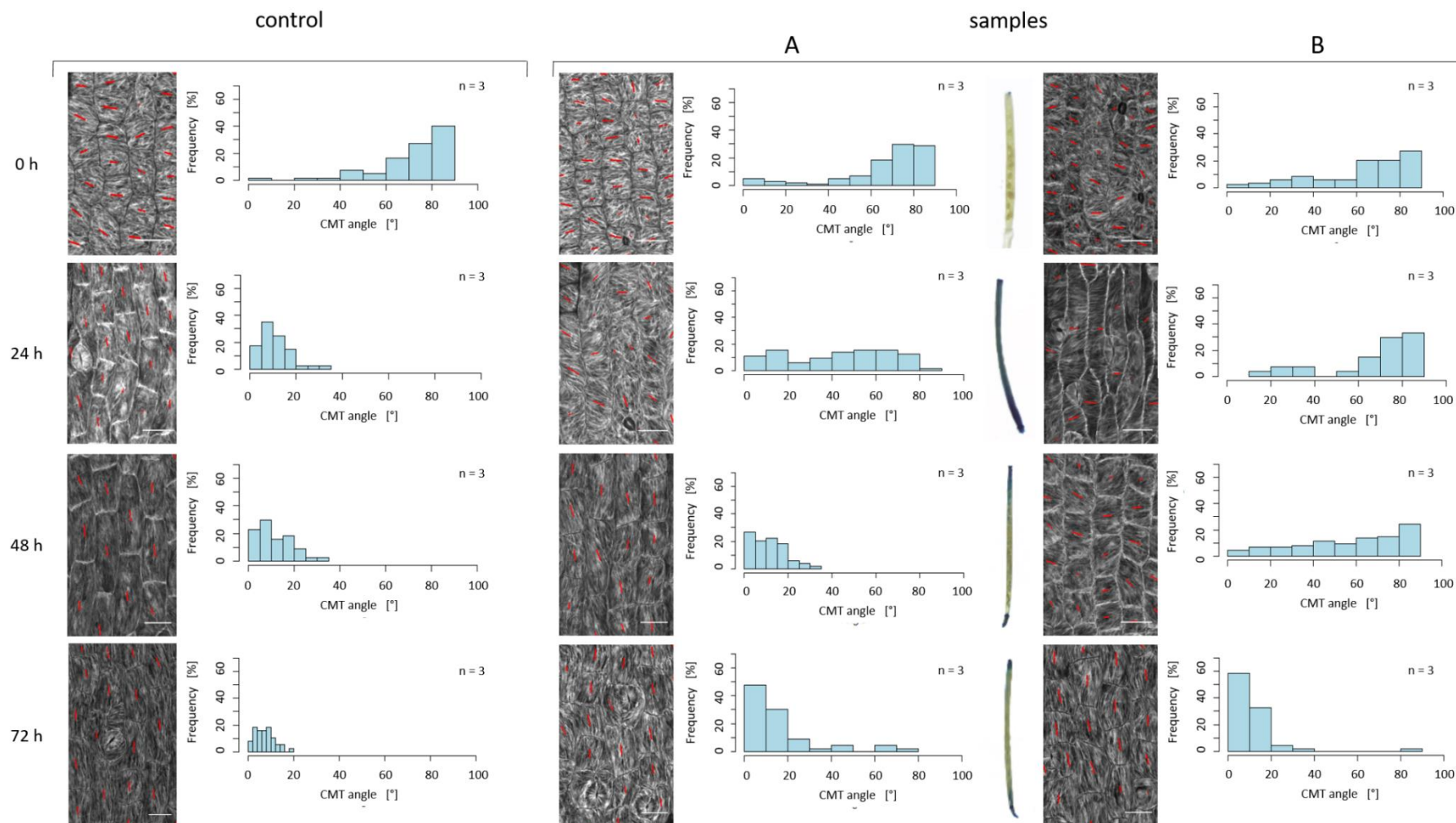


Figure 25: Repeated Dex treatments of *C. hirsuta* 35S::GFP:TUA6; *amiRKTN1* line T2-8 fruit (stage 16). Fruit were treated 0, 1, 2 or 3 times with 100 μ M Dex or water for 10 min and analyzed at 0 h, 24 h (1 x Dex), 48 h (2 x Dex) and 72 h (3 x Dex). The length of the red line represents the extent of CMT organisation and its orientation represents the average CMT alignment of the cell. Frequency histograms plot the frequency of cells with average CMT angles in bins of 10° from 0 – 90°. Scale bars: 25 μ m.

However, when I quantified *KTN1* gene expression in Dex-treated and control fruit by RT-qPCR, I found that sample fruit showed a 55 % reduction in *KTN1* expression compared to control fruit, prior to Dex treatment (Figure 26). Moreover, there was little further reduction in *KTN1* expression 24 h after Dex treatment (Figure 26). At 48 h, after two Dex treatments, *KTN1* expression was reduced to approx. 18 % of control fruit levels, and at 72 h, after three Dex treatments, *KTN1* expression was reduced to approx. 12 % of control fruit levels (Figure 26). The initial difference in *KTN1* expression between sample and control fruit may indicate a technical problem. However, given this result, it is difficult to draw conclusions from this experiment (discussed further in discussion section).

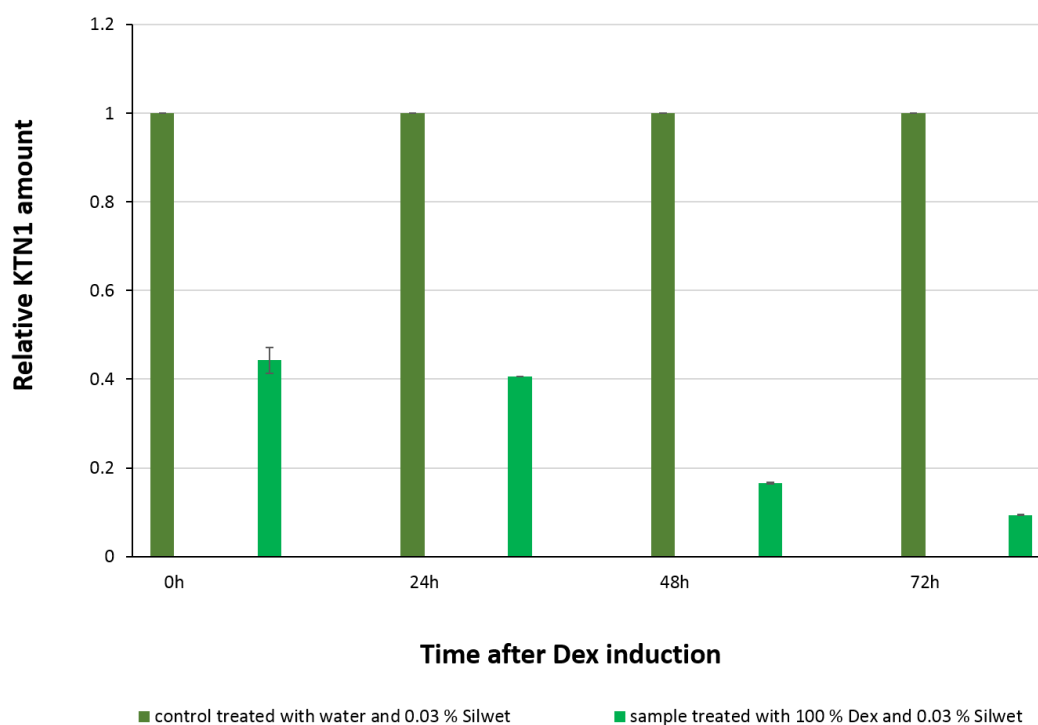


Figure 26: RT-qPCR results of *C. hirsuta* 35S::*GFP:TUA6*; *amiRKTN1* fruit pods repeatedly dipped in a solution of water and 0.03 % Silwet (control) and 100 μ M Dex and 0.03 % Silwet (sample), respectively. The biological replicates are the fruits (n=3) used for CLSM analysis. Error bars indicate variation between technical replicates.

To repeat this experiment, I decided to perform a sustained treatment of *C. hirsuta* and *A. thaliana* 35S::*GFP:TUA6*; *amiRKTN1* fruit with 100 μ M Dex from stage 16 until the fruit pods are competent to explode. After marking one suitable pod per plant and dividing the plants in controls and samples, I performed CLSM time-lapse imaging on 7 mm long fruit pods, still attached to the plant, to examine the CMT alignment before Dex treatment (0 h). After CLSM, I used the imaged fruits for RT-qPCR analysis, and used an additional fruit for GUS staining. The remaining fruit pods were treated with 100 mM Dex and 0.03 % Silwet (sample) or water with 0.03 % Silwet (control) for 10 min, respectively. 24 h after Dex treatment, I used three sample and control fruits for CLSM and RT-qPCR, one sample fruit for GUS staining, and treated the remaining plants again in freshly prepared Dex and control solutions for 10 min, respectively. I repeated the treatments and analysis every 24 h until the fruit pods were competent to explode. I assessed this as previously described in section 3.3, stopping treatments when the fruit pod, which is two fruits before the marked pod, shattered (360 h).

I used RT-qPCR to show that *KTN1* expression levels were initially similar between sample and control fruits and decreased in response to Dex treatment in this experiment (Figure 27). I expressed the amount of *KTN1* mRNA transcripts in Dex-treated fruit relative to untreated fruit (Figure 27). At 24 h after Dex treatment, *KTN1* expression levels reduced by approx. 85 % in *C. hirsuta* and approx. 70 % in *A. thaliana* (Figure 27). *KTN1* expression levels remained low after repeated Dex treatments at 48 h and 72 h time points (Figure 27). At 360 h, after sustained Dex treatments every 24 h, *KTN1* expression levels were approx. 10 % of control levels in *C. hirsuta* and approx. 50 % in *A. thaliana* (Figure 27). Therefore, sustained Dex treatment produced a significant and sustained reduction of *KTN1* gene expression in *C. hirsuta* 35S::*GFP:TUA6*; *amiRKTN1* fruit, and a significant, although more variable,

reduction of *KTN1* gene expression in *A. thaliana* 35S::GFP:TUA6; *amiRKTN1* fruit pods repeatedly dipped in a solution of water and 0.03 % Silwet (control) and 100 μ M Dex and 0.03 % Silwet (sample), respectively. (Figure 27).

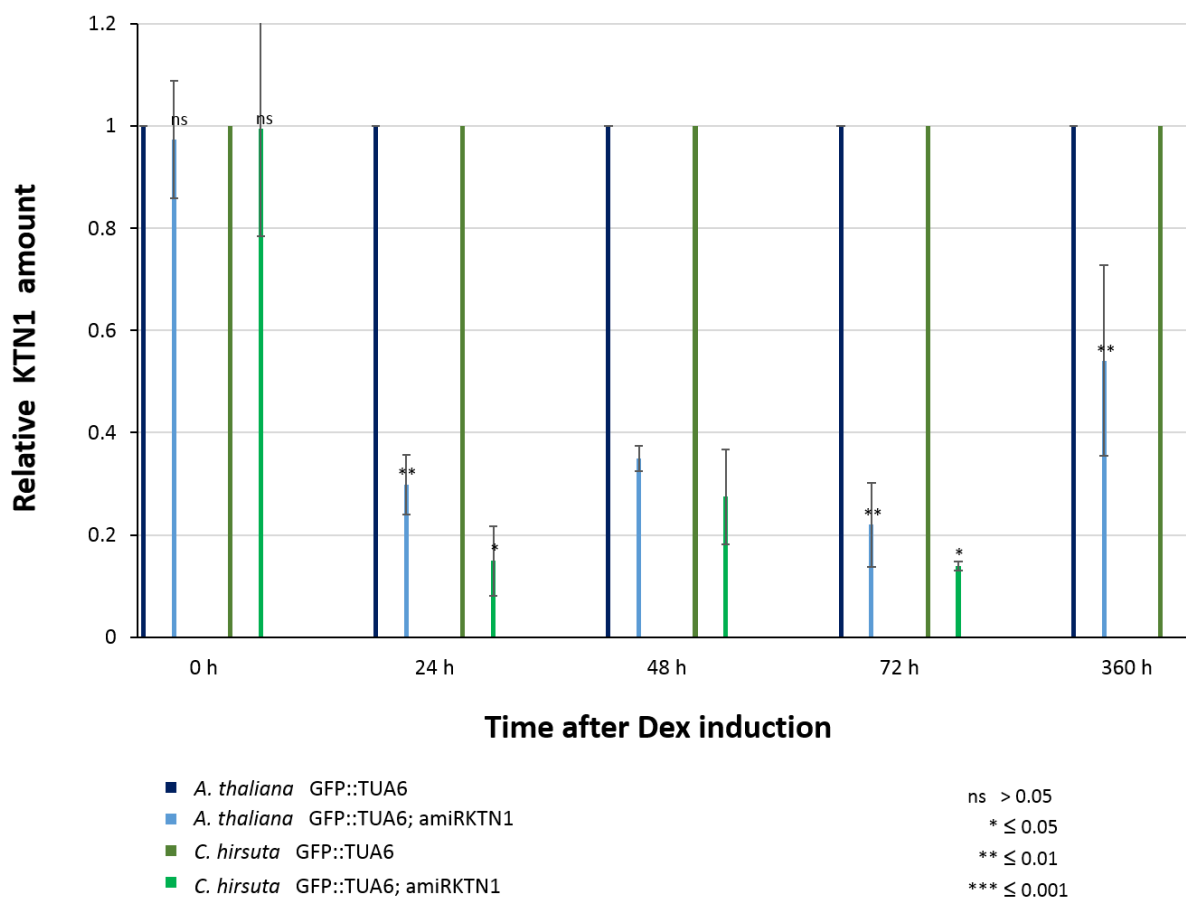


Figure 27: RT-qPCR results of *C. hirsuta* and *A. thaliana* 35S::GFP:TUA6; *amiRKTN1* fruit pods repeatedly dipped in a solution of water and 0.03 % Silwet (control) and 100 μ M Dex and 0.03 % Silwet (sample), respectively.

Next, I investigated the effect of sustained Dex treatment of *35S::GFP:TUA6; amiRKTN1* fruit on CMT organization (Figure 28 and Figure 29). To summarize my results, I pooled data from three fruits to plot the distribution of CMT angles in exocarp cells as a histogram at each time point, and showed the magnitude of CMT alignment per cell in a representative fruit (Figure 28 and Figure 29). In *C. hirsuta*, the control fruits showed a reorientation of CMT alignment after stage 16, from transverse to longitudinal, which is comparable to wild type (Figure 9, Figure 12 and Figure 28). At 0 h, the distribution of CMT angles is skewed towards high angles and the magnitude of alignment is high, indicating a well-organized, transverse CMT alignment (Figure 28). This transverse CMT alignment is maintained at 24 h and changes to a broad distribution of CMT angles from 0 – 90 ° at 48 h after Dex treatment (Figure 28). At 72 h, the distribution of CMT angles is skewed towards low angles and the magnitude of alignment is high, indicating a switch to a well-organized, longitudinal CMT alignment (Figure 28). At 360 h, the distribution of CMT angles shows a peak at 30 ° (Figure 28).

In *C. hirsuta 35S::GFP:TUA6; amiRKTN1* fruit, Dex treatment caused a 24 h delay in switching from transverse to longitudinal CMT alignment (Figure 28). At 0 h, the distribution of CMT angles is skewed towards high angles and the magnitude of alignment is high, indicating a well-organized, transverse CMT alignment (Figure 28). This transverse CMT alignment is maintained at 24 h and 48 h time points (Figure 28). Finally at 72 h, the distribution of CMT angles is skewed towards low angles and the magnitude of alignment is high, indicating a switch to a well-organized, longitudinal CMT alignment (Figure 28). This longitudinal CMT alignment is maintained at 360 h (Figure 28). Therefore, repeated Dex treatment maintained CMT in a transverse alignment for 24 h after CMTs had begun to reorient in control fruit (Figure 28).

Dex-treated fruit also stained blue at every time point when assayed for GUS expression, indicating sustained expression of the *amiRKTN1* construct (Figure 28).

In contrast to *C. hirsuta*, Dex treatment of *A. thaliana* *35S::GFP:TUA6;amiRKTN1* fruit had little effect on CMT organization (Figure 29). In *A. thaliana* *35S::GFP:TUA6; amiRKTN1*, the control fruits showed a reorientation of CMT alignment after stage 16, from transverse to longitudinal, which is comparable to wild type (Figure 9, Figure 29). However, as previously observed (Figure 9), the magnitude of CMT alignment was considerably lower than in *C. hirsuta* cells, as seen by the shorter red lines (compare Figure 28 with Figure 29). At 0h, the distribution of CMT angles in exocarp cells of both control and sample fruit is skewed towards high angles, indicating a transverse CMT alignment (Figure 29). At 24 h, the distribution of CMT angles switched is now skewed towards low angles in both control and sample fruit, indicating a switch to a longitudinal CMT alignment (Figure 29). This longitudinal CMT alignment is then maintained in both control and sample fruit at 48 h, 72 h and 360 h time points (Figure 29). Therefore, repeated Dex treatment had little effect on CMT organization in the exocarp cells of *A. thaliana* *35S::GFP:TUA6; amiRKTN1* fruit (Figure 29). Dex-treated fruit also stained blue at every time point when assayed for GUS expression, indicating expression of the *amiRKTN1* construct, although staining was reduced and patchy at 360 h (Figure 29), associated with an increase in *KTN1* gene expression at this time point (Figure 27).

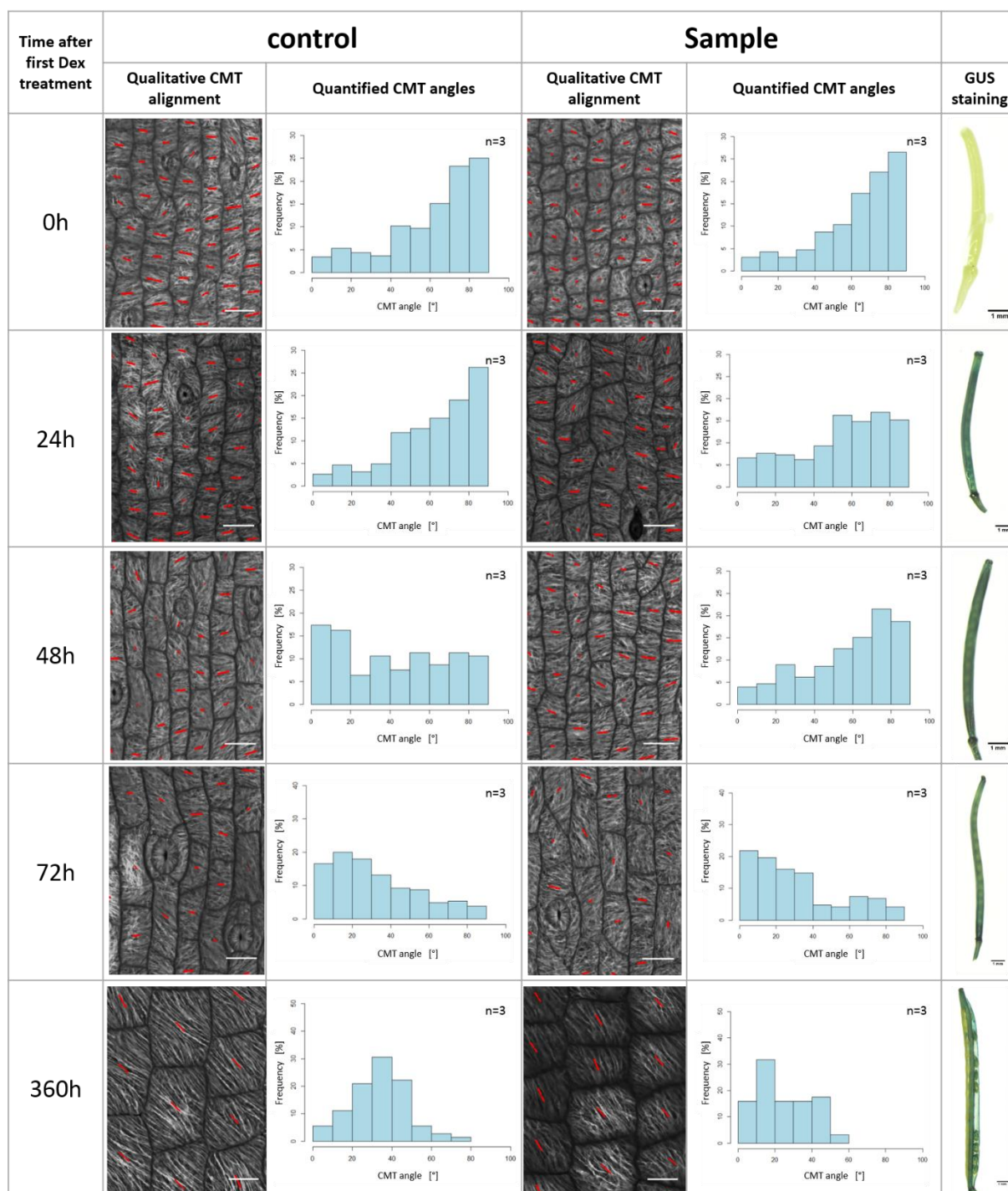


Figure 28: Sustained Dex treatment of *C. hirsuta* 35S::GFP:TUA6; *amiRKTN1* fruit pods. Fruit were treated every 24 h with 100 μ M Dex or water for 10 min and analyzed at 0 h, 24 h (1 x Dex), 48 h (2 x Dex), 72 h (3 x Dex) and 360 h (15 x Dex). The length of the red line represents the extent of CMT organisation and its orientation represents the average CMT alignment of the cell. Histograms plot the frequency of cells with average CMT angles in bins of 10° from 0 – 90°. GUS stained fruit pods at each time point show no expression of the construct at 0 h (no stain) and expression at all other time points (blue stain). Scale bars: 20 μ m.

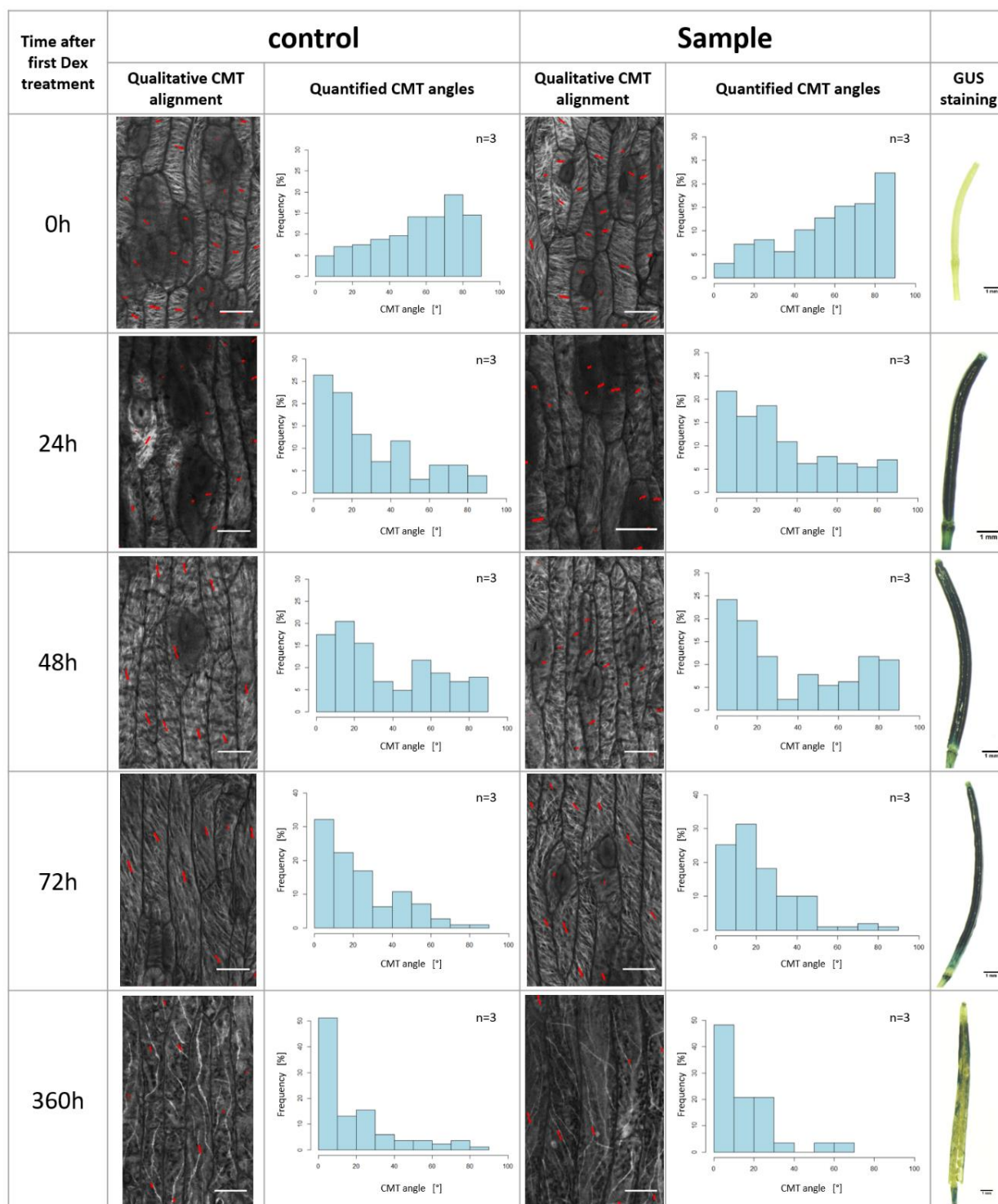


Figure 29: Sustained Dex treatment of *A. thaliana* 35S::GFP:TUA6; *amiRKTN1* fruit pods. Fruit were treated every 24 h with 100 μ M Dex or water for 10 min and analyzed at 0 h, 24 h (1 x Dex), 48 h (2 x Dex), 72 h (3 x Dex) and 360 h (15 x Dex). The length of the red line represents the extent of CMT organisation and its orientation represents the average CMT alignment of the cell. Histograms plot the frequency of cells with average CMT angles in bins of 10° from 0 – 90°. GUS stained fruit pods at each time point show no expression of the construct at 0 h (no stain) and expression at all other time points (blue stain). Scale bars: 20 μ m.

Next, I investigated whether the 24 h delay in CMT reorientation caused by *KTN1* silencing had any effect on the dynamics of exocarp cell shape change in *C. hirsuta*. By calculating the aspect ratio of exocarp cells during the time course of Dex treatment in *C. hirsuta* *35S::GFP:TUA6; amiRKTN1* fruit, I found that cells transitioned from square to elongate to square, similar to wild type (Figure 10 and Figure 11), irrespective of Dex treatment (Figure 30). Cells with an aspect ratio of approx. 2, indicating an elongate, rectangular shape, are statistically more similar at 48 h in untreated fruit and 72 h in Dex-treated fruit, than between the same time points, indicating a delayed progression (Figure 30). However, this result is unclear due to large variation in the data (Figure 30).

Quantifying the aspect ratio of exocarp cells in *A. thaliana* *35S::GFP:TUA6; amiRKTN1* fruit showed a significant difference to *C. hirsuta* (Figure 30). In contrast to *C. hirsuta*, *A. thaliana* exocarp cells remained rectangular and elongate with a mean aspect ratio > 1 throughout the time course (Figure 30), similar to previous results (Figure 11). Reduced *KTN1* gene expression (Figure 27) did not cause exocarp cells to deviate from this rectangular shape in *A. thaliana* *35S::GFP:TUA6; amiRKTN1* fruit (Figure 30), just as it did not disrupt CMT organization in exocarp cells (Figure 29).

To investigate whether the slight delay in CMT reorientation caused by *KTN1* silencing was likely to affect explosive pod shatter, I analysed valve coiling in *C. hirsuta* *35S::GFP:TUA6; amiRKTN1* fruits (Figure 31). I repeated the experimental procedure described above for sustained Dex treatment, continuing the time course for a total of 384 h. Both Dex-treated and untreated valves showed very similar coiling in this experiment (Figure 31). By following the same procedure to assess the coiling response of valves to osmotic treatments (Figure 19), I found that valves coiled more tightly in water and more loosely in 4 M NaCl solution, irrespective of Dex treatment

(Figure 31). By calculating the diameter of valve coils in each osmotic treatment, I found no significant difference between the coiling of Dex-treated and untreated fruit (Figure 32). Therefore, I found no evidence that reducing *KTN1* gene expression perturbed the explosive coiling of *C. hirsuta* fruit.

I aimed to further verify that reduced *KTN1* expression did not affect the turgor-driven contraction of exocarp cells that is required for explosive coiling of *C. hirsuta* valves. To do this, I analysed the response of Dex-treated *C. hirsuta* 35S::*GFP:TUA6*; *amiRKTN1* valves to osmotic treatments at the cellular level. I followed the same method described previously to cut short fruit segments and perform CLSM in both high turgor and low turgor solutions after cell wall staining with PI (Figure 19 and Figure 20). I used *C. hirsuta* 35S::*GFP:TUA6*; *amiRKTN1* fruit after a 360 h time course of daily treatment with 100 μ M Dex or control solutions. Specifically, I imaged the same exocarp cells in pure water (high turgor treatment) and after 45 min in 1 M NaCl (low turgor treatment). I loaded the CLSM stacks into MorphoGraphX software to generate a 3D mesh of the exocarp cells in high and low turgor treatments and calculated the changes in cell volume and directional expansion and shrinkage in these cells in response to osmotic treatments. I summarize the results of five adjacent exocarp cells in Dex-treated (Figure 34) and untreated (Figure 33) *C. hirsuta* fruit. Cells responded similarly to osmotic treatments irrespective of Dex treatment, indicating that reduced *KTN1* expression did not affect the turgor-driven contraction of exocarp cells (Figure 33, Figure 34 and Table 5). In response to increasing turgor, cells increased in volume, depth and width, while decreasing in length (Figure 33, Figure 34 and Table 5), which is similar to previous results (Hofhuis *et al.*, 2016). However, plasmolyzed cells were on average 5.16 % (control fruit, Figure 33) and 3.4 % (Dex-treated fruit, Figure 34) longer than turgid cells, which is a smaller difference in cell length between plasmolyzed and turgid cells than previously reported (Hofhuis *et al.*, 2016). This

difference may reflect that I used whole fruit rather than valve segments in my experiment (discussed further in discussion section).

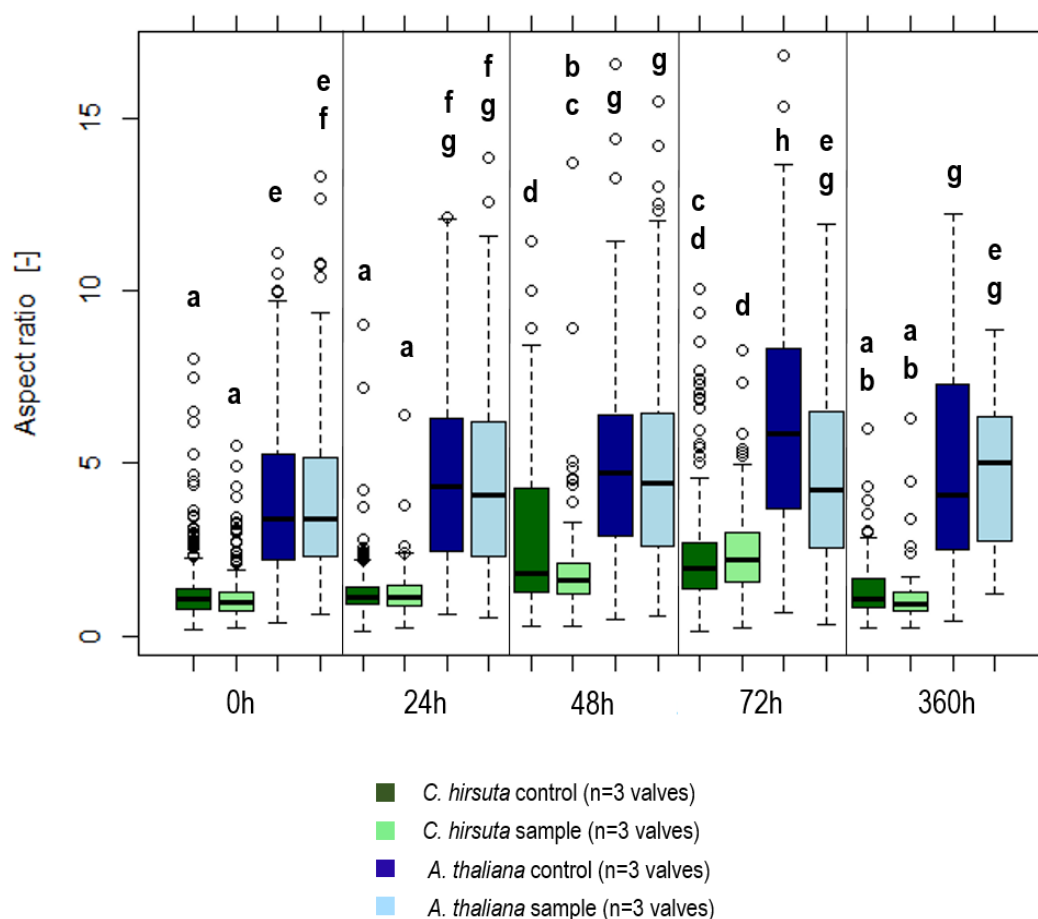


Figure 30: Aspect ratio analysis of *C. hirsuta* and *A. thaliana* 35S::GFP:TUA6; *amiRKTN1* fruit exocarp cells treated with 100 μ M Dex and 0.03 % Silwet (sample) and water with 0.03 % Silwet (control), respectively. Box and whisker plots: box delimits the 2nd and 3rd quartiles, whiskers show the 1st and 4th quartiles, white circles show outliers, black lines show mean. Statistical significance was determined at 0.05 by an ANOVA Tukey test.

Table 5: Effect of sustained Dex treatment on explosive pod shatter. The numbers are mean values of the analysed segmented cells.

		Change in length		Change in width		Change in depth		Change in volume
		μ m	%	μ m	%	μ m	%	
Control	H ₂ O	16.78	- 5.16	27.46	+ 0.94	10.97	+ 31.09	+ 55.57
	NaCl	17.64		27.20		7.56		
Sample	H ₂ O	18.17	- 3.40	26.08	+ 4.61	11.78	+ 9.40	+ 16.00
	NaCl	18.79		24.88		10.67		

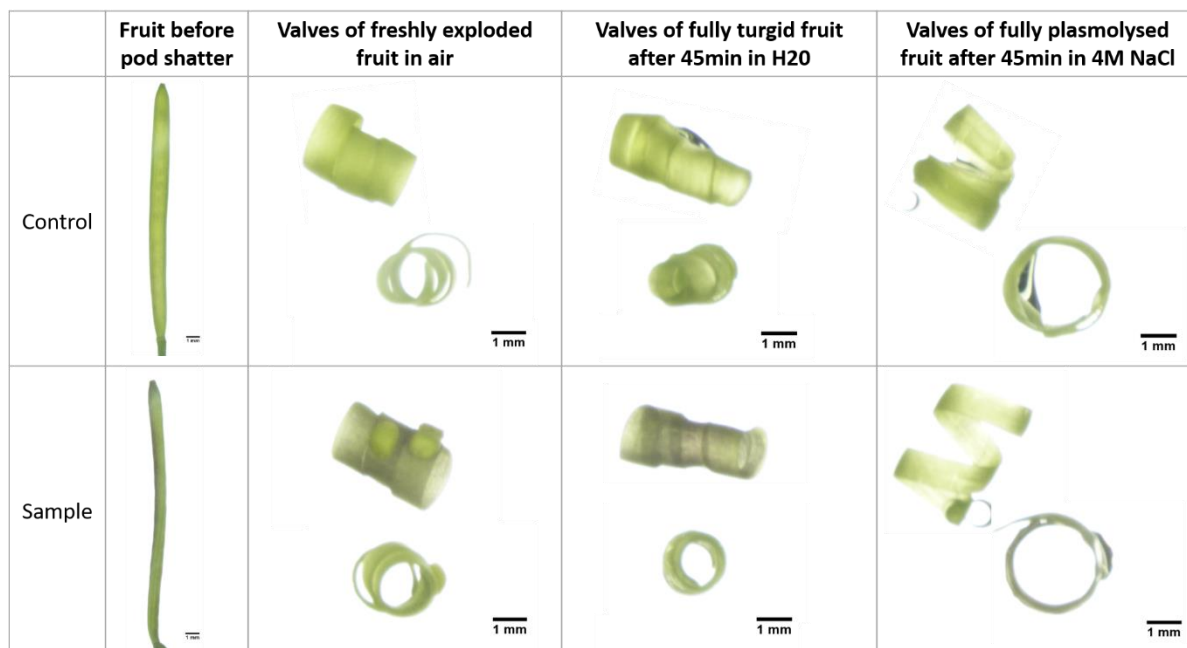


Figure 31: Sustained 100 μ M Dex treatment of *C. hirsuta* 35S::GFP:TUA6; *amiRKTN1* fruits does not affect explosive valve coiling. Fruit pods were manually triggered to explode at time point 384 h and valves were photographed in air and after high turgor (pure water) and low turgor (4 M NaCl) treatments.

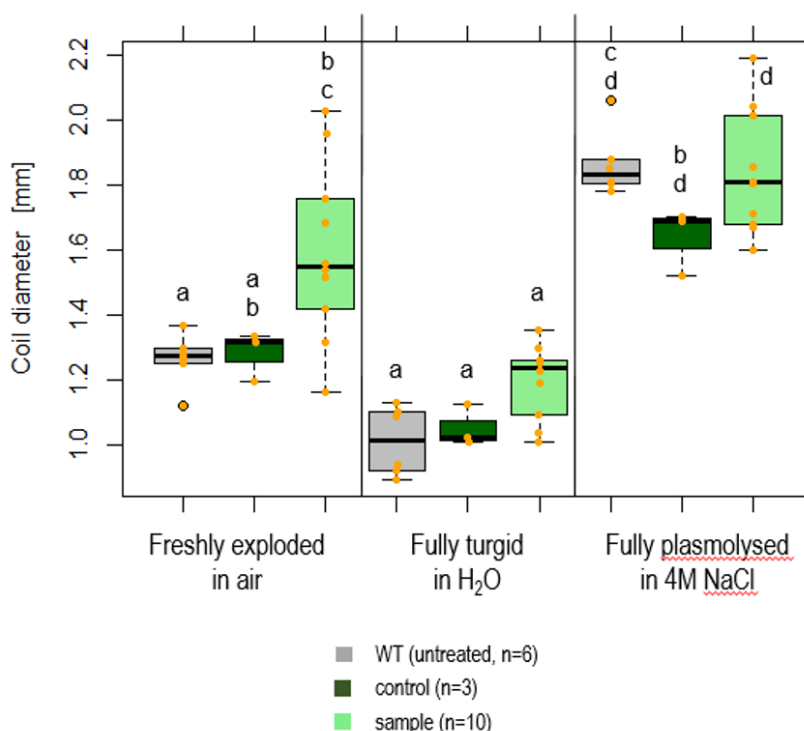


Figure 32: Diameter of valve coils following osmotic treatments of *C. hirsuta* 35S::GFP:TUA6; *amiRKTN1* fruits after sustained treatment with 100 μ M Dex. Box and whisker plots: box delimits the 2nd and 3rd quartiles, whiskers show the 1st and 4th quartiles, white circles show outliers, black lines show mean. Statistical significance was determined at 0.05 by an ANOVA Tukey test.

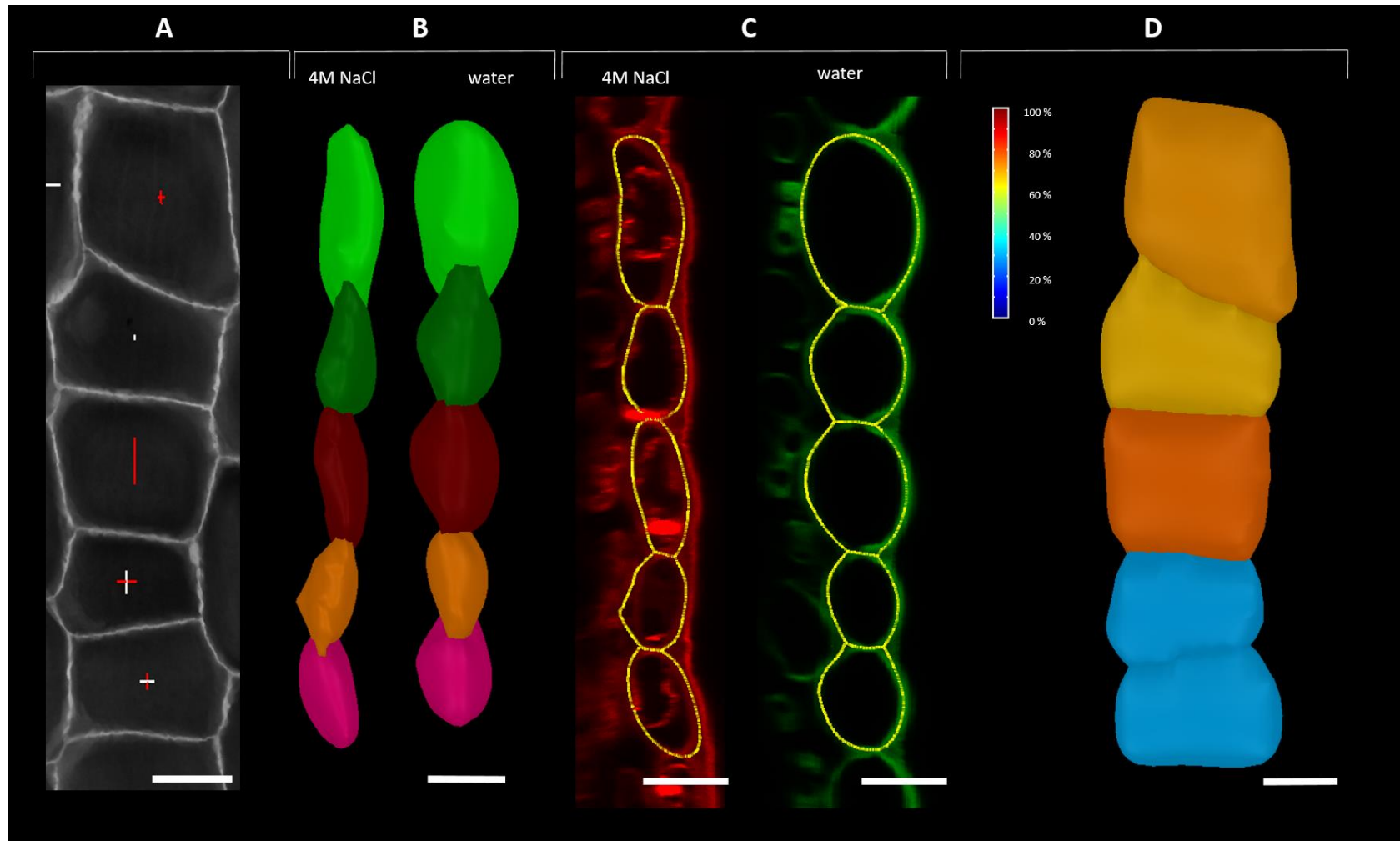


Figure 33: Dex treatment of *C. hirsuta* 35S::GFP:TUA6;amiRKTN1 fruits before explosive pod shatter. The fruit analysed fruit pods were repeatedly dipped in water. A) Top view of PI-stained cells before osmotic treatment. The crosshairs show the principal directions of shrinkage (red) and expansion (white) in comparison to salt treated cells. B) The segmented exocarp cells post and prior salt treatment. C) Side view of PI-stained cells post and prior salt treatment. D) Segmented exocarp cells post and prior salt treatment. The heat map shows cell volume. The scale is 20µm.

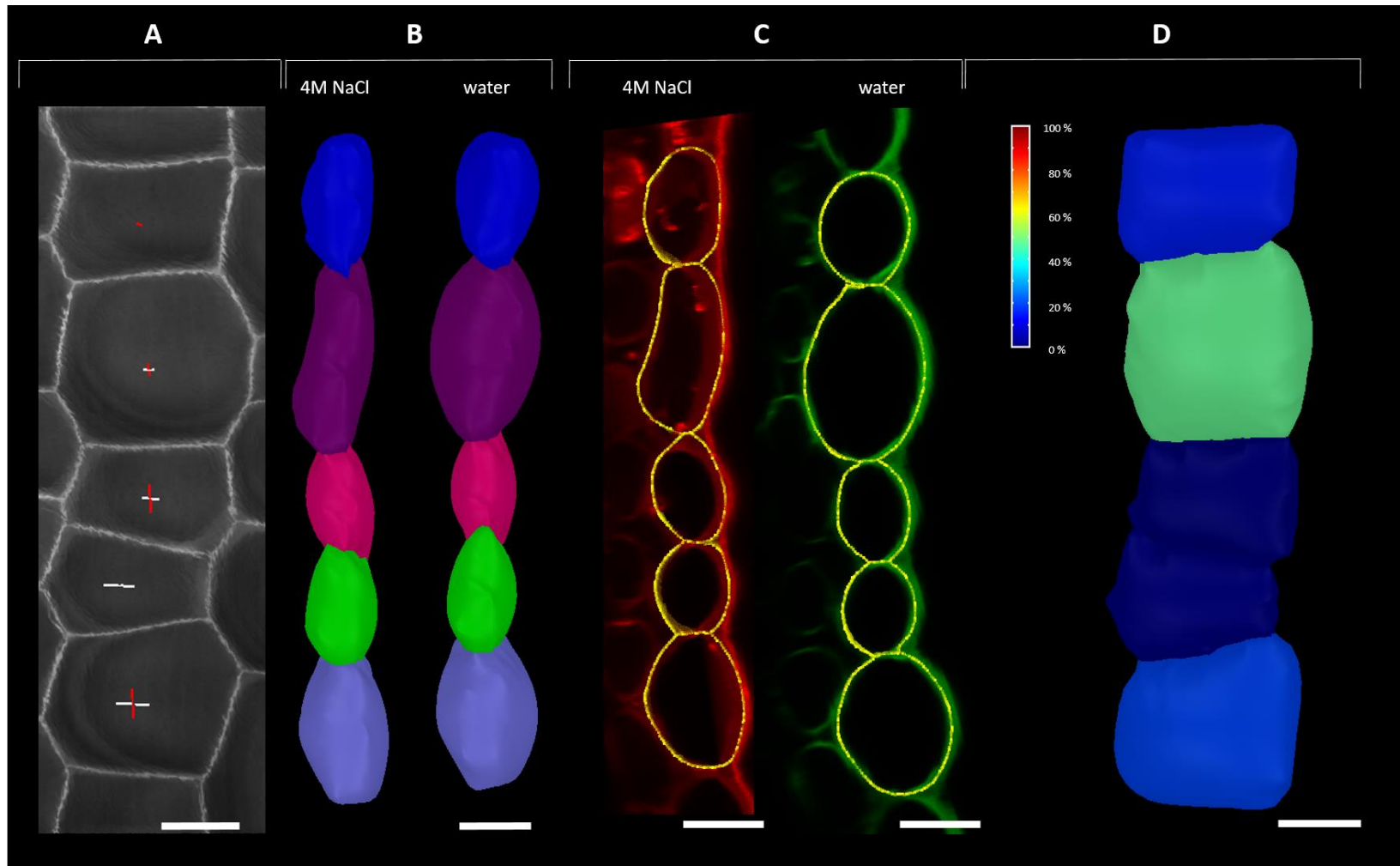


Figure 34: Dex treatment of *C. hirsuta* 35S::GFP:TUA6;amiRKTN1 fruits before explosive pod shatter. The fruit analysed fruit pods were repeatedly dipped in 100 µM Dex. A) Top view of PI-stained cells before osmotic treatment. The crosshairs show the principal directions of shrinkage (red) and expansion (white) in comparison to salt treated cells. B) The segmented exocarp cells post and prior salt treatment. C) Side view of PI-stained cells post and prior salt treatment. D) Segmented exocarp cells post and prior salt treatment. The heat map shows cell volume. The scale is 20µm.

4. Discussion

4.1. Summary

During my project, I characterized the dynamics of CMT alignment during fruit development and its function in explosive pod shatter in *C. hirsuta*. Further, I performed experiments to test and support the prediction from previous work (Hofhuis *et al.*, 2016) that cell shape and anisotropy contribute to explosive pod shatter in *C. hirsuta*.

By characterising fruit development in *C. hirsuta* and *A. thaliana*, I showed that the exocarp cells of *C. hirsuta* fruit show more highly organised CMT alignments and a more pronounced reorientation of CMT alignment in comparison to *A. thaliana*. I quantified the dynamic changes in exocarp cell shape during *C. hirsuta* fruit development and showed that these dynamics did not occur in *A. thaliana* fruit. I showed that CMT alignment in *C. hirsuta* and *A. thaliana* exocarp cells reoriented from transverse to longitudinal direction within 24 h of the pods reaching 7 mm length. This reorientation of CMT changes the alignment of cellulose microfibrils from transverse to a more longitudinal direction in *C. hirsuta* exocarp cells (Hofhuis *et al.*, 2016), providing anisotropic cell wall properties.

Disrupting exocarp CMT alignment with sustained oryzalin treatment was sufficient to abolish explosive pod shatter in *C. hirsuta* fruit. CMT depolymerization caused the exocarp cells to become round and prevented the dynamic changes in cell shape that characterize wild-type development. At the organ-level, these fruit valves did not coil and were insensitive to osmotic treatments. These results indicate that CMT alignment, and its consequent effects on cell shape and cell wall anisotropy, are required for exocarp cells to contract in response to increased turgor. However, the perturbation to CMT alignment that I achieved by silencing *KTN1* gene expression, was not sufficient to affect explosive pod shatter in *C. hirsuta* fruit. In summary, my

results support the prediction that exocarp cell shape and cell wall anisotropy are important for the mechanism of turgor-driven contraction that generates the tension required for explosive pod shatter in *C. hirsuta* (Hofhuis *et al.*, 2016).

4.2. Staging Fruit Development in *C. hirsuta* and *A. thaliana*

By comparing fruit development between *C. hirsuta* and *A. thaliana*, I showed an overall similarity in growth and morphology, particularly up until stage 17b when the fruit reached their final length and start to grow in the width (Figure 5). Key differences at this stage are: (1) *A. thaliana* fruits have curved valves attached to a narrow replum, while *C. hirsuta* fruits have flatter valves attached to a wider replum. (2) *C. hirsuta* valves are corrugated due to the larger seeds (Hay *et al.*, 2014) pressing against the flatter valves; and (3) *C. hirsuta* valves are competent to coil and explosively disperse the seeds during stages 17b and 18, while *A. thaliana* valves dehisce at stage 19 and seeds disperse during stage 20.

By using CLSM to visualize 35S::*GFP:TUA6* expression in exocarp cells, I showed a reorientation of CMT alignment from transverse to longitudinal direction, relative to the long axis of the fruit, in both species during stage 16 (Figure 4). CMT are highly dynamic filaments, located adjacent to the plasma membrane, which guide the direction of cellulose microfibril synthesis by the cellulose synthase complex (Paredes, 2006). Growth is generally larger perpendicular to the orientation of stiff cellulose microfibrils in the cell walls, which is in turn controlled by CMT orientation (Crowell *et al.*, 2011; Green, 1962; Ledbetter and Porter, 1963; Paredes, 2006). Thus, fruits are predicted to be stiffer in the width direction when CMT arrays are transversely aligned, resulting in growth in the length direction (Figure 5 and Figure 9). When CMT arrays reorient in stage 16, fruit are predicted to be stiffer in the length direction,

resulting in growth in the width direction (Figure 5 and Figure 9). Therefore, the observed CMT reorientation in exocarp cells of *C. hirsuta* and *A. thaliana* is predicted to contribute to the change in growth direction (anisotropy) during late stages of fruit development (Figure 7).

I found that the magnitude of CMT alignment in exocarp cells was higher in *C. hirsuta* than *A. thaliana* (Figure 9). I also found that exocarp cell shape changed dynamically during fruit development in *C. hirsuta* but not *A. thaliana* (Figure 11). By calculating the aspect ratio of exocarp cells throughout fruit development, I showed that *A. thaliana* cells had an elongate, rectangular shape (aspect ratio > 1) at all stages of fruit development (Figure 11). In contrast, *C. hirsuta* exocarp cells had a square shape (aspect ratio ~ 1) at stage 12, changed to a wide rectangular shape (aspect ratio < 1) at stages 13- 15, transitioned through to a square and then to an elongate, rectangular shape (aspect ratio > 1) at stage 16 – 17b, before changing to a square shape (aspect ratio ~ 1) at stage 18 (Figure 11). The reorientation of CMT arrays from transverse to longitudinal begins at stage 16 and precedes the transition from an elongate, rectangular cell shape to a square cell shape at stage 18. This transition produces the particular cell shape required in computational models for turgor-driven cell contraction (Hofhuis *et al.*, 2016). Moreover, the longitudinal alignment of CMT arrays is predicted to dictate a longitudinal alignment of stiff cellulose microfibrils in the cell walls, which is required in computational models for turgor-driven cell contraction (Hofhuis *et al.*, 2016). Therefore, my results validate the observations reported in (Hofhuis *et al.*, 2016).

4.3. CMT Disruption with Oryzalin

My observations of CMT organization and cell shape in *C. hirsuta* exocarp cells fit the expectations of computational models for turgor-driven cell contraction (Hofhuis *et al.*, 2016). However, a very important part of my project was to perturb CMT organization in order to test the effect on turgor-driven cell contraction and ultimately on explosive pod shatter. To disrupt CMT alignment, I used the dinitroaniline oryzalin, which is one of the most common MT-active herbicides (Dostál and Libusová, 2014; Dumontet and Jordan, 2010). Oryzalin causes the depolymerisation of MT and thus inhibits incorporation of tubulin dimers into the MT fibril, which results in bundled CMT (Baskin *et al.*, 1994; Dostál and Libusová, 2014; Dumontet and Jordan, 2010).

In contrast to my experimental design, oryzalin treatments are often performed in seedlings to perturb young, growing tissues, such as roots, hypocotyls and epidermal pavement cells of leaves or cotyledons (Baskin *et al.*, 1994; Akita *et al.*, 2015). In these cases, seedlings are grown on oryzalin-containing agar at concentrations between nanomolar until very low micromolar range of the herbicide (Baskin *et al.*, 1994; Akita *et al.*, 2015). In my case, I found that a suitable concentration to disturb CMT alignment within the fruit exocarp was 125 μM . This higher oryzalin concentration was required for a number of reasons: (1) My target tissues are in the fruit. Fruit develop at the end of a plant's life cycle so it is not appropriate to grow plants continuously, under sterile conditions, on oryzalin-containing agar. (2) My target cells are in differentiated tissues. In particular, the fruit exocarp has a thick cuticle which protects the fruit against dehydration, abiotic and biotic stresses (Yeats and Rose, 2013; Domínguez *et al.*, 2010). The composition and thickness of the cuticle can be modulated through development and in response to such stresses to ensure successful seed maturation (Domínguez *et al.*, 2010). Therefore, in contrast to

chemical uptake by roots, which is very efficient (Chaffey, 2008), chemical uptake by the fruit exocarp is likely to be inefficient. However, I could successfully affect CMT alignment in the exocarp cells of mature fruits by dipping branches in a solution of 125 μM oryzalin containing 0.03 % Silwet for 5 min (Figure 13).

A closer look at my oryzalin dose-response experiments shows that an exposure to 50 μM oryzalin for 5 min already caused a slight effect on CMT alignment (Figure 13). Nevertheless, I decided to continue with 125 μM oryzalin since this concentration caused the characteristic CMT bundling which is the phenotype described in literature as indicating CMT depolymerization (Baskin *et al.*, 1994; Dostál and Libusová, 2014; Dumontet and Jordan, 2010). Although CMT bundling was increased by treatment with 250 μM oryzalin, I preferred to use 125 μM oryzalin as the lowest concentration that disrupted CMT organization without impacting the fruit phenotype. However, increasing the oryzalin concentration to 500 μM caused only a slight effect on CMT alignment (Figure 13). This might be due to a difference in fruit maturity. Based on cell shape, the exocarp cells in the 500 μM oryzalin treatment were more mature than other samples (Figure 9 and Figure 13). Therefore, despite the addition of 0.03% Silwet as a surfactant, a thicker cuticle in more mature fruit may inhibit the diffusion of oryzalin into the exocarp cells.

I chose to start my time-course experiments in stage 16 fruit, which is the point when exocarp CMT arrays reorient from the transverse to longitudinal direction. Because I dissolved oryzalin in DMSO, I added DMSO and 0.03 % Silwet to my control water solution. Although I made a mistake in calculating the amount of DMSO in control solutions (see Materials and Methods 2.1), I found that CMT reorientation of control fruits was comparable to the wild type (Figure 9 and Figure 14). Therefore, treatment with DMSO did not affect CMT alignment in my experiments (Figure 14), which is consistent with previous results (Akita *et al.*, 2015).

Because it is critical to start each time course before CMT reorientation, I investigated the degree of variation in the dynamics of CMT reorientation in stage 16 fruit (Figure 9 and Figure 12). I found that stage 16 fruit invariantly had a transverse alignment of exocarp CMT arrays, and that I could reliably identify this stage based on fruit length (Table 3). Single treatments with oryzalin did not show CMT bundling in the exocarp cells of *C. hirsuta* fruit, and gave variable results between the two replicates. However, in replicate 1, oryzalin treatment reduced the magnitude of aligned CMTs after 24 h, which was sustained for 48 h, before cells recovered a longitudinal alignment CMT alignment, similar to control samples, after 72 h (Figure 14). These results indicate that the depolymerizing effect of oryzalin, caused by binding to tubulin dimers, is reversible (Hoffman and Vaughn, 1994; Hugdahl and Morejohn, 1993). Moreover, it shows that when CMTs recovered after oryzalin treatment they did not recover their pre-treatment transverse alignment, but rather the longitudinal alignment that their developmental age dictates.

To address the reversible effect of oryzalin and the absence of CMT bundling, I sustained daily oryzalin treatments through until *C. hirsuta* fruit were competent to explode. Furthermore, I increased treatment time with 125 μ M oryzalin from 5 min to 10 min to ensure a sufficient oryzalin exposure. These conditions caused CMT bundling and abolished the alignment of CMT arrays such that the distribution of CMT angles could not be calculated (Figure 15). These effects were visible 24 h after oryzalin treatment (Figure 15), similar to the dose-response experiments (Figure 13), suggesting a possible experimental handling mistake in the single oryzalin treatments (Figure 14). Another effect of sustained oryzalin treatment was to cause exocarp cell shape to become rounded (Figure 15). This already started 72 h after the first oryzalin treatment and cells were distinctly rounded with aberrant bulges at 384 h (Figure 15). I was not able to quantify this effect on cell shape by calculating the aspect ratio of the cells as

this MorphoGraphX process, which fits a square in the single exocarp cells does not take round cell edges into consideration (2.10.2). The effect of oryzalin on cell shape is also described in (Corson *et al.*, 2009). Here, the authors describe the loss of anisotropy in shoot apical meristem cells of *A. thaliana* caused by oryzalin treatment, such that cell growth became isotropic, resulting in round cells (Corson *et al.*, 2009). Thus, I successfully changed cell growth and geometry in the fruit exocarp of *C. hirsuta* by depolymerizing CMT with repeated oryzalin treatment.

This sustained oryzalin treatment through the final stages of fruit development was sufficient to prevent explosive pod shatter. By treating fruits only from stage 16 onwards, they developed normal length and overall morphology, similar to control fruit (Figure 17). But oryzalin treatment specifically blocked the explosive coiling of valves (Figure 17). This result shows that aligned CMT arrays, and their influence on directional cell growth and shape in the exocarp, are required for explosive coiling of the valves in *C. hirsuta*.

Valve coiling results from differential contraction of tissues in the valve and depends on a mechanism of turgor-driven contraction in the exocarp cell layer (Hofhuis *et al.*, 2016). By analyzing the curvature of whole valves in response to osmotic treatments, I showed that oryzalin treatment rendered the valves unresponsive to changes in turgor (Figure 17 and Figure 18). This suggests that the mechanism of turgor-driven contraction in the exocarp cell depends on aligned CMT arrays and the cell shape and anisotropy that these alignments dictate.

I aimed to analyze how oryzalin affected the cellular response to osmotic treatments, but I had a number of problems with these experiments. First, I performed these experiments with segments of whole fruit, while previous experiments used segments of valve tissue (Hofhuis *et al.*, 2016). Valves are free to deform by coiling, however in my case, the valves were attached to the rest of the fruit and not free to

deform. Therefore, the amount of exocarp cell contraction in response to increased turgor in my control fruits (Figure 19) was lower than previously reported (Hofhuis *et al.*, 2016). The second problem was verifying that cells were undamaged and competent to respond to osmotic treatments. For example, while exocarp cells in control fruit changed considerably in volume between plasmolyzed and turgid, as expected (Figure 19 D), cells in oryzalin-treated fruit did not (Figure 20 C). A technical explanation for this is that the oryzalin-treated cells were damaged and unable to inflate and deflate as expected in response to changes in turgor pressure. Therefore, although it is interesting that the anisotropic response to turgor found in wild-type exocarp cells is abolished by oryzalin treatment (Figure 20 A-C), this result needs to be confirmed by replication.

In summary, I successfully depolymerized CMT in exocarp cells during late stages of *C. hirsuta* fruit development by daily oryzalin treatments. CMT depolymerization disrupted the wild-type transitions in exocarp cell shape by changing the direction of cell growth from anisotropic to isotropic, resulting in round exocarp cells. This perturbation was sufficient to abolish turgor-driven contraction of exocarp cells and explosive pod shatter. This result confirms the prediction from previous modeling approaches that exocarp cell contraction is an active, turgor-driven process, that relies on anisotropy and cell shape (Hofhuis *et al.*, 2016). Importantly, the results of my perturbation experiments functionally link CMTs to explosive pod shatter.

4.4. *KTN1* Silencing During Fruit Development

Given that CMT depolymerization was sufficient to abolish explosive pod shatter, I wanted to investigate the role of CMT organization. The protein *KTN1* is important for CMT organisation since it affects CMT alignment and orientation (Mcnally and Vale, 1993; Vaughn *et al.*, 2011; Wang *et al.*, 2013). *KTN1* increases MT dynamics by cleaving the MT lattice enabling a quick relocation of the MT polymer (Alberts *et al.*, 2003; Shaw *et al.*, 2003).

I used an amiR*KTN1*, inserted in a two-component system, to silence *KTN1* gene expression in *C. hirsuta* and *A. thaliana* 35S::*GFP:TUA6* pods during fruit development. I found, that all treatments with a solution of 100 μ M Dex and 0.03 % Silwet caused a reduction in *KTN1* expression indicating successful induction of amiR*KTN1* expression (Figure 24, Figure 26 and Figure 27). However, the reduced *KTN1* gene expression neither perturbed CMT alignment sufficiently during fruit development nor affected explosive pod shatter in *C. hirsuta* (Figure 25, Figure 28, Figure 29, Figure 31 and Figure 32). Despite reduced *KTN1* expression, *C. hirsuta* valve coiling responded to osmotic treatments and exocarp cells responded to increased turgor pressure by increasing in volume, depth and width, while decreasing in length (Figure 33, Figure 34 and Table 5), which is similar to previous results (Hofhuis *et al.*, 2016).

These results suggest that *KTN1* function may not be required in fruit exocarp cells at late stages of development to control the alignment of CMT arrays. For example, plant hormones (especially auxin) contribute to CMT organisation (Esau 1977; Zandomeni & Schopfer 2005; Sasidharan *et al.*, 2014), and may play a more important role in regulating CMT dynamics in the fruit exocarp. Alternatively, *KTN1*

gene expression may not be sufficiently reduced in these experiments to assess *KTN1* function.

5. Future Perspective

In my thesis, I analysed different fruit samples at different stages of development to assess exocarp cell shape and CMT alignment. In a next step, live imaging of fruit during development would allow a more detailed analysis of growth parameters like growth distribution, duration and direction. Moreover, live imaging could be used to quantify the contribution of cell division to establishing the files of short, wide exocarp cells that distinguish stage 13-15 *C. hirsuta* fruit from *A. thaliana* fruit. Since the *KTN1* gene silencing achieved by amirKTN1 induction was not sufficient to affect CMT alignment, a different approach may be useful. For example, a *KTN1* loss of function mutant could be generated in *C. hirsuta* by CRISPR/Cas9. Another approach could focus on other factors that contribute to CMT organisation. After oryzalin treatment, CMT did not recover their pre-treatment transverse alignment, but rather a longitudinal alignment. This suggests that developmental stage dictates CMT alignment and possible candidates to test could be hormones such as auxin. To further understand the role of exocarp cell anisotropy in explosive pod shatter, cell wall properties such as the degree of pectin methylesterification could be analysed during *C. hirsuta* fruit development.

Figures

Figure 1: Scanning electron micrograph of an <i>A. thaliana</i> WT fruit at stage 17.	4
Figure 2: Process of ballistical seed dispersal of <i>C. hirsuta</i>	7
Figure 3: Result of osmotic treatment and FEM simulation of pressurized exocarp cells.	8
Figure 4: Schematic description of the four parameters for describing growth properties. ..	10
Figure 5: Phenotypic comparison of different fruit developmental stages of <i>A. thaliana</i> and <i>C. hirsuta</i> , respectively.	26
Figure 6: Single <i>A. thaliana</i> fruit pod fixed to microscopic slide with an adhesive tag to monitor its growth.	28
Figure 7: Growth of <i>C. hirsuta</i> (A) and <i>A. thaliana</i> (B) wild type (WT) and GFP::TUA6 marker lines.	29
Figure 8: Comparison of fruit growth between <i>C. hirsuta</i> and <i>A. thaliana</i> WT and 35S::GFP:TUA6 marker lines, respectively, according to the different fruit pod stages.	30
Figure 9: CMT alignment in exocarp cells at different fruit developmental stages in <i>A. thaliana</i> and <i>C. hirsuta</i>	32
Figure 10: Schematic explanation of the aspect ratio.	33
Figure 11: Aspect ratio (shown as heat map) for exocarp cells of <i>A. thaliana</i> and <i>C. hirsuta</i> during fruit development..	35
Figure 12: Time series of CMT orientation in individual fruit pods of <i>C. hirsuta</i> and <i>A. thaliana</i> GFP::TUA6 plants.....	38
Figure 13: Ascertaining a suitable oryzalin concentration for CMT disruption in adult fruit pods..	40
Figure 14: Single oryzalin treatment of <i>C.hirsuta</i> 35S::GFP:TUA6 fruit pods (stage 16).	42
Figure 15: Sustained oryzalin treatment of <i>C. hirsuta</i> 35S::GFP:TUA6 fruit pods.	46

Figure 16: Aspect ratio analysis of <i>C. hirsuta</i> 35S::GFP:TUA6 valve exocarp cells treated with 125 μ M oryzalin (sample) and 125 μ M DMSO (control), respectively..	47
Figure 17: Sustained oryzalin treatment of <i>C. hirsuta</i> 35S::GFP:TUA6 fruits abolishes explosive valve coiling.	51
Figure 18: Quantification of coil diameters of osmotic treated <i>C. hirsuta</i> 35S::GFP:TUA6 fruits after a continuous chemical treatment (125 μ M DMSO and 125 μ M oryzalin, respectively) in a 24 h rhythm.....	51
Figure 19: Osmotic treatment of <i>C. hirsuta</i> 35S::GFP:TUA6 fruits before explosive pod shatter.	52
Figure 20: Osmotic treatment of <i>C. hirsuta</i> 35S::GFP:TUA6 fruits before explosive pod shatter.	53
Figure 21: Alignment of amiRKTN1 with <i>C. hirsuta</i> KTN1 (CARHR074160.1).	55
Figure 22: Dexamethasone inducible two-component system carrying amiRKTN1 for posttranslational KTN1 silencing.....	56
Figure 23: Dex-induction of the GUS marker gene in the amiRKTN1 two-component construct.	57
Figure 24: Quantification of KTN1 gene expression levels by RT-qPCR in seedlings of <i>C. hirsuta</i> and <i>A. thaliana</i> 35S::GFP:TUA6; amiRKTN1 lines grown 48 h on 100 μ M Dex-containing agar.....	58
Figure 25: Repeated Dex treatments of <i>C. hirsuta</i> 35S::GFP:TUA6; amiRKTN1 line T2-8 fruit (stage 16).....	61
Figure 26: RT-qPCR results of <i>C. hirsuta</i> 35S::GFP:TUA6; amiRKTN1 fruit pods repeatedly dipped in a solution of water and 0.03 % Silwet (control) and 100 μ M Dex and 0.03 % Silwet (sample), respectively.....	62

Figure 27: RT-qPCR results of <i>C. hirsuta</i> and <i>A. thaliana</i> 35S::GFP:TUA6; amiRKTN1 fruit pods repeatedly dipped in a solution of water and 0.03 % Silwet (control) and 100 μ M Dex and 0.03 % Silwet (sample), respectively.....	64
Figure 28: Sustained Dex treatment of <i>C. hirsuta</i> 35S::GFP:TUA6; amiRKTN1 fruit pods.	67
Figure 29: Sustained Dex treatment of <i>A. thaliana</i> 35S::GFP:TUA6; amiRKTN1 fruit pods.....	68
Figure 30: Aspect ratio analysis of <i>C. hirsuta</i> and <i>A. thaliana</i> 35S::GFP:TUA6; amiRKTN1 fruit exocarp cells treated with 100 μ M Dex and 0.03 % Silwet (sample) and water with 0.03 % Silwet (control), respectively.....	71
Figure 31: Sustained 100 μ M Dex treatment of <i>C. hirsuta</i> 35S::GFP:TUA6; amiRKTN1 fruits does not affect explosive valve coiling.....	72
Figure 32: Diameter of valve coils following osmotic treatments of <i>C. hirsuta</i> 35S::GFP:TUA6; amiRKTN1 fruits after sustained treatment with 100 μ M Dex.....	72
Figure 33: Dex treatment of <i>C. hirsuta</i> 35S::GFP:TUA6 fruits before explosive pod shatter. .	73
Figure 34: Dex treatment of <i>C. hirsuta</i> 35S::GFP:TUA6 fruits before explosive pod shatter..	74

Tables

Table 1: Table of oligonucleotides used in this project.

Table 2: Overview of *C. hirsuta* and *A. thaliana* growth development according to pod length.

Table 3: Length ranges ascribed to fruit development stages according to data shown in Figure 8.

Sources

- Akita, K., Higaki, T., Kutsuna, N. & Hasezawa, S. 2., 2015. Quantitative analysis of microtubule orientation in interdigitated leaf pavement cells. *Plant Signaling and Behavior*, 10(5), pp.1–6.
- Akita, K., Higaki, T., Kutsuna, N. & Hasezawa, S., 2015. Quantitative analysis of microtubule orientation in interdigitated leaf pavement cells. *Plant Signaling & Behavior*, 10(5), p.e1024396. Available at: <http://www.tandfonline.com/doi/full/10.1080/15592324.2015.1024396>.
- Alberts, B. et al., 2003. *Molekularbiologie der Zelle*, Wiley-VCH, Weinheim.
- Amos, L.A. & Schlieper, D., 2005. Microtubules and maps. *Advances in protein chemistry*, 71, pp.257–298.
- Barbier de Reuille, P. et al., 2015. MorphoGraphX: A platform for quantifying morphogenesis in 4D. *eLife*, 4, p.5864.
- Baskin, T.I., 2005. Anisotropic Expansion of the Plant Cell Wall. *Annual Review of Cell and Developmental Biology*, 21(1), pp.203–222. Available at: <http://www.annualreviews.org/doi/10.1146/annurev.cellbio.20.082503.103053>.
- Baskin, T.I. et al., 1994. Morphology and microtubule organization in Arabidopsis roots exposed to oryzalin or taxol. *Plant & cell physiology*, 35(6), pp.935–942.
- Boudon, F. et al., 2015. A computational framework for 3D mechanical modeling of plant morphogenesis with cellular resolution. *PLoS computational biology*, 11(1), p.e1003950.
- Bowman, J.L., Floyd, S.K. & Sakakibara, K., 2007. Green genes-comparative genomics of the green branch of life. *Cell*, 129(2), pp.229–234.
- Burk, D.H., Liu, B., Zhong, R., et al., 2001. A katanin-like protein regulates normal cell wall biosynthesis and cell elongation. *The Plant cell*, 13(4), pp.807–827.

- Burk, D.H., Liu, B., Zhong, R.Q., et al., 2001. A katanin-like protein regulates normal cell wall biosynthesis and cell elongation. *Plant Cell*, 13(4), pp.807–827.
- Cai, G., 2010. Assembly and disassembly of plant microtubules: tubulin modifications and binding to MAPs. *Journal of Experimental Botany*, 61(3), pp.623–626. Available at: <http://dx.doi.org/10.1093/jxb/erp395>.
- Carpita, N., Tierney, M. & Campbell, M., 2001. Molecular biology of the plant cell wall: searching for the genes that define structure, architecture and dynamics. *Plant molecular biology*, 47(1–2), pp.1–5.
- Chaffey, N., 2008. Handbook of Plant Science. *Annals of Botany*, 101(4), pp.613–614. Available at: <http://www.ncbi.nlm.nih.gov/pmc/articles/PMC2710202/>.
- Chen, X. et al., 2014. Inhibition of cell expansion by rapid ABP1-mediated auxin effect on microtubules. *Nature*, 516(7529), pp.90–93. Available at: <http://www.pubmedcentral.nih.gov/articlerender.fcgi?artid=4257754&tool=pmc.ncbi&rendertype=abstract>.
- Coen, E. et al., 2004. The genetics of geometry. *Proceedings of the National Academy of Sciences of the United States of America*, 101(14), pp.4728–4735.
- Corpet, F., 1988. Multiple sequence alignment with hierarchical clustering. *Nucleic acids research*, 16(22), pp.10881–10890.
- Corson, F. et al., 2009. Turning a plant tissue into a living cell froth through isotropic growth. *Proceedings of the National Academy of Sciences of the United States of America*, 106(21), pp.8453–8458.
- Cosgrove, D.J., 2005. Growth of the plant cell wall. *Nature reviews. Molecular cell biology*, 6(November), pp.850–861.
- Cosgrove, D.J., 2016. Plant cell wall extensibility: Connecting plant cell growth with cell wall structure, mechanics, and the action of wall-modifying enzymes. *Journal of Experimental Botany*, 67(2), pp.463–476.

- Creff, A., Brocard, L. & Ingram, G., 2015. A mechanically sensitive cell layer regulates the physical properties of the Arabidopsis seed coat. *Nature Communications*, 6, p.6382. Available at: <http://www.nature.com/doi/10.1038/ncomms7382>.
- Crowell, E.F. et al., 2011. Differential regulation of cellulose orientation at the inner and outer face of epidermal cells in the Arabidopsis hypocotyl. *The Plant cell*, 23(7), pp.2592–2605.
- Darwin, C., 1881. *The Power of Movement in Plants*.
- Desai, A. & Mitchison, T.J., 1997. Microtubule polymerization dynamics. *Annual Review of Cell and Developmental Biology*, 13(1), pp.83–117. Available at: <https://doi.org/10.1146/annurev.cellbio.13.1.83>.
- Dinneny, J.R. & Yanofsky, M.F., 2005. Drawing lines and borders: How the dehiscent fruit of Arabidopsis is patterned. *BioEssays*, 27(1), pp.42–49.
- Domínguez, E., Heredia-Guerrero, J.A. & Heredia, A., 2010. The biophysical design of plant cuticles: an overview. *New Phytologist*, 189(4), pp.938–949. Available at: <https://doi.org/10.1111/j.1469-8137.2010.03553.x>.
- Dostál, V. & Libusová, L., 2014. Microtubule drugs: Action, selectivity, and resistance across the kingdoms of life. *Protoplasma*, 251(5), pp.991–1005.
- Dumontet, C. & Jordan, M.A., 2010. Microtubule-binding agents: a dynamic field of cancer therapeutics. *Nature reviews. Drug discovery*, 9(10), pp.790–803.
- Esau, K., 1977. *Anatomy of Seed Plants*, 2nd Edition 2nd ed.,
- Ferrándiz, C., 2002. Regulation of fruit dehiscence in Arabidopsis. *Journal of experimental botany*, 53(377), pp.2031–2038.
- Ferrandiz, C., Liljegren, S.J. & Yanofsky, M.F., 2000. Negative regulation of the SHATTERPROOF genes by FRUITFULL during Arabidopsis fruit development. *Science (New York, N.Y.)*, 289(5478), pp.436–438.
- Forterre, Y. et al., 2005. How the Venus flytrap snaps. *Nature*, 433(7024), pp.421–425.

- Fosket, D.E. & Morejohn, L.C., 1992. Structural and Functional Organization of Tubulin. *Annual Review of Plant Physiology and Plant Molecular Biology*, 43(1), pp.201–240. Available at: <https://doi.org/10.1146/annurev.pp.43.060192.001221>.
- Ganguly, A. & Cabral, F., 2011. New insights into mechanisms of resistance to microtubule inhibitors. *Biochimica et biophysica acta*, 1816(2), pp.164–171. Available at: <http://www.ncbi.nlm.nih.gov/pmc/articles/PMC3202616/>.
- Geitmann, A., 2016. Actuators Acting without Actin. *Cell*, 166(1), pp.15–17.
- Goujon, M. et al., 2010. A new bioinformatics analysis tools framework at EMBL-EBI. *Nucleic acids research*, 38(Web Server issue), pp.W695-9.
- Green, P.B., 1962. Mechanism for Plant Cellular Morphogenesis. *Science (New York, N.Y.)*, 138(3548), pp.1404–1405.
- Gu, Q. et al., 1998. The FRUITFULL MADS-box gene mediates cell differentiation during Arabidopsis fruit development. *Development (Cambridge, England)*, 125(8), pp.1509–1517. Available at: <http://eutils.ncbi.nlm.nih.gov/entrez/eutils/elink.fcgi?dbfrom=pubmed&id=9502732&retmode=ref&cmd=prlinks%0Apapers2://publication/uuid/4B5E1FB5-23E0-49BA-BFC2-D1A4F4383879>.
- Hamant, O. et al., 2008. Developmental patterning by mechanical signals in Arabidopsis. *Science (New York, N.Y.)*, 322(5908), pp.1650–5. Available at: <http://classic.sciencemag.org/content/322/5908/1650.full>.
- Hay, A. & Tsiantis, M., 2016. Cardamine hirsuta: a comparative view. *Current opinion in genetics & development*, 39, pp.1–7.
- Hay, A.S. et al., 2014. Cardamine hirsuta: A versatile genetic system for comparative studies. *Plant Journal*, 78(1), pp.1–15.
- Hejnowicz, Z. & Romberger, J.A., 1984. Growth tensor of plant organs. *Journal of Theoretical Biology*, 110(1), pp.93–114. Available at:

- <http://www.sciencedirect.com/science/article/pii/S002251938480017X>.
- Hoffman, J.C. & Vaughn, K.C., 1994. Mitotic disrupter herbicides act by a single mechanism but vary in efficacy. *Protoplasma*, 179(1–2), pp.16–25. Available at: <http://link.springer.com/10.1007/BF01360733>.
- Hofhuis, H. et al., 2016. Morphomechanical Innovation Drives Explosive Seed Dispersal. *Cell*, 166(1), pp.222–233. Available at: <http://www.ncbi.nlm.nih.gov/pmc/articles/PMC4930488/>.
- Hu, Y. et al., 2010. High efficiency transport of quantum dots into plant roots with the aid of silwet L-77. *Plant Physiology and Biochemistry*, 48(8), pp.703–709. Available at: <http://www.sciencedirect.com/science/article/pii/S0981942810000793>.
- Hugdahl, J.D. & Morejohn, L.C., 1993. Rapid and Reversible High-Affinity Binding of the Dinitroaniline Herbicide Oryzalin to Tubulin from Zea mays L. *Plant physiology*, 102(3), pp.725–740.
- J. Sambrook & Russell, D.W., 2001. *Molecular cloning. A laboratory manual*, New York: Cold Spring Harbor Laboratory Press.
- Johnston, J.S. et al., 2005. Evolution of genome size in Brassicaceae. *Annals of botany*, 95(1), pp.229–235.
- Jordan, M.A. & Wilson, L., 2004. Microtubules as a target for anticancer drugs. *Nature reviews. Cancer*, 4(4), pp.253–265.
- Koncz, C. & Shell, J., 1986. The promoter of TL-DNA gene 5 controls the tissue-specific expression of chimaeric genes carried by a novel type of Agrobacterium binary vector. , pp.383–396.
- Lamesch, P. et al., 2012. The Arabidopsis Information Resource (TAIR): improved gene annotation and new tools. *Nucleic acids research*, 40(Database issue), pp.D1202-10.

- Langowski, L., Stacey, N. & Ostergaard, L., 2016. *Diversification of fruit shape in the Brassicaceae family*,
- Larkin, M.A. et al., 2007. Clustal W and Clustal X version 2.0. *Bioinformatics (Oxford, England)*, 23(21), pp.2947–2948.
- Ledbetter, M.C. & Porter, K.R., 1963. A Microtubule In Plant Cell Fine Structure. *The Journal of Cell Biology*, 19(1), p.239 LP-250. Available at: <http://jcb.rupress.org/content/19/1/239.abstract>.
- Liljegren, S.J. et al., 2004. Control of Fruit Patterning in Arabidopsis by INDEHISCENT. *Cell*, 116(6), pp.843–853. Available at: <http://linkinghub.elsevier.com/retrieve/pii/S009286740400217X> [Accessed March 31, 2018].
- Liljegren, S.J., 2000. SHATTERPROOF MADS-box genes control seed dispersal in Arabidopsis. *Nature*, 404(April), pp.766–770. Available at: <http://dx.doi.org/10.1038/35008089>.
- Lin, D. et al., 2013. Rho GTPase signaling activates microtubule severing to promote microtubule ordering in arabidopsis. *Current Biology*, 23(4), pp.290–297. Available at: <http://dx.doi.org/10.1016/j.cub.2013.01.022>.
- Lindeboom, J.J. et al., 2013. A mechanism for reorientation of cortical microtubule arrays driven by microtubule severing. *Science (New York, N.Y.)*, 342(6163), p.1245533.
- Lloyd, C., 2011. Dynamic microtubules and the texture of plant cell walls. *International review of cell and molecular biology*, 287, pp.287–329.
- Lloyd, C.W., 1991. *The cytoskeletal basis of plant growth and form.*, Academic Press Limited.
- Lockhart, J.A., Bretz, C. & Kenner, R., 1967. An Analysis of Cell-Wall Extension. *Annals of the New York Academy of Sciences*, 144(1), pp.19–33. Available at:

- <https://doi.org/10.1111/j.1749-6632.1967.tb33998.x>.
- Martone, P.T. et al., 2010. Mechanics without Muscle: Biomechanical inspiration from the plant world. *Integrative and Comparative Biology*, 50(5), pp.888–907.
- McNally, F.J. & Vale, R.D., 1993. Identification of Katanin , an ATPase That Severs and Disassembles Stable Microtubules. , 75, pp.419–429.
- Mirabet, V. et al., 2017. The self-organization of plant microtubules in three dimensions enables stable cortical localization and sensitivity to external cues. *bioRxiv*. Available at: <http://biorxiv.org/content/early/2017/10/27/210138.abstract>.
- Moore, I. et al., 2006. Transactivated and chemically inducible gene expression in plants. *Plant J*, 45(4), pp.651–683. Available at: http://www.ncbi.nlm.nih.gov/entrez/query.fcgi?cmd=Retrieve&db=PubMed&dopt=Citation&list_uids=16441354.
- Murashige, T. & Skoog, F., 1962. A revised medium for rapid growth and bioassays with tobacco tissue culture. *Physiol. Plant*, 15, pp.473–497.
- Nakamura, M., Ehrhardt, D.W. & Hashimoto, T., 2010. Microtubule and katanin-dependent dynamics of microtubule nucleation complexes in the acentrosomal Arabidopsis cortical array. *Nature cell biology*, 12(11), pp.1064–1070.
- Oda, Y., 2015. Cortical microtubule rearrangements and cell wall patterning. *Frontiers in Plant Science*, 6(April), pp.1–7. Available at: http://www.frontiersin.org/Journal/Abstract.aspx?s=907&name=plant_physiology&ART_DOI=10.3389/fpls.2015.00236%5Cnhttp://journal.frontiersin.org/article/10.3389/fpls.2015.00236/pdf.
- Page, D.R. & Grossniklaus, U., 2002. the Art and Design of Genetic Screens : Arabidopsis Thaliana. *Genetics*, 3(February), pp.124–136.
- Paradez, A., Wright, A. & Ehrhardt, D.W., 2006. Microtubule cortical array organization and plant cell morphogenesis.

- Paredez, A.R., Somerville, C. & Ehrhardt, D., 2006. Visualization of Cellulose Synthase with Microtubules. *Science*, 312(2006), pp.1491–1495. Available at: <http://www.ncbi.nlm.nih.gov/pubmed/16627697>.
- Peaucelle, A., Wightman, R. & Hofte, H., 2015. The Control of Growth Symmetry Breaking in the Arabidopsis Hypocotyl. *Curr Biol*, 25(13), pp.1746–1752. Available at: <http://www.ncbi.nlm.nih.gov/pubmed/26073136>.
- Peaucelle, A., Wightman, R. & Höfte, H., 2015. The Control of Growth Symmetry Breaking in the Arabidopsis Hypocotyl. *Current Biology*, 25(13), pp.1746–1752.
- Pfaffl, M.W., 2001. A new mathematical model for relative quantification in. , 29(9), pp.16–21.
- Price, R.A., Palmer, J.D. & Al-Shehbaz, I.A., 1995. Systematic relationships of Arabidopsis : a molecular and morphological perspective. *Arabidopsis*, pp.7–19. Available at: <http://ci.nii.ac.jp/naid/10003360476/en/> [Accessed March 31, 2018].
- Rajani, S. & Sundaresan, V., 2001. The Arabidopsis myc / bHLH gene ALCATRAZ enables cell separation in fruit dehiscence Sarojam Rajani * † and Venkatesan Sundaresan * ‡. , 1, pp.1914–1922.
- Reiter, W.-D., 1998. Arabidopsis thaliana as a model system to study synthesis, structure, and function of the plant cell wall. *Plant Physiology and Biochemistry*, 36(1), pp.167–176. Available at: <http://www.sciencedirect.com/science/article/pii/S0981942898801010>.
- Richards, O.W. & Kavanagh, A.J., 1943. The Analysis of the Relative Growth Gradients and Changing Form of Growing Organisms: Illustrated by the Tobacco Leaf. *The American Naturalist*, 77(772), pp.385–399. Available at: <http://www.jstor.org/stable/2457686>.
- Roeder, A.H.K., Ferrandiz, C. & Yanofsky, M.F., 2003. The role of the REPLUMLESS homeodomain protein in patterning the Arabidopsis fruit. *Current biology: CB*,

13(18), pp.1630–1635.

Roeder, A.H.K. & Yanofsky, M.F., 2006. *Fruit Development in Arabidopsis*,

Rozen, S. & Skaletsky, H., 2000. Primer3 on the WWW for general users and for biologist programmers. *Methods in molecular biology (Clifton, N.J.)*, 132, pp.365–386.

Sampathkumar, A. et al., 2014. Subcellular and supracellular mechanical stress prescribes cytoskeleton behavior in Arabidopsis cotyledon pavement cells D. Bergmann, ed. *eLife*, 3, p.e01967. Available at: <http://www.ncbi.nlm.nih.gov/pmc/articles/PMC3985187/>.

Sasidharan, R., Keuskamp, D.H., et al., 2014. Interactions between auxin, microtubules and XTHs mediate green shade- induced petiole elongation in Arabidopsis. *PLoS ONE*, 9(3), pp.1–13.

Sasidharan, R., Keuskamp, D.H., et al., 2014. Interactions between Auxin, Microtubules and XTHs Mediate Green Shade- Induced Petiole Elongation in Arabidopsis E. Huq, ed. *PLoS ONE*, 9(3), p.e90587. Available at: <http://www.ncbi.nlm.nih.gov/pmc/articles/PMC3942468/>.

Sassi, M. et al., 2014. An auxin-mediated shift toward growth isotropy promotes organ formation at the shoot meristem in Arabidopsis. *Current biology: CB*, 24(19), pp.2335–2342.

Sharma, N. et al., 2007. Katanin regulates dynamics of microtubules and biogenesis of motile cilia. *Journal of Cell Biology*, 178(6), pp.1065–1079.

Shaw, S.L., Kamyar, R. & Ehrhardt, D.W., 2003. Sustained microtubule treadmilling in Arabidopsis cortical arrays. *Science (New York, N.Y.)*, 300(5626), pp.1715–1718.

Skotheim, J.M. & Mahadevan, L., 2005. Physical Limits and Design Principles for Plant and Fungal Movements. *Science*, 308(5726), p.1308 LP-1310. Available at: <http://science.sciencemag.org/content/308/5726/1308.abstract>.

- Somerville, C. & Koornneef, M., 2002. A fortunate choice: the history of *Arabidopsis* as a model plant. *Nature reviews. Genetics*, 3(11), pp.883–889.
- Stoppin-Mellet, V., Gaillard, J. & Vantard, M., 2006. Katanin's severing activity favors bundling of cortical microtubules in plants. *Plant Journal*, 46(6), pp.1009–1017.
- Taylor, P.E., Card, G. & House, J., 2006. High-speed pollen release in the white mulberry tree, *Morus alba* L. In *Sex Plant Reprod.* Springer-Verlag.
- Ueda, K., Matsuyama, T. & Hashimoto, T., 1999. Visualization of microtubules in living cells of transgenic *Arabidopsis thaliana* Rapid communication. *Protoplasma*, 206(3), pp.201–206. Available at: <http://dx.doi.org/10.1007/BF01279267>.
- Uyttewaal, M. et al., 2012. Mechanical Stress Acts via Katanin to Amplify Differences in Growth Rate between Adjacent Cells in *Arabidopsis*. *Cell*, 149(2), pp.439–451. Available at: <http://linkinghub.elsevier.com/retrieve/pii/S0092867412002899>.
- Vaughn, K.C., Bowling, A.J. & Ruel, K.J., 2011. The mechanism for explosive seed dispersal in *Cardamine hirsuta* (Brassicaceae). *American Journal of Botany*, 98(8), pp.1276–1285.
- Vaughn, K.C. & Lehen, L.P., 1991. Mitotic Disrupter Herbicides. , 39(3), pp.450–457.
- Wang, M. et al., 2013. A Comparative Genome Analysis of PME and PME1 Families Reveals the Evolution of Pectin Metabolism in Plant Cell Walls. *PLoS ONE*, 8(8), pp.1–12.
- Wightman, R. et al., 2013. SPIRAL2 Determines Plant Microtubule Organization by Modulating Microtubule Severing. *Current Biology*, 23(19), pp.1902–1907. Available at: <http://www.sciencedirect.com/science/article/pii/S0960982213009226>.
- Wightman, R. & Turner, S.R., 2007. Severing at sites of microtubule crossover contributes to microtubule alignment in cortical arrays. *The Plant journal : for cell and molecular biology*, 52(4), pp.742–751.

- Yeats, T.H. & Rose, J.K.C., 2013. The formation and function of plant cuticles. *Plant physiology*, 163(1), pp.5–20.
- Zandomeni, K. & Schopfer, P., 2005. Reorientation of microtubules at the outer epidermal wall of maize coleoptiles by phytochrome, blue-light photoreceptor, and auxin. *Protoplasma*, 173, pp.103–112.
- Zhang, Q. et al., 2013. Microtubule Severing at Crossover Sites by Katanin Generates Ordered Cortical Microtubule Arrays in Arabidopsis. *Current Biology*, 23(21), pp.2191–2195. Available at:
<http://linkinghub.elsevier.com/retrieve/pii/S0960982213011342>.

Erklärung

Ich versichere, dass ich die von mir vorgelegte Dissertation selbstständig angefertigt, die benutzten Quellen und Hilfsmittel vollständig angegeben und die Stellen der Arbeit – einschließlich Tabellen, Karten und Abbildungen -, die anderen Werken im Wortlaut oder dem Sinn nach entnommen sind, in jedem Einzelfall als Entlehnung kenntlich gemacht habe; dass diese Dissertation noch keiner anderen Fakultät oder Universität zur Prüfung vorgelegen hat; dass sie – abgesehen von unten angegebenen Teilpublikationen – noch nicht veröffentlicht worden ist sowie, dass ich eine solche Veröffentlichung vor Abschluss des Promotionsverfahrens nicht vornehmen werde. Die Bestimmungen der Promotionsordnung sind mir bekannt. Die von mir vorgelegte Dissertation ist von Dr. rer. nat. Angela Hay betreut worden.

Köln, September 2018

Curriculum Vitae

PERSONAL DATA

Date of birth	30.07.1987
Place of birth	Cologne
Nationality	german

EDUCATION

10/15 – 12/2018	PhD Student at the Max Planck Institute for Plant Breeding Research Genetic basis for phenotypic evolution Topic: Growth Anisotropy and Cortical Microtubules in Explosive Pod Shatter
04/12 – 12/14	M.Sc. molecular and applied Biotechnology RWTH Aachen Final grade: 1.7 Master thesis at the Biochemical Engineering of the Process Engineering Aachen (AVT) with the topic: Effect of the density of viscous fluids on liquid movement in shake flasks
09/08 – 01/12	B.Sc. Biotechnology with practical semester FH Aachen Campus Jülich Final grade: 2.2 Bachelor thesis at the Fraunhofer-Institute for Molecular Biology and Applied Ecology (IME) in Aachen with the topic: Optimization of geraniol production on transgenic <i>in vitro</i> and <i>in vivo</i> cultivated tobacco plants
08/2004 – 06/2007	Erftgymnasium Bergheim Grade: Abitur (final grade: 2.1) Advanced courses: Biology and German
08/1998 - 08/2004	Gutenberg - Gymnasium Bergheim

OCCUPATIONS

05/13 – 04/15	Student assistant at the Enzyme Process Technology (EPT) at the Process Engineering Aachen (AVT) <ul style="list-style-type: none">- Preparation and measurement of enzyme kinetics- Chemical analysis (HPLC, GC)- Generation of piping and instrumentation diagrams- Organisation / Management of lab supplies
02/15 – 03/15	Intern at the Fraunhofer-Institute for Molecular Biology and Applied Ecology (IME), Aachen <ul style="list-style-type: none">- Cloning of CRISPR-Cas9 constructs (PCR)

06/13 – 10/13	Student assistant at the Helmholtz-Institute for biomedical Engineering, Aachen <ul style="list-style-type: none"> - Supervision of biology students during an internship („Glyco Biotechnology“) - Preparation and post processing of the experiments
10/12 – 03/13	Student assistant at the Biochemical Engineering (BioVT) at the Process Engineering Aachen (AVT) <ul style="list-style-type: none"> - Supervision of machine-engineering students during an internship („metrological Laboratory“) - Preparation and post processing of the experiments
10/09 – 09/10	Student assistant at the Environmental Biotechnology at the FH Aachen Campus Jülich, Jülich <ul style="list-style-type: none"> - Supervision of machine-engineering students during an internship („Environmental Biotechnology“) - Preparation and post processing of the experiments
07/05 – 09/08	Doctor's receptionist at the veterinary practise of C. Komorowski, Kerpen <ul style="list-style-type: none"> - Preparation of patients - Surgery assistance

FURTHER EDUCATION

01/18 - Today	Cornelia Harte Mentoring <ul style="list-style-type: none"> - CHM Mint - Support in career management
04/18	Seminar: Job Description Patent Attorney
03/18	Study visit to the EPO in The Hague <ul style="list-style-type: none"> - Insight into the work of EPO experts, patent examiners and lawyers
07/17 – 08/17	Summer School on Intellectual Property Modules: <ul style="list-style-type: none"> - Introduction to IP, Patents & Trade Secrets, IP Management, Copyright, Trademarks, Unfair Competition, IP & Contracts, Industrial Design
02/17 – 03/17	Seminar: Introduction into patent issues <ul style="list-style-type: none"> - History of patenting, today`s rules and regulations, exercises on Examples of FTO analysis, case studies

ADDITIONAL SKILLS

Computer literacy:	MS Office: competent knowledge MorphoGraphix: competent knowledge R statistics: basic knowledge
Language skills:	German: Mother tongue English: fluently French: basic knowledge